Remote Continuous Evaluation of a Bridge Constructed Using High-Performance Steel

BRIDGE ENGINEERING CENTER

Final Report
May 2006

Sponsored by
the Iowa Department of Transportation (CTRE Project 02-123)

ctre
Center for Transportation
Research and Education

IOWA STATE UNIVERSITY

About the Bridge Engineering Center

The mission of the Bridge Engineering Center is to conduct research on bridge technologies to help bridge designers/owners design, build, and maintain long-lasting bridges.

Disclaimer Notice

The contents of this report reflect the views of the authors, who are responsible for the facts and the accuracy of the information presented herein. The opinions, findings and conclusions expressed in this publication are those of the authors and not necessarily those of the sponsors.

The sponsors assume no liability for the contents or use of the information contained in this document. This report does not constitute a standard, specification, or regulation.

The sponsors do not endorse products or manufacturers. Trademarks or manufacturers' names appear in this report only because they are considered essential to the objective of the document.

Nondiscrimination Statement

Iowa State University does not discriminate on the basis of race, color, age, religion, national origin, sexual orientation, gender identity, sex, marital status, disability, or status as a U.S. veteran. Inquiries can be directed to the Director of Equal Opportunity and Diversity, (515) 294-7612.

Technical Report Documentation Page

1. Report No. CTRE Project 02-123	2. Government Accession No.	3. Recipient's Catalog No.	
4. Title and Subtitle Remote Continuous Evaluation of a Bridge Constructed Using High-Performance Steel		**5. Report Date** May 2006	
		6. Performing Organization Code	
7. Author(s) Terry Wipf, Brent M. Phares, Lowell F. Greiman, Derek Hemphill, Justin D. Doornink, Ping Lu		**8. Performing Organization Report No.**	
9. Performing Organization Name and Address Center for Transportation Research and Education Iowa State University 2711 South Loop Drive, Suite 4700 Ames, IA 50010-8664		**10. Work Unit No. (TRAIS)**	
		11. Contract or Grant No.	
12. Sponsoring Organization Name and Address Iowa Department of Transportation 800 Lincoln Way Ames, IA 50010		**13. Type of Report and Period Covered** Final Report	
		14. Sponsoring Agency Code	

15. Supplementary Notes

Visit www.ctre.iastate.edu for color PDF files of this and other research reports.

16. Abstract

Of the approximately 25,000 bridges in Iowa, 28% are classified as structurally deficient, functionally obsolete, or both. The state of Iowa thus follows the national trend of an aging infrastructure in dire need of repair or replacement with a relatively limited funding base. Therefore, there is a need to develop new materials with properties that may lead to longer life spans and reduced life-cycle costs. In addition, new methods for determining the condition of structures are needed to monitor the structures effectively and identify when the useful life of the structure has expired or other maintenance is needed. High-performance steel (HPS) has emerged as a material with enhanced weldability, weathering capabilities, and fracture toughness compared to conventional structural steels. In 2004, the Iowa Department of Transportation opened Iowa's first HPS girder bridge, the East 12th Street Bridge over I-235 in Des Moines, IA.

The objective of this project was to evaluate HPS as a viable option for use in Iowa bridges with a continuous structural health monitoring (SHM) system. The scope of the project included documenting the construction of the East 12th Street Bridge and concurrently developing a remote, continuous SHM system using fiber-optic sensing technology to evaluate the structural performance of the bridge. The SHM system included bridge evaluation parameters, similar to design parameters used by bridge engineers, for evaluating the structure.

Through the successful completion of this project, a baseline of bridge performance was established that can be used for continued long-term monitoring of the structure. In general, the structural performance of the HPS bridge exceeded the design parameters and is performing well. Although some problems were encountered with the SHM system, the system functions well and recommendations for improving the system have been made.

17. Key Words fatigue evaluation—fiber-optic strain sensor—high-performance steel—highway bridge—remote continuous structural health monitoring		18. Distribution Statement No restrictions.	
19. Security Classification (of this report) Unclassified.	**20. Security Classification (of this page)** Unclassified.	**21. No. of Pages** 141	**22. Price** NA

Form DOT F 1700.7 (8-72)   **Reproduction of completed page authorized**

REMOTE CONTINUOUS EVALUATION OF A BRIDGE CONSTRUCTED USING HIGH-PERFORMANCE STEEL

Final Report
May 2006

Principal Investigator
Terry J. Wipf
Professor of Civil Engineering, Iowa State University
Manager of the Bridge Engineering Center, Center for Transportation Research and Education

Co-Principal Investigator
Brent M. Phares
Associate Director of the Bridge Engineering Center, Center for Transportation Research and Education

Lowell.F.Greimann
Professor of Civil Engineering, Iowa State University

Research Assistant
Derek Hemphill
Justin D. Doornink
Ping Lu

A report from
Center for Transportation Research and Education
Iowa State University
2711 South Loop Drive, Suite 4700
Ames, IA 50010-8664
Phone: 515-294-8103
Fax: 515-294-0467
www.ctre.iastate.edu

TABLE OF CONTENTS

LIST OF FIGURES

LIST OF TABLES

ACKNOWLEDGMENTS

1. INTRODUCTION

Background

In early 2004, the Iowa Department of Transportation (Iowa DOT) completed construction on Iowa's first high-performance steel (HPS) bridge, the East 12th Street Bridge (hereafter referred to as the E. 12th St. Bridge or the bridge) over I-235 in Des Moines, Iowa, with funding from the Federal Highway Administration's (FHWA) Innovative Bridge Research and Construction (IBRC) program. When compared with conventional steels, HPS, which was developed in the mid-1990s, has improved weldability, weathering, and fracture toughness characteristics. As the replacement of bridges in Iowa and across the United States becomes more prevalent, the advantages of HPS make its use potentially very appealing. Specifically, the advantages of improved weathering and fracture toughness characteristics have long-term benefits that could reduce maintenance costs and extend the useful life.

The E. 12th St. Bridge (Figure 1.1), constructed using HPS girders, replaced a deteriorated concrete box girder bridge. The replacement is part of a renovation of the I-235 corridor through Des Moines and the surrounding metro area. The two-span bridge runs nearly north and south, providing one lane of traffic in each direction. The bridge connects the state capital area on the south to a residential area, including East High School, on the north.

Figure 1.1. East 12th Street Bridge over I-235 in Des Moines, Iowa

The IBRC program, which provides funding to design and construct innovative bridge solutions, required that the performance of the HPS bridge be evaluated and documented over a two-year period. With the ongoing success of bridge monitoring in Iowa, it was decided to further develop and deploy a continuous structural health monitoring (SHM) system for this evaluation. With this system, the bridge performance could be evaluated at any time and with respect to time. This

report documents the design and construction of the bridge, summarizes the monitoring system in place, describes the data management system, and documents the structural performance of the bridge.

Objectives

The following are the main objectives of the work described in this report:

- Monitor and document the construction of Iowa's first HPS bridge. Since the E. 12th St. Bridge represents the Iowa DOT's first use of HPS girders in bridge construction, it was important to document how the use of HPS altered typical bridge construction practices.
- Evaluate the use of HPS in bridge applications. With the aging infrastructure system in Iowa, it is necessary to identify viable options for rehabilitating the transportation system. The general structural performance of the bridge was studied to substantiate the further use of HPS in Iowa.
- Use innovative structural health monitoring techniques to continuously monitor the bridge performance. SHM offers a distinct advantage over conventional visual inspection in that bridge condition can be monitored continuously without being subjective. At any time, the overall condition of the bridge can be evaluated without the need to inspect the bridge physically, which eliminates the need for the traffic control typically required for field inspections.
- Develop initial concepts for monitoring bridge deterioration over time and develop a baseline record for identifying structural performance changes. Another aspect of SHM is the potential for quantifying the rate at which bridges deteriorate. Until recently, the technologies used to evaluate structures were inadequate to monitor structures accurately for an extended period. With the technologies developed and deployed in this project, it is possible to monitor structures over a long period without data drift, degradation, or error. With proper algorithms (similar to those developed as part of this project), reliable SHM systems can provide the information required to predict bridge deterioration over time. Such information can present opportunities for predicting the remaining life of a structure by understanding the current state of the bridge.
- Conduct a fatigue evaluation with specific interest in the impact of design features associated with HPS. Several typical and atypical fatigue-sensitive details were included in the bridge design. These details included the web gap detailing, stiffeners welded to the tension flanges, and weld concentrations at web and flange plate splices. These specific details were being evaluated because of Iowa's continued interest in their long-term performance.
- Continue developing expertise in the broad field of SHM in Iowa. The state of Iowa has long been a leader in innovative bridge research and construction. As a state with an extensive network of bridges and infrastructure but limited resources, it is important to continue to work toward finding ways to monitor the infrastructure to extend the life of the structures without compromising the safety of the general public, damaging the surrounding environment, and paralyzing the important transportation network that links the state together and to surrounding states.

Scope

The research summarized herein consists of several components. Initially the work consisted of observing and documenting the construction of the bridge. Concurrently, an innovative remote continuous SHM system (the first of its type in Iowa) was developed using available hardware to advance the practice of installing reliable long-term SHM systems on the bridge infrastructure. A data management system, including custom-developed software, was also developed to use the obtained data to evaluate both the long- and short-term performance of the bridge. Early in the project, it was decided that developing a system that could separate the long-term transient effects (such as temperature) from live load effects was important. Several techniques were investigated for accomplishing this. Ultimately, a behavior-based technique was developed that reliably separated these effects. Through the developed data management and interpretation system, the performance of the HPS girders was assessed, and a baseline record of the bridge's structural performance was established. An evaluation of the typical and atypical fatigue-sensitive details was also conducted to provide information about their general performance over time.

Report Organization

The literature review in the following section documents the differences between HPS and ordinary structural steel, reviews the existing SHM technologies and needs, and reviews stress cycle counting techniques. The section entitled "Bridge Description, Design, and Construction" describes the bridge and gives a general construction overview. The section entitled "Monitoring System" provides details about the monitoring and data management systems deployed on the HPS bridge. The section entitled "Performance" presents the performance of the bridge both over time and during a controlled load test. Conclusions and recommendations are then given in the final section.

2. LITERATURE REVIEW

In order to understand fully how the HPS girders used in the E. 12th St. Bridge are unique compared to girders used in other bridges in Iowa, the characteristics of HPS were reviewed. SHM technologies and systems were also reviewed to provide the research team with an understanding of the current state-of-the-art SHM systems, the systems' strengths and weaknesses, and ways to improve the practice of SHM through this project. To facilitate the quantification of stress cycles to which the bridge was exposed, cycle counting techniques were also reviewed. The review of these topics allowed the project team to document the construction of the subject bridge adequately, design and install a SHM system, and evaluate the performance of the subject bridge while advancing the state of SHM.

High-Performance Steel

Through a joint research program, the FHWA, the U.S. Navy, and the American Iron and Steel Institute (AISI) joined together in 1994 to develop HPS. This program was charged with improving weldability characteristics, increasing fracture toughness characteristics, and increasing corrosion resistance over ordinary steel. With these goals, the program developed HPS. Since its creation, numerous bridges using HPS girders have been constructed, with many shown to have been economically built.

In specifications, HPS is differentiated from traditional steel by placing the letters "HPS" before the specified minimum yield strength of the steel in kips per square inch (ksi). In most cases, the yield strength is also followed by the letter "W," which indicates that the steel must meet the ASTM G101 specification for weathering steel properties (Bethlehem 2002). HPS is commonly available in three design yield strengths: 50 ksi (HPS 50W), 70 ksi (HPS 70W), and 100 ksi (HPS 100W).

Chemistry

To achieve the desired properties of HPS, a unique alloy combination was developed. For comparison, a portion of the chemical composition of HPS 50W and 70W as well as those of conventional steels are shown in Table 2.1 (FHWA 2002). (Note that, for clarity, only the unique element levels are shown, and thus the total does not equal 100%.) The reduced carbon content in HPS improves the weldability of the steel, while the unique combination of chromium, copper, nickel, and molybdenum provides the enhanced corrosion resistance characteristics. The reduction in sulfur content over traditional steels improves the toughness of the steel, and the combination of other elements ensures that the strength requirements are met (Wilson 2000).

4

Table 2.1. Chemical composition of conventional and high-performance steels

		Carbon (%)	Manganese (%)	Phosphorus (%)	Sulfur (%)	Silicon (%)	Copper (%)	Nickel (%)	Chromium (%)	Molybdenum (%)	Vanadium (%)	Aluminum (%)	Nitrogen (%)
70W	Min.	0.0	0.80	0.0	0.0	0.25	0.20	0.0	0.40	0.0	0.02	0.0	0.0
	Max.	0.19	1.35	0.04	0.04	0.65	0.40	0.50	0.70	0.0	0.10	0.0	0.0
HPS 50W	Min.	0.0	1.10	0.0	0.0	0.30	0.25	0.25	0.45	0.02	0.04	0.01	0.0
&	Max.	0.11	1.35	0.02	0.01	0.50	0.40	0.40	0.70	0.08	0.08	0.04	0.02
HPS 70W													

Advantages of HPS

As previously stated, specific goals were set during the development of HPS to improve the attributes of available steels. This was done in an attempt to reduce overall life-cycle costs, improve safety, and ensure that steel remains competitive with other materials.

- Weathering: As with ordinary weathering steel, HPS does not have to be painted to prevent corrosion under normal atmospheric conditions. This attribute has the potential of reducing maintenance costs.
- Fracture Toughness: HPS is more ductile at low temperatures than ordinary steel and has a higher crack tolerance. The higher crack tolerance increases the safety of the bridge by allowing more time for detecting and repairing cracks.
- Weldability: To eliminate hydrogen-induced cracking in HPS weldments, lower preheat temperatures, less heat input control, and less post-weld treatment are required than for ordinary steel weldments. This feature eases the fabrication process, which can lead to lower initial fabrication costs.

Mechanical Properties of HPS

One of the goals in the development of HPS was to increase the fracture toughness of the steel at lower temperatures. The required toughness of HPS and the minimum yield and ultimate tensile strengths are given in Table 2.2 (FHWA 2002). For reference, the charpy-vee-notch is a measure of the toughness of the material. The higher the toughness (15 ft.-lbs. at 10°F for traditional steels [ASTM 2002]), the lower the risk of a brittle fracture, which again allows more time for detecting and repairing cracks.

Table 2.2. Mechanical properties of high-performance steel

	HPS 50W up to 4 in. as-rolled	HPS 70W up to 4 in. (Q&T), 2 in. (TMCP)
Minimum Yield Strength, F_y	50 ksi (345 Mpa)	70 ksi (485 Mpa)
Ultimate Tensile Strength, F_u	70 ksi (485 Mpa)	85–110 ksi (585–760 Mpa)
Minimum charpy-vee-notch, longitudinal orientation	25 ft.-lbs. (41 J) at 10°F (-12°C)	30 ft.-lbs. (48 J) at 10°F (-23°C)

Costs

The cost of HPS per pound is approximately twice the cost of A709 50W. However, the advantages listed above can lead to cost savings by offsetting the additional per-pound cost with effective use. In most designs, smaller sections are permitted when using HPS rather than ordinary steel. This results in a two-fold cost reduction. First, the dead load is reduced. This reduces the overall demand on the section (i.e., dead load plus live load plus impact, etc.), and a smaller section is required. Second, because of the improved properties, less total steel is required, resulting in a savings in the basic material costs. Even further, the lighter superstructure design reduces the sub-structure needs and general construction costs (e.g., lifting needs, transportation requirements, stability demands). Given that the steel does not have to be painted to prevent corrosion, long-term maintenance costs are also reduced. With higher fracture toughness, more time is available for crack detection and repair before a crack of critical length develops (FHWA 2002).

Structural Health Monitoring

SHM is an increasingly popular way to monitor the performance of structures. To ensure that the SHM system deployed on the E. 12th St. Bridge was based on the latest technology, the literature addressing SHM was reviewed. Areas of interest included sensors and data acquisition systems, with a focus on fiber-optic (FO) sensor-based systems, data transfer technologies, and data storage options.

Sensors

Several types of measurements techniques can be used to determine the behavior of a bridge structure. Strains, displacements, and accelerations are several common measurements that can be used to characterize performance.

Several different types of strain gages are available. The types most familiar to researchers include foil strain gages (Texas Measurements 2005) and vibrating wire strain gages (Roctest 2005). Wireless sensors and FO sensors can also be used to measure strain. Foil and vibrating wire strain gages are often categorized as conventional strain gages because they have existed and been used for many years. There are many advantages of foil strain gages, such as their low cost and ease of installation, but these gages' susceptibility to electromagnetic and radio interference, dependence on signal amplitude, and tendency to drift over time can limit their

usefulness in long-term monitoring applications. Vibrating wire strain gages, although more stable over the long term, can not sample fast enough to characterize live load effects adequately.

With conventional sensors, increasing the number of sensors significantly increases the complexity of the system, due to an increased number of wires. Increasing the number of wires in turn increases installation and material costs. To offset the increased costs and complexity of systems, wireless sensors have been developed. These sensors are usually powered with a battery of variable size and generally have a limited range over which data can be transmitted. Generally, wireless sensors are larger in size than wire-led sensors. Some types of wireless sensors are programmable to perform some limited data processing. Drawbacks to this type of sensor include limited power supply, limited communication distance, and higher price (Casciati et al. 2003).

As stated above, displacement transducers (Trans-Tek 2005) and accelerometers (PCB Piezotronics 2005) take readings that can also be used to interpret structural behavior. These sensors measure the global properties of the structure to determine bridge performance characteristics. Like foil strain gages, displacement transducers and accelerometers are vulnerable to electromagnetic and radio interference. However, this vulnerability does not preclude them from being used in long-term monitoring projects because they do not drift over time or depend on signal amplitude.

FO sensors, a relatively new type of structural sensor, have only recently become widely available. FO sensors have many advantages that can be put to use in the long term. Some available FO sensors can make many different types of measurements (e.g., strain, temperature, acceleration, displacement) and can be manufactured in unique forms to fit different needs. These needs include sensitivity (gage length or dynamic range) and location on a structure (crack detection, embedment, localized details, etc.). The ability of some types of FO sensors to be multiplexed together can be a significant advantage in terms of reducing the amount of cabling infrastructure. Since FO sensors and the process through which they are read are not affected by electric and electromagnetic fields, radio frequency, and signal amplitude, a FO-based system is an attractive option for long-term monitoring (Ansari 2003).

FO sensor systems operate by sending light waves (from a laser interrogator) down a fiber-optic cable. The information from the light wave, which is modified in some fashion by the sensor, is returned to the interrogator and provides the measurement basis. The different techniques used to read the different types of information from the light wave, as well as the way the light wave is modified, result from the different types of FO sensors available. According to Inaudi (2003), some of the different FO sensors include the following:

- SOFO is "based on the French acronym for Surveilance d'Ouvrages par Fibres Optiques – Structural Monitoring using Optical Fibers" (Glisic et al. 2003). In SOFO, displacement sensors "measure the length difference between two optical fibers" installed near each other. The sensors can measure displacements over distances between 200 mm and 10m.
- Microbending displacement sensors use a FO sensor with either fiber-optic cables or metallic wires wrapped along its length. The cables or wires wrapped around the sensor

change the properties of the sensor, causing light to be lost from the fiber. The deformation of the sensor can therefore be determined from the loss information. Known problems with microbending displacement sensors make them more suitable for short-term monitoring than long-term monitoring.

- Bragg Gratings, or Fiber Bragg Gratings (FBG), are capable of measuring both strain and temperature. As the fiber core of the FBG changes due to either mechanical strain or temperature change, the index of refraction of the sensor changes, therefore changing the wavelength of the signal returned. The major advantage of FBG is its ability to be multiplexed together on a single length of fiber-optic cable.

- Fabry-Perot sensors are capable of measuring strain. These sensors work by measuring the interference caused by an air gap between two cleaved fibers whose ends are a small distance apart within a capillary silica tube (Inaudi 2003).

Another type of FO technique that can be used to measure strain is a Brillouin scattering-based sensor system. This method is based on the Brillouin scattering principle, which says that Brillouin scattering occurs when the density of the optical fiber is changed. Through the use of Brillouin optical time domain reflectometry (B-OTDR), the location of the density change of the fiber can be found. This application has been used for monitoring over long distances (such as gas pipe lines) (Liu 2003).

Long-guage FO sensors can be used to find the strain over long distances (gage lengths between 250 mm and 10m). This type of sensor can be useful when looking at the global properties of a structure. As a long-gage sensor, the SOFO sensor was designed specifically for embedment in concrete. This sensor allows strain measurements to be used for the dynamic evaluation of a structure as well as long-term monitoring (Inaudi and Glisic 2004).

Fiber-Optic Interrogators

As stated above, FO sensing of all types is based on light waves and the interpretation of information from the light waves after a sensor has changed the properties of the light band. Different interrogators use different means to extract the information from the reflected light waves. According to Todd, Johnson, and Althouse (2001), different techniques for measuring wavelength shifts from FO sensors are based largely on principles involving the following: scanning Fabry-Perot (SFP) filter-based interrogation, tunable acousto-optic filter interrogation, wavelength division multiplexed interferometric interrogation (WDM), and prism/CCD- (charged coupled device) array techniques. A broadband light source and broadband detectors are used by SFP and acousto-optic (tunable filter techniques) systems. The filters are tuned so only one sensor per array for multiplexed sensors is read at a time. SFP filter-based interrogation finds the gratings' reflection peaks by controlling the voltage applied to the filter, while acousto-optic systems change the frequency applied to the filter. WDM and CCD array-based systems use a broadband source and broadband detectors along with components that can separate wavelengths to read multiple sensors at the same time. The WDM system requires the wavelengths from the sensors be in the middle of the filters' passbands; therefore, large shifts in wavelengths are not permitted. This system would best be used in applications for which low-amplitude readings are expected. CCD array systems do not require the wavelengths to be within a certain bandwidth and, therefore, can read larger amplitude shifts in wavelengths (Todd, Johnson, and Althouse 2001).

Micron Optics manufactures FO sensor interrogators that can read up to 512 FBG sensors on four channels at speeds up to 250 Hz. The interrogator consists of a computer with a built-in color LCD display. The system can be linked to other equipment using an Ethernet cable (Micron Optics 2005).

Roctest manufactures two different types of interrogators for use with their proprietary FO sensors (Fabry-Perot strain gages as well as transducers that have a wide range of measuring capabilities, including strain, pressure, temperature, displacement, and force). The first system has eight channels that can be monitored at 100, 500, or 1000 Hz. An RS-232 communication port controls each channel separately. A 10-volt analog output is generated for each individual channel. The second system is a data logger that can store 50,000 data samples before needing to be downloaded. Units consisting of between 16 and 32 channels are available (Roctest 2005).

Luna Innovations manufactures interrogators that can scan multiple types of Luna FO sensors, including FBG and Fabry-Perot strain sensors and FO sensor accelerometers. The 8 sensor channels, which can be expanded to 64 channels with expansion units also offered by Luna Innovations, produce data through a RS-232 connection. A backlit LCD readout allows control of the unit, which can collect data at up to 100 Hz. Another FO sensor interrogator offered by Luna Innovations can scan up to 8 channels at 130 Hz. This unit has a USB data port available for connecting a display Luna Innovations (2005).

Blue Road Research manufactures several different units; the model with the largest capacity will be detailed here. The unit has two modes: (1) high bandwidth mode, which allows for one sensor to be read per channel at speeds up to 10 kHz at a 0.2 me noise level or 2 MHz at a 2.0 me noise level; and (2) multi-sensor mode, in which up to 20 sensors are able to be read per channel at speeds of 50 Hz. These units are capable of reading Blue Road Reasearch's catalog of sensors, including single- and dual-axis FBG strain sensors (Blue Road Research 2005).

Data Transfer

As with any project that involves data collection, the E. 12th St. Bridge SHM system will be required to transfer data from one location to another. In general, information must typically be transferred between equipment components that are located close to one another and to equipment that is located far away. For equipment components close to one another, it is most common to establish a local area network (LAN). For greater distances, the Internet is a medium through which two LANs can be connected. Communication can take place using both wired and wireless technology.

Wired Technologies

To transfer data within a LAN, the computers need to be linked together. In terms of wired connections, this is usually accomplished with Ethernet cables because they are low-cost and widely available. Ethernet connections can commonly transfer data at speeds from 10 megabits per second (Mbps) to 100 Mbps (Microsoft 2005). A new class of Ethernet connections can transfer data at up to 1,000 Mbps. Fiber optic cables can also be used for data transfer through

fiber distributed data interface (FDDI), which can transfer at speeds between 100 Mbps and 2 Gbps (Indiana University 2005).

There are many different modes to connect computers to the internet. A public switched telephone network (PSTN) connection to the internet uses standard telephone lines. The transfer speed using PSTN depends on many factors and is usually less than 56 Kbps at a cost of about $20 per month. An integrated services digital network (ISDN) can use a single wire to carry both voice and data over the internet; speeds are usually limited to around 64 Kbps at a cost of around $30 a month, with an initial equipment fee of less than $200. A digital subscriber line (DSL) also uses regular telephone lines to transfer data to the Internet. DSL connections can typically upload data at around 640 Kbps and download data at up to 1.5 Mbps. The cost of DSL modems is usually less than $100, and service can range between $30 and $150 per month. T-Carrier technology, which is commonly used to connect large organizations to the internet, is available in two different types, T-1 and T-3. T-1 connections transfer data at speeds up to 1.544 Mbps and T-3 at speeds up to 44.736 Mbps. These types of connections are typically available only at high costs. Asynchronous transfer mode (ATM), which can integrate the transfer of audio, data, image, text, and video information (Center for the New Engineer 2005), can have transfer rates between 25 Mbps and 600 Mbps, but is best suited for audio and video communication (Froelich 2005).

Wireless Technologies

Currently, the IEEE 802.11 standard regulates the operation of wireless LAN (WLAN). Communication within a WLAN can be performed via radio frequency (direct sequence or hopping spread spectrum) or infrared frequency. The mode of communication also governs the transmission speed, which can vary from 1 Mbps to 54 Mbps for radio frequency systems and up to 622 Mbps for infrared systems. WLAN can operate between point-to-point or point-to-multipoint systems.

Wireless communication within a LAN typically occurs between two types of equipment. First, wireless devices must have a wireless network adapter. These network adapters function in much the same way as a wired network adaptor. Wireless communication to the rest of the LAN occurs through a piece of equipment known as an access point. Access points can either be standalone units or integrated into a piece of hardware with other capabilities (e.g., routing, switching). Currently, there are three types of 802.11 standards, known as 802.11a, 802.11b, and 802.11g. In some cases, wireless WAN can be configured with devices using any of the three standards.

An emerging technology for short-distance communication within a LAN is known as Bluetooth. Currently, Bluetooth is most often used between computers and their components (mouse, keyboard, etc.), mobile phones, and other portable devices. Unfortunately, the same frequency band used by the 802.11 standard is used for Bluetooth, so interference is possible. However, newer standards should relive some of the congestion in that frequency range. Bluetooth has a range of up to approximately 10 meters.

Broadband wireless (BW) communication is often compared to DSL, as BW connects local users to the internet. The transmitter and receiver must have an unobstructed path between them to

transfer information. The distance over which BW can operate depends on the frequency used for transmission. Local multi-point distribution service (LMDS), which uses transmitters spaced about one mile apart, operates at a higher frequency and has a large bandwidth, capable of supporting all the channels of direct broadcast satellite TV. The lower bandwidth service, multi-channel multi-point distribution service (MMDS), has transmitters up to 35 miles apart, but has lower transfer rates than LMDS.

Issues that must be considered when using any wireless communication protocol include interference and security. Interference in the communication can be caused by obstacles in the direct path of communication and by electromagnetic interference. Interference issues can generally be overcome by intelligent placement of the wireless components. Security issues can be tightened by using authentication and encryption. Authentication can be performed through allowing only certain MAC addresses to enter the network and by using a closed network with a non-advertised name. High levels of data encryption (e.g., 128 or 256 bit) can be also used to create virtual "wires" between two wireless nodes (University of Tennessee 2005).

Data Storage

Once the data are obtained from the data acquisition system, they will need to be stored before and after any processing of the data. The storage of the data can be broken into two categories: flat files (i.e., .txt and .dat files) and databases (Dummies.com 2005). A flat file is a single table, in which the user must know the location (row and column location) of an item to find it (Webopedia "Flat-file" 2005). A database consists of a collection of multiple tables linked together. An item is found within a database by queries. A database can be thought of as an "electronic filing system" (Webopedia 2005). Flat files are easy to create, do not require special software, are easy to open, and use less space than databases. Databases are more secure than flat files, facilitate data location when the data structure is complex, and allow multiple users to access the database at the same time (Dummies.com 2005).

Structural Health Monitoring Systems

On the Commodore Barry Bridge, Kulcu et. al. (2000) used different gages and acquisition rates to capture different types of data. Long-term data are collected once every 15 minutes, 7 days a week, using vibrating wire strain gages and a Campbell Scientific data acquisition system. Short-term data (live load) were collected at approximately 100 Hz with foil-resistance strain gages, accelerometers, and an Optim MEGADAC data acquisition system, twice a day, every day for one week during two quarters of the year. Wind data were also collected every 5 seconds from the bridge using ultrasonic wind sensors and a Handar data acquisition system. Control of the system was provided through remote applications; this connection was made through an ordinary telephone line.

The data acquisition control and data presentation of the wind data, live video data, and long-term data from the Commodore Barry Bridge were performed using a Lab-View platform. The wind data were processed and saved in daily files that were stored in a database. After processing, the long-term data were stored in spreadsheets. The short-term data were also processed before being archived. Future work on this monitoring project includes redesigning

11

the data acquisition system to make it a fully automatic web-based system and to fully automate the data processing system (Kulcu et al. 2000).

A strengthening project on the Horsetrail Falls Bridge, in which fiber reinforced plastic (FRP) wrap was used to strengthen two reinforced concrete beams externally, was evaluated over a two-year period with 28 FBG sensors. Although FBG sensors usually have a gage length around 1 cm, capillary tubes were used to mount the sensors, which effectively changed the gage lengths to 70 cm or 100 cm, depending on the desired gage length. FBG sensors were chosen for their qualities that are beneficial in long-term monitoring, their ability to be used with long gage lengths, and their small size, which was appealing because this bridge is a historic landmark in the Columbia River Gorge (Seim, Udd, and Schulz 1999).

ISIS Canada has used FO sensors to investigate the use of FRP to strengthen deteriorated concrete structures from remote locations. At the time of publication of the reference article (Tennyson et al. 2001), 16 bridges in Canada had been monitored using FO sensors. The FBG used for the project generally experienced a low failure rate when properly installed. The accuracy of the FO sensors was verified (with success) by conventional strain gages. The resilience of FO sensors and electric strain gages embedded in concrete were also compared. The FO sensors were more robust than electric strain gages when embedded in concrete. Examples of the use of FO sensors by ISIS Canada are presented in the following paragraph.

On the Beddington Trail Bridge in Alberta, Canada, 20 FBG sensors were embedded into the concrete girders, which were prestressed with carbon fiber composite cables. Readings were taken from the sensor six years after they were installed, and 18 were still working. The Taylor Bridge in Manitoba is one of the largest highway bridges reinforced by FRP and monitored using FO sensors. Carbon fiber reinforced polymer was used as reinforcement in the prestressed girders and in a portion of the deck slab. The barrier walls were reinforced with glass fiber reinforced polymer. The FRP reinforcing bars were monitored with 63 FBGs and two multi-Bragg sensors. Temperature compensation was provided through readings taken with 22 electric-based sensors. Twenty-six electrical strain gages were placed near selected FBGs to verify the readings, of which more than 60% failed, although they were properly sealed during the steam curing of the girders (Tennyson et al. 2001).

Stress Cycle Counting

Bridges are loaded by vehicles of varying configurations and weights, causing varying levels of stress at different locations. These stress levels can differ even more as the global boundary conditions change with environmental changes (temperature, humidity, direct sunlight, etc.) and with bridge deterioration. To characterize the magnitudes of stresses induced on details, stress cycle counting techniques are commonly used. Stress cycle counting produces a snapshot of the size and associated number of stress cycles that a bridge has been exposed to. Such data are useful in fatigue evaluations.

The first cycle counting methods to be developed were termed level-crossing counting, peak counting, and simple range counting. Although not described in detail here, these methods are

generally considered inadequate because they do not take into account the sequence in which the stress cycles occur. The order in which the cycles occur is of most importance for materials with non-linear stress-strain relationships.

The rainflow counting technique (sometimes known as "Falling Rain" on "Pagoda Roof"), developed by Matsuishi and Endo, is a procedure that counts closed hysteresis loops of varying stress magnitudes. Because of its widespread acceptance, "rainflow counting" is a common phrase used to denote all methods that use closed hysteresis loops to identify stress cycles. Common rainflow counting algorithms include the original rainflow counting, range-pair counting, range-pair-range counting, Haynes method, ordered overall range counting, racetrack counting, and hysteresis loop counting. All of these methods will provide matching results if the strain-time plot begins and ends with the largest strain magnitude. In other cases, the methods will not give equal results, but the results will be similar (Bannantine, Commer, and Handrock 1990).

The following is an excerpt from Bannantine, Commer, and Handrock (1990), in which a step-by-step description of the "Falling Rain" method is given:

> The first step in implementing this procedure is to draw the strain-time history so that the time axis is oriented vertically, with increasing time downward. One could now imagine that the strain history forms a number of "pagoda roofs." Cycles are then defined by the manner in which rain is allowed to "drip" or "fall" down the roofs. [This is the analogy used by Matsuishi and Endo, mentioned above, from which the rainflow method of cycle counting received its name.] A number of rules are imposed on the dripping rain so as to identify closed hysteresis loops. The rules specifying the manner in which rain falls are as follows:
>
> 1. To eliminate the counting of half-cycles, the strain-time history is drawn so as to begin and end at the strain value of greatest magnitude.
> 2. A flow of rain is begun at each strain reversal in the history and is allowed to continue to flow, unless
>   a. The rain began at a local maximum point (peak) and falls opposite a local maximum point greater than that from which it came.
>   b. The rain began at a local minimum point (valley) and falls opposite a local minimum point greater (in magnitude) than that from which it came.
>   c. It encounters a previous rainflow.
>
> The foregoing procedure can be clarified through the use of an example. [Figure 2.1] shows a strain history and the resulting flow of rain. The following discussion describes in detail the manner in which each rainflow path was determined.
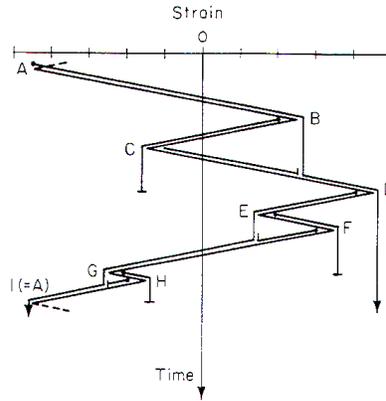
Figure 2.1. Rainflow counting, or "Falling Rain" approach (Bannantine, Commer, and Handrock 1990)

As shown in [Figure 2.1], the greatest strain-time history begins and ends at the strain value of greatest magnitude (point A). Rainflow is now initiated at each reversal in the strain history.

A. Rain flows from point A over points B and D and continues to the end of the history, since none of the conditions for stopping rain flow are satisfied.

B. Rain flows from point B over point C and stops opposite point D, since both B and D are local maximums and the magnitude of D is greater than B (rule 2a above).

C. Rain flows from point C and must stop upon meeting the rain flow from point A (rule 2c).

D. Rain flows from point D over points E and G and continues to the end of the history, since none of the conditions for stopping rain flow are satisfied.

E. Rain flows from point E over point F and stops opposite point G, since both E and G are local minimums and the magnitude of G is greater than E (rule 2b).

F. Rain flows from point F and must stop upon meeting the flow from point D (rule 2c).

G. Rain flows from point G over point H and stops opposite point A, since both G and A are local minimums and the magnitude of A is greater than G (rule 2b).

H. Rain flows from point H and must stop upon meeting the rainflow from point D (rule 2c).

Having completed the above, we are now able to combine events to form completed cycles. In this example, events A–D and D–A are combined to form a full cycle. Event B-C combines with event C-B (of strain range C–D) to form an additional cycle. Similarly, cycles are formed at E-F and G-H. (Bannantine, Commer, and Handrock 1990)

3. BRIDGE DESCRIPTION, DESIGN, AND CONSTRUCTION

Bridge Description

The E. 12th St. Bridge over I-235 in Des Moines, Iowa, shown in Figure 1.1, is a 298 ft. 7 in. long two-span HPS girder bridge, with an 8 in. thick cast-in-place concrete deck. The deck (constructed composite with the HPS girders) and sidewalks were constructed using high-performance structural concrete (HPSC) with a minimum strength of 5,000 psi. The framing plan of the bridge is shown in Figure 3.1. The north span is 153 ft. 3 in. long and the south span is 145 ft. 4 in. long. The girders are supported at the ends with integral abutments (the north integral abutment is shown in Figure 3.2). The driving portion of the bridge consists of two lanes with a total width of 29 ft. 6 in. The pedestrian walkways, flanking both sides of the roadway, are each 7 ft. 10 in. wide. The six girders, spaced at 8 ft. 8 in., as shown in Figure 3.3, are constructed with HPS, with each girder having three longitudinal segments. The 113 ft. 6 in. long "North Region" and the 103 ft. 1 in. long "South Region" were constructed with HPS 50W steel, while the 82 ft. 0 in. long "Center Region" was constructed with HPS 70W steel. The girders in the "North Region," "Center Region," and "South Region" each have different cross sections; the details of each are shown in Figures 3.4 though 3.6.
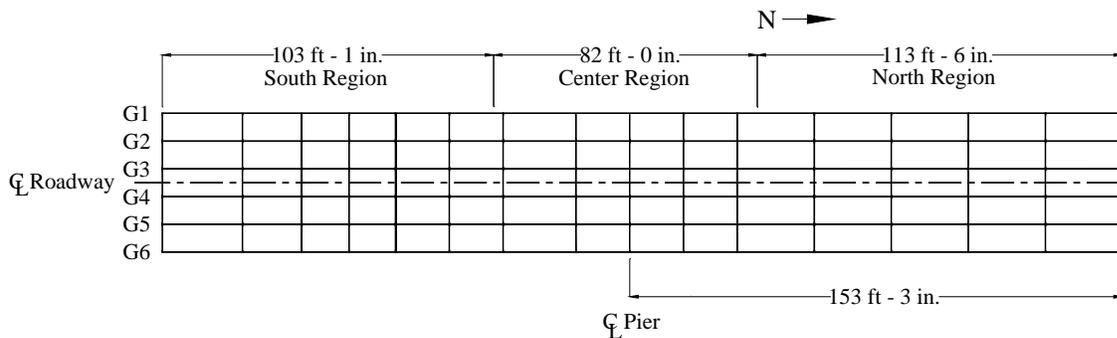
Figure 3.1. Plan view of the E. 12th St. Bridge framing system

Figure 3.2. Typical girders and the north integral abutment
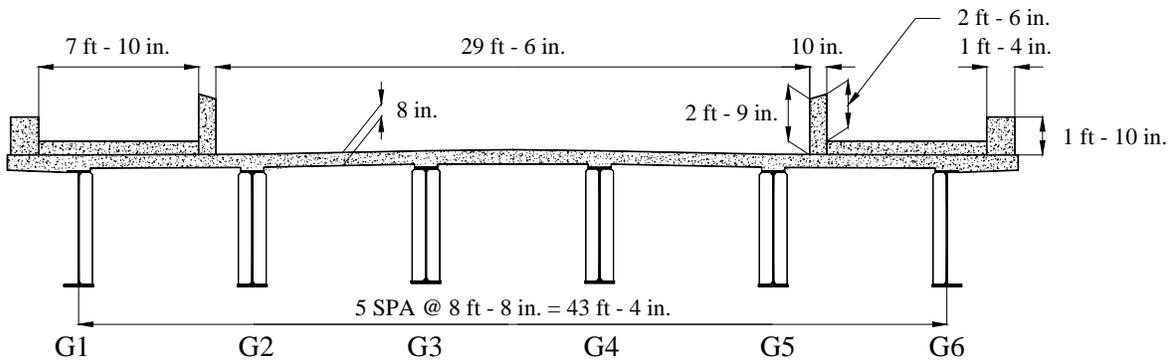
Figure 3.3. Typical cross-sectional view of the E. 12th St. Bridge (looking north)
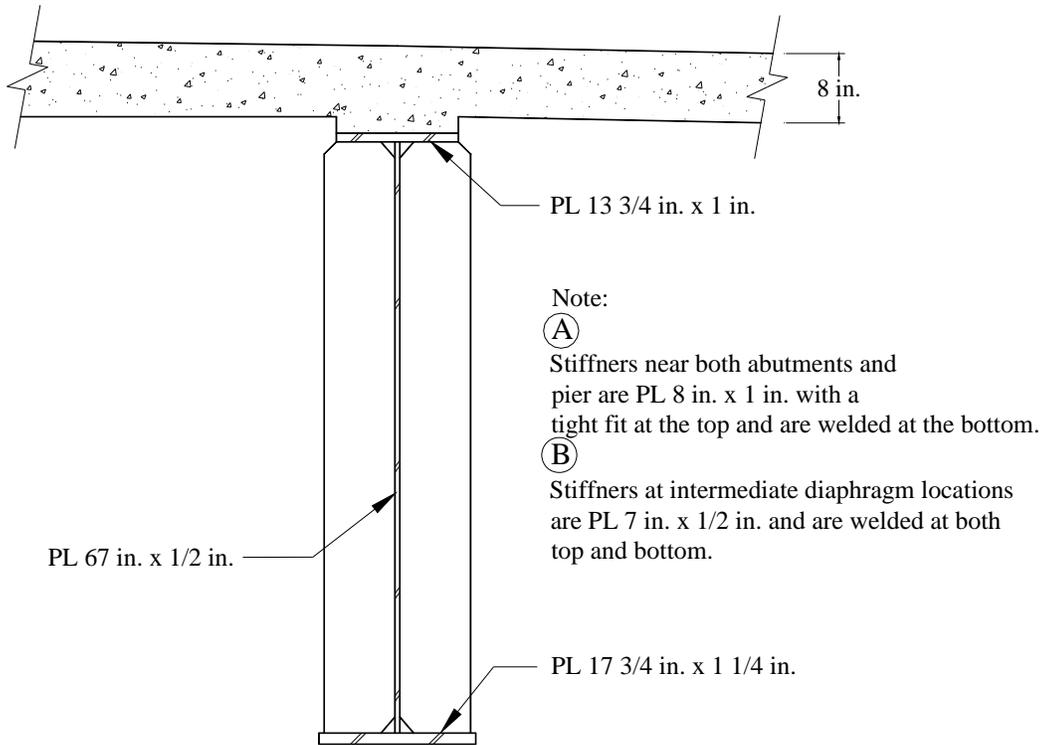
Figure 3.4. Cross section of the "North Region" girders

8 in.

PL 13 3/4 in. x 1 in.

Note:
Ⓐ
Stiffners near both abutments and
pier are PL 8 in. x 1 in. with a
tight fit at the top and are welded at the bottom.
Ⓑ
Stiffners at intermediate diaphragm locations
are PL 7 in. x 1/2 in. and are welded at both
top and bottom.

PL 67 in. x 1/2 in.

PL 17 3/4 in. x 1 1/4 in.
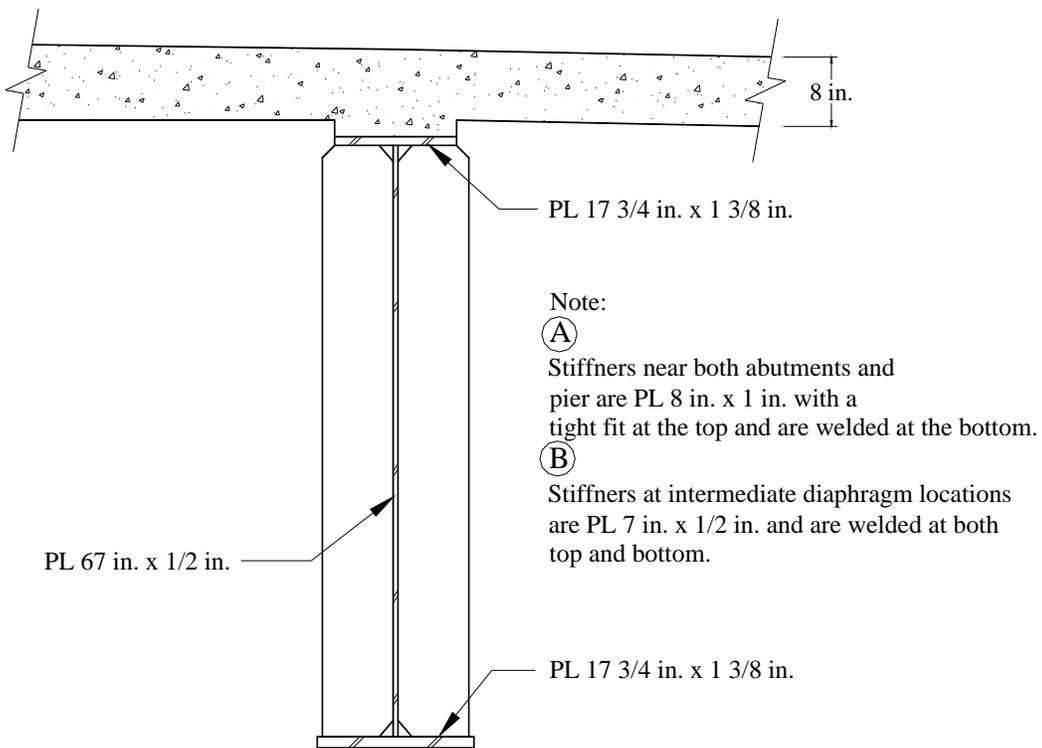
Figure 3.5. Cross section of "Center Region" girders

8 in.

PL 17 3/4 in. x 1 3/8 in.

Note:
Ⓐ
Stiffners near both abutments and
pier are PL 8 in. x 1 in. with a
tight fit at the top and are welded at the bottom.
Ⓑ
Stiffners at intermediate diaphragm locations
are PL 7 in. x 1/2 in. and are welded at both
top and bottom.

PL 67 in. x 1/2 in.

PL 17 3/4 in. x 1 3/8 in.

8 in.

PL 11 13/16 in. x 13/16 in.

Note:
(A)
Stiffners near both abutments and
pier are PL 8 in. x 1 in. with a
tight fit at the top and are welded at the bottom.
(B)
Stiffners at intermediate diaphragm locations
are PL 7 in. x 1/2 in. and are welded at both
top and bottom.

PL 67 in. x 1/2 in.

PL 17 3/4 in. x 1 in.

Figure 3.6. Cross section of "South Region" girders

Bridge Design

The Iowa DOT identified the East 12th St. Bridge as an opportunity for the Iowa DOT's initial use of HPS. The IBRC program requirements of monitoring and evaluating the demonstration bridge for a two-year period provided an opportunity for the Office of Bridges and Structures not only to do a thorough evaluation of the bridge performance, but also to become very familiar with the design, fabrication, and construction issues associated with this relatively new structural material for future applications. The bridge was designed to take full advantage of the HPS structural properties, including material strength, toughness, and fatigue.

Bridge Construction

A challenge in constructing the subject bridge was working over the major roadway (I-235) that the bridge spans. With the volume of traffic I-235 carries, the Iowa DOT mandated that I-235 not be shut down during normal workday hours. During non-peak hours (in middle of the day during the work week), one lane at a time could be shut down for short periods of time. The allowance for this lane closure allowed some construction operations to proceed without the need for nighttime work. However, when construction required full closure of I-235, work had to be completed at night and typically occurred on weekends. The contractor for the subject bridge was United Contractors, Inc., of Johnston, Iowa.

Demolition

Before construction of the new bridge could begin, the existing concrete box-girder bridge, shown in Figure 3.7, had to be removed. Demolition began with the removal of the guardrails, light poles, and other items that could be removed without closure of I-235. On the night of Saturday, May 3, 2003, I-235 was closed from E. 6th St. to East 15th St. to allow the majority of the demolition to take place. Most of the demolition was completed in a conventional manner, using track hoes with vibrating hammers that punched holes in the bridge deck. These holes enabled track hoes with buckets to tear apart the bridge, with supplemental aide from the vibrating hammer-equipped track hoes (see Figure 3.8). On the night of May 3, I-235 was closed to traffic at approximately 12 a.m. Saturday night and reopened to traffic 30 hours later, prior to Monday morning rush hour traffic.

Figure 3.7. Original E. 12th St. Bridge

Figure 3.8. Demolition operations on Sunday, May 4, 2003

Construction

Abutment Footings

After the box-girder bridge had been removed, work began by constructing new bridge abutments. Because the replacement bridge has integral abutments, work started by driving H-piles. The north abutment consists of a row of 15 HP 10x42 piles, with a single HP 10x42 pile behind each outer pile in the row, for a total of 17 piles. The south abutment was constructed with a row of 14 HP 10x42 piles, with a single HP10x42 pile behind the outer pile on the west side of the abutment and 2 HP10x42 piles behind the outer pile on the east side of the abutment, for a total of 17 piles. The piles were driven to a depth at which they reached the design bearing value (73 Kips). Exposed piles following installation can be seen in Figure 3.9. After the piles were driven, the top of the piles were encased in concrete to form the complete abutment. Figure 3.10 shows an abutment under construction.

Figure 3.9. Piles at south abutment before abutment concrete was placed

a. Front view of abutment

b. Top view of abutment

Figure 3.10. South integral abutment footing before formwork was removed

Pier

As work was progressing with the abutments, construction of the center pier was also initiated. The original bridge pier foundation was removed, and a new foundation was constructed at approximately the same location. Vertical steel reinforcing bars were extended past the top of the foundation to tie the foundation and pier stem together. The reinforcing bars for the pier columns were then tied to the exposed bars, as seen in Figure 3.11.

Due to the unique geometry of the V-pier, shown in Figure 3.12, flat plate girder forms were used to form the north and south sides of the pier (the sides facing the abutments). Adjustable

metal forms, with the ability to form radii, were used to form the curved sides of the columns. Three sides of the formwork were assembled on the ground. Specifically, one flat plate girder form was laid horizontally, and the radii of the formwork were set vertically upon it, as seen in Figure 3.13. This partially complete formwork was then lifted into place with the last flat plate girder form and set into position, thus completing the formwork for the pier stem and columns. The fully assembled pier formwork can be seen in Figure 3.14.

As with the demolition of the existing bridge, the placement of the concrete for the pier stem and columns could not take place during the day. Placement of the concrete required that multiple lanes of I-235 traffic be shut down because a crane was used to lift the concrete into place and a large number of concrete trucks were needed. Together, these necessitated nighttime placement of the concrete. The completed pier stem and columns are shown in Figure 3.15.

Figure 3.11. Reinforcing steel for the center pier
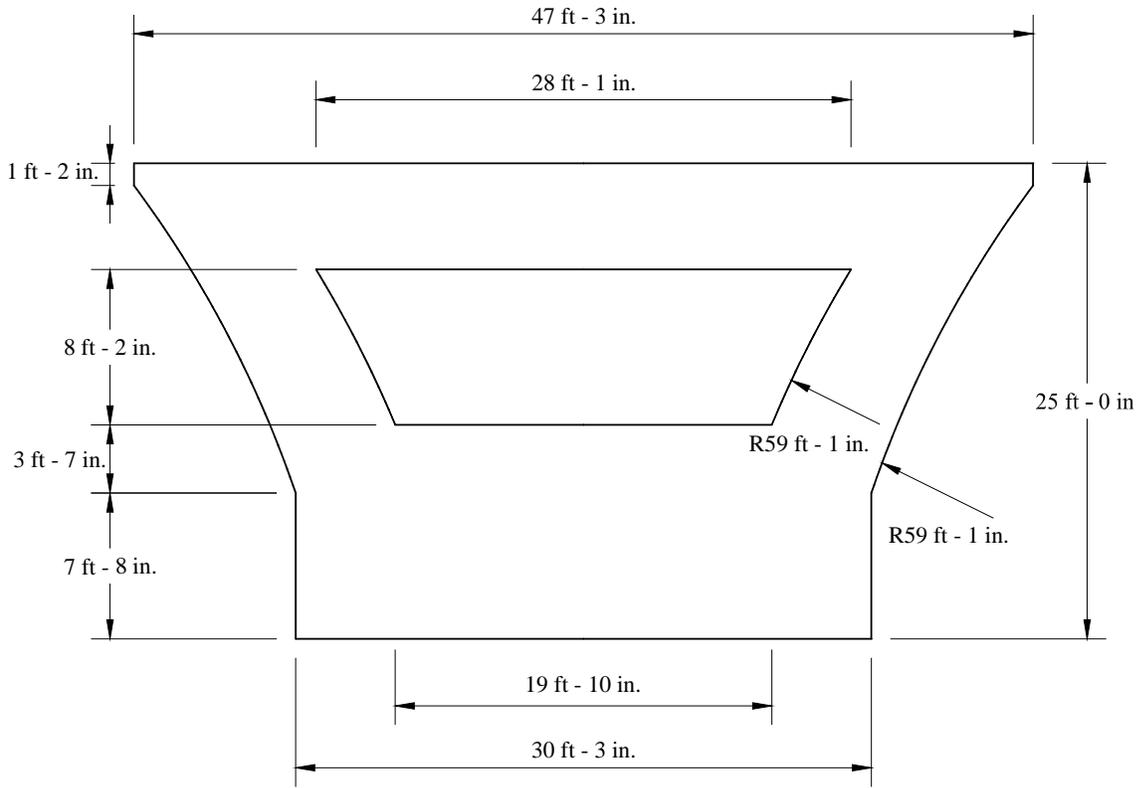
Figure 3.12. Elevation view of the center pier

Figure 3.13. Formwork for the center pier during assembly

Figure 3.14. Center pier formwork after assembly and placement

Figure 3.15. Center pier after formwork was stripped and before reinforcing steel and formwork for the pier cap were constructed

Once the pier stem and columns had gained sufficient strength, assembly of the formwork for the pier cap began. The formwork was assembled in place; this can be seen in Figure 3.16. Similar to the placement of the pier stem and columns, the placement of the concrete for the pier cap also took place during a nighttime shutdown of I-235. The completed pier can be seen in Figure 3.17.

Figure 3.16. Formwork for the center pier cap being constructed

Figure 3.17. Completed center pier

HPS girders

The HPS girders used in the bridge were manufactured in Illinois by Industrial Steel Construction, Inc. The girders were shipped to the site, by truck, with three to four sections of girder delivered at a time (only one section per truck). Delivery took place during non-peak daytime hours when one lane of I-235 could be closed to traffic; this lane was needed for unloading. Figure 3.18 depicts a delivery, and Figure 3.19 shows several stockpiled girders. To facilitate construction the "North Region" and "Center Region," sections of girders were stored

in the median, where they were spliced together before installation. girders for the "South Region" section were stored on the south side of I-235.

Erection of the HPS girders was also completed during a nighttime operation. The cranes used to set sections of the girders were temporarily moved directly onto the I-235 roadway, and the girders were hoisted over the roadway. Setting all the sections and cross-frames of the six girders occurred during three night-time operations. During the first night, the "North Region" and "Center Region" of all six girders were set, as shown in Figure 3.20. The cross-frames between the set sections of the girders were also installed during the first night.

The "South Region" of four of the six girders (G3, G4, G5, and G6) and the corresponding cross-frames were placed during the second night. This is shown in Figure 3.21. During the third night, the remaining regions of the two girders were installed along with the cross-frames between these sections. The completed framework of girders and cross-frames is shown in Figure 3.22. A false deck sitting on the bottom flange of the girders was also constructed during the nighttime operations; the false deck can be seen in Figure 3.23. This false deck both served as a work platform in regions directly over I-235 and prevented construction assemblies or debris from falling on I-235 below.
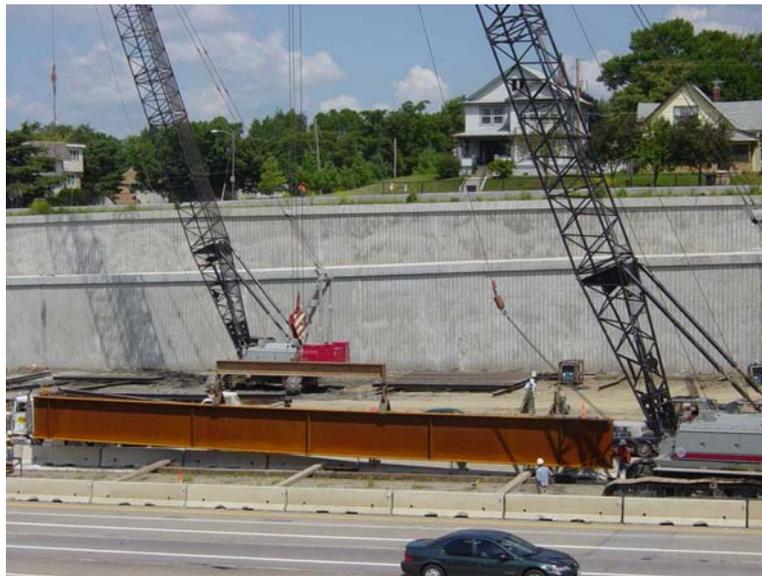
Figure 3.18. HPS girder being unloaded following delivery

26

Figure 3.19. Stockpiled HPS girders located on the south side of I-235

Figure 3.20. HPS girder being set during the first of three nighttime operations

Figure 3.21. Girders installed after the second night of girder setting operations

a. Side view of bridge

b. End view of bridge

Figure 3.22. Bridge after all girders have been erected

Figure 3.23. Work platform resting on the bottom flange of the girders over I-235

Reinforced Concrete Deck

After the formwork and reinforcing bars had been installed for the deck and the integral abutment cap, the first of two sequenced concrete placements took place. Figure 3.24 shows the deck formwork stringers along with several intermediate cross-frames. The northern positive moment region and abutment and the southern positive moment region and abutment constituted the first placement. After the second placement, which consisted of the center negative moment region, had cured to sufficient strength, the pedestrian walkways and the barrier rails were placed. Figure 3.25 shows the concrete covered for insulation during curing. The barrier rails (two on each side, one to guard the edge of the bridge and one to separate pedestrians from traffic) were constructed using a continuous slip forming technique. The completed slip formed barriers can be seen in Figure 3.26.

Opening

The bridge was opened to traffic on March 23, 2004, 10 months and 20 days after the original bridge was closed for replacement. The total cost of the demotion of the original bridge and construction of the new bridge was $13,037,674.60. The completed bridge is shown in Figure 3.27.

Figure 3.24. Intermediate cross-frames and deck formwork stringers

Figure 3.25. Bridge deck covered after concrete placement

Figure 3.26. Bridge after slip forming of barriers

Figure 3.27. Completed bridge open to traffic

4. MONITORING SYSTEM

Introduction

The SHM system deployed on the E. 12th St. Bridge was designed to achieve the objectives listed in the "Introduction" section. In addition, it was decided to use off-the-shelf and readily available technologies, when possible, in an effort to minimize development time.

The SHM system developed for and installed on the bridge can generally be divided into three sub-systems: the data acquisition sub-system (DASS), the gateway sub-system (GSS), and the data storage/processing sub-system (DSPSS). A schematic of the SHM system can be seen in Figure 4.1.

The flowchart shown in Figure 4.2 summarizes the data "flow" from their origin at the sensors to their final format. The primary sub-systems mentioned above, the hardware components of each sub-system, and software programs within them are shown in the flowchart. This chapter is organized in a manner similar to the organization of the Figure 4.2 flowchart.

Data Acquisition Sub-System (DASS)

The DASS, located at the bridge, collects raw data from strain sensors strategically located on the bridge and transfers the information to the GSS, which is located at a nearby secure facility. Components of the DASS include the following (manufacturing company in parentheses):

- Strain sensing equipment
    - 40 FBG sensors (Avensys, Inc./Bragg Photonics & LxSix)
    - Si425-500 Swept Laser Interrogator (Micron Optics, Inc.)
- Communication equipment
    - 2.4 GHz wireless-802.11g access point (Linksys)

Fiber Bragg Grating Sensors

FBG sensors are sensors "written" to a piece of conventional fiber-optic cable. Each FBG reflects a specific wavelength of light depending on the mechanical strain induced on the sensor or changes in sensor temperature. Thus, changes in the reflection wavelength are directly related to a change in strain or temperature. As mentioned above, because the FBG measurements are not dependent upon signal amplitude (only upon reflected wavelength), they are relatively stable over time. Also, this type of sensor is not affected by electromagnetic interference, radio frequency interference, or electric currents, which generally cause traditional sensors to "drift" with time and introduce random noise. In addition, multiple FBG sensors can be multiplexed on a single optical fiber, which reduces lead wire lengths and numbers.
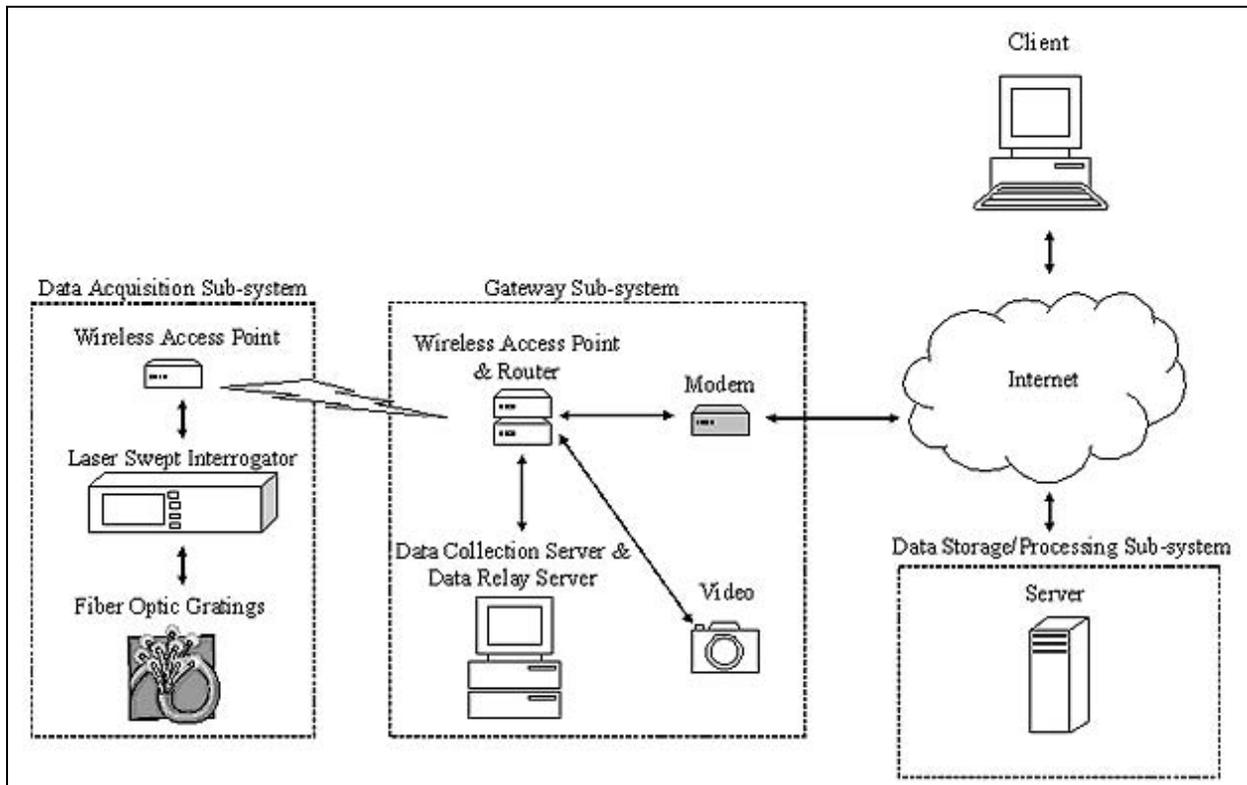
Figure 4.1. Schematic of the E. 12th St. Bridge SHM system

.
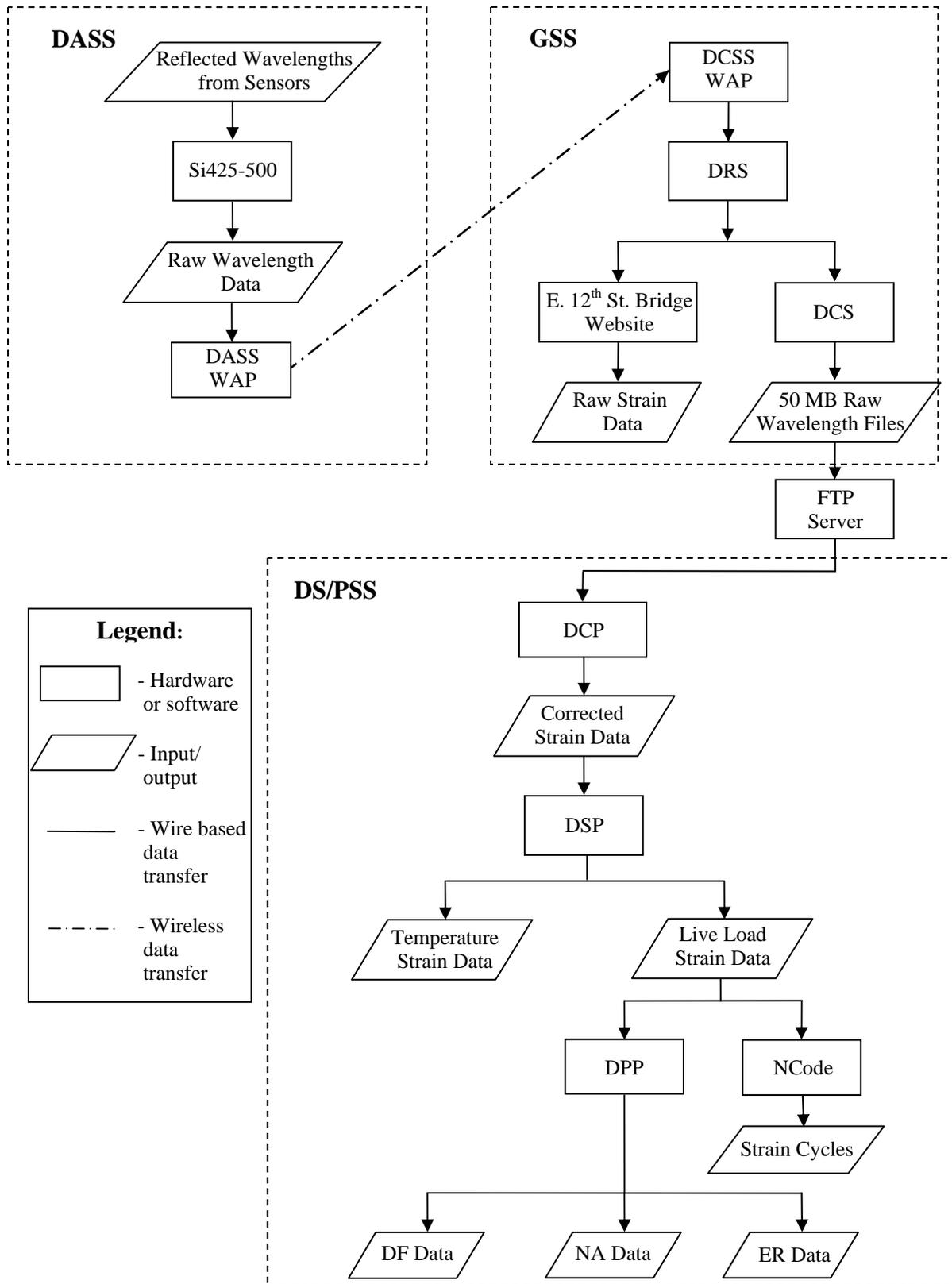
Figure 4.2. Data acquisition and processing flowchart

The flowchart contains the following labeled elements:

DASS
- Reflected Wavelengths from Sensors
- Si425-500
- Raw Wavelength Data
- DASS WAP

GSS
- DCSS WAP
- DRS
- E. 12th St. Bridge Website
- DCS
- Raw Strain Data
- 50 MB Raw Wavelength Files

- FTP Server

DS/PSS
- DCP
- Corrected Strain Data
- DSP
- Temperature Strain Data
- Live Load Strain Data
- DPP
- NCode
- Strain Cycles
- DF Data
- NA Data
- ER Data

Legend:
- Hardware or software
- Input/output
- Wire based data transfer
- Wireless data transfer

35

Sensor Locations

The FBG sensors installed on the subject bridge are located at strategic points on the bridge so that both the global and local performance of the bridge could be assessed. The sensors are located at the nine cross sections shown in Figure 4.3, referred to as CS A through CS I in the figure. The global performance is monitored with FBG sensors placed on the bottom flanges of all the girders and select top flanges (shown in Table 4.1 and Figure 4.4) near midspan of both the north and south spans (cross sections B and I, respectively). Top and bottom flange sensors were also placed near the north abutment on several girders (cross section A), and two girders were monitored with bottom flange sensors near the bridge pier (cross section D).
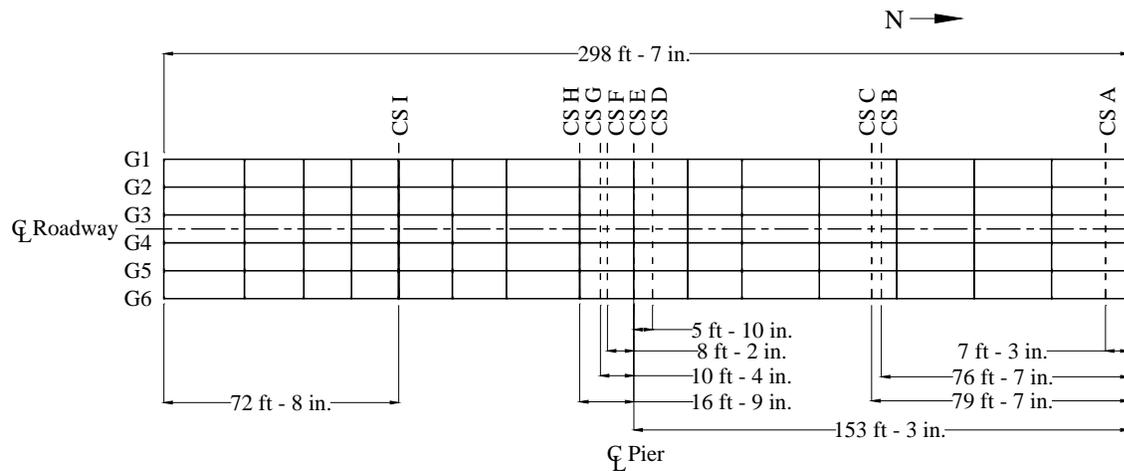

Figure 4.3. Plan view of the E. 12th St. Bridge showing the cross sections where sensors were installed

Localized strains near fatigue-sensitive details were monitored at several locations. The web gap regions of two girders were instrumented in the negative moment region near the pier. The web gap region was monitored with two different sensor configurations: a flange tipping configuration and a web gap bending configuration. (The exact placements will be described subsequently.) Two girders at cross section E were equipped with web gap sensors, and two girders at cross section H had both flange tipping and web gap sensors installed. Stress concentrations at both a flange (cross section G) and web (cross section F) welded splice were also monitored in the negative moment region near the pier.

FBG sensors were also placed at three locations on the bridge to measure the steel temperature, hereafter referred to as "temperature sensors." Unlike all of the previously described sensors, these sensors were not physically attached to the bridge. Therefore, the temperature sensors are isolated from mechanical strain, and shifts in their reflected wavelengths are related to temperature changes only. A final FBG sensor was placed in the protective cabinet, which will be discussed subsequently, that houses the data collection hardware. This allows the temperature in the cabinet to be monitored.

As stated above, the sensors were monitored on four different channels (each channel has multiple sensors). The channel from which each sensor is monitored depends only upon

36

installation convenience. Channel 1 consists of sensors 1 to 13, which are generally near the pier; channel 2 consists of sensors 14 to 29, which are located near midspan of the north span and the north abutment; channel 3 consists of sensors 30 to 39, which are near midspan of the south span. Channel 4 consists of the single FBG sensor monitoring the temperature in the protective cabinet located at the bridge pier. The locations of all sensors described above are listed in Table 4.1 and are shown in Figure 4.4. The cross section designations are shown in Figure 4.3. See Figures 4.5 through 4.7 for more detailed information about sensor locations.

Figure 4.5 illustrates the typical placement of the bottom flange FBG sensors (sensors 3, 4, 14, 17, 19, 20, 22, 24, 25, 26, 28, 31, 32, 33, 35, 37, and 38) and the top flange FBG sensors (sensors 15, 18, 21, 23, 30, 34, 36, and 39). These sensors are oriented longitudinally and centered between the face of the web and the edge of the flange. In all cases, the top flange sensors were placed on the bottom of the top flange and the bottom flange sensors were placed on the top of the bottom flange.

The typical placement of the flange tipping sensors (sensors 8 and 9) and the web gap sensors (sensors 1, 2, 7, and 10) are shown in Figure 4.6. The flange tipping sensors were oriented transversly on the girder top flange along the outside edge of the stiffener to measure the out-of-plane strain at the stiffener-flange interface. The web gap sensors were placed vertically on the girder web, centered at the intersection of the bottom of the web gap and the top of the stiffener.

The typical placement of the web splice sensors (sensors 5 and 12) and the flange splice sensors (sensors 6 and 11) are shown in Figure 4.7. The splice sensors were oriented longitudinally along the flange-web weld at locations where either the web or flange plates were spliced with weldments.

**Table 4.1. Sensor number, location, type, and channel number information**

| Sensor number	Girder number	Cross section	Type	Side of web	Channel number
1	3	E	Web gap	East	1
2	3	E	Web gap	West	1
3	3	D	Bottom flange	West	1
4	2	D	Bottom flange	East	1
5	2	F	Web plate splice	East	1
6	2	G	Flange plate splice	East	1
7	2	H	Web gap	West	1
8	2	H	Flange tipping	West	1
9	1	H	Flange tipping	East	1
10	1	H	Web gap	East	1
11	1	G	Flange plate splice	East	1
12	1	F	Web plate splice	East	1
13	1	E	Web gap	East	1
14	3	B	Bottom flange	West	2
15	2	B	Top flange	West	2
16	1	C	Bottom flange temperature	East	2
17	1	B	Bottom flange	East	2
18	1	B	Top flange	East	2
19	1	A	Bottom flange	East	2
20	2	A	Bottom flange	West	2
21	3	A	Top flange	West	2
22	3	A	Bottom flange	West	2
23	3	B	Top flange	West	2
24	2	B	Bottom flange	West	2
25	4	B	Bottom flange	West	2
26	5	B	Bottom flange	West	2
27	5	C	Bottom flange temperature	West	2
28	6	B	Bottom flange	West	2
29	6	C	Bottom flange temperature	West	2
30	1	I	Top flange	East	3
31	1	I	Bottom flange	East	3
32	2	I	Bottom flange	East	3
33	3	I	Bottom flange	East	3
34	4	I	Top flange	West	3
35	4	I	Bottom flange	West	3
36	5	I	Top flange	West	3
37	5	I	Bottom flange	West	3
38	6	I	Bottom flange	West	3
39	6	I	Top flange	West	3
40	--	--	Equipment temperature	--	4
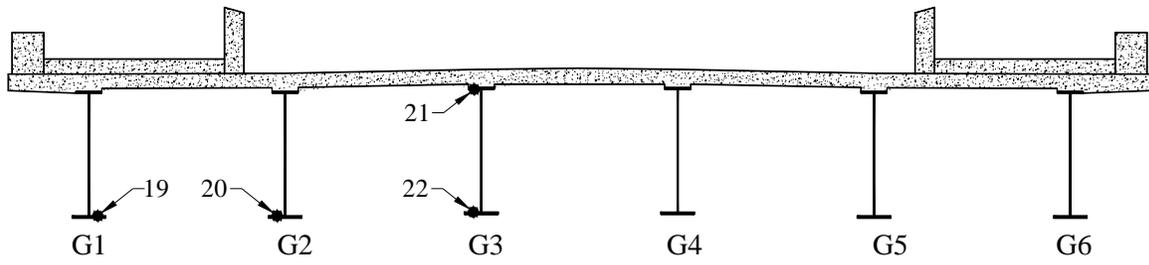
a. Cross section A
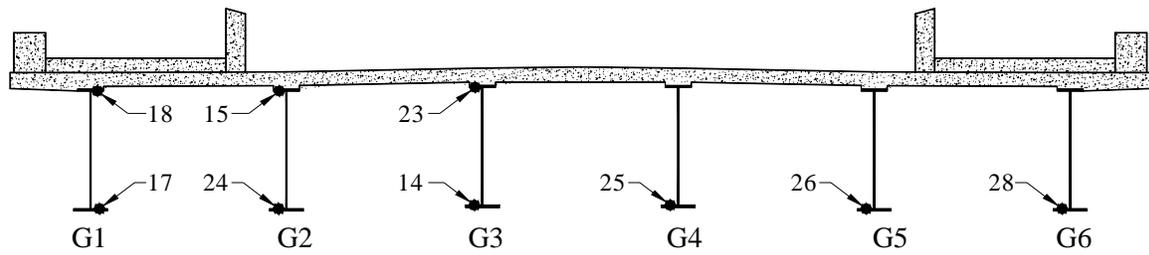
b. Cross section B
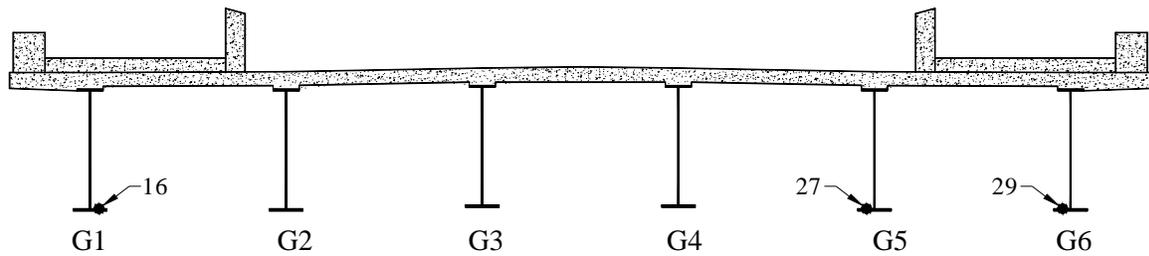
c. Cross section C
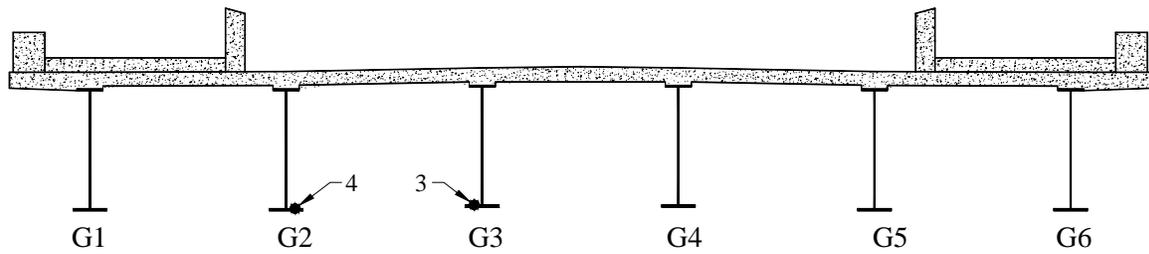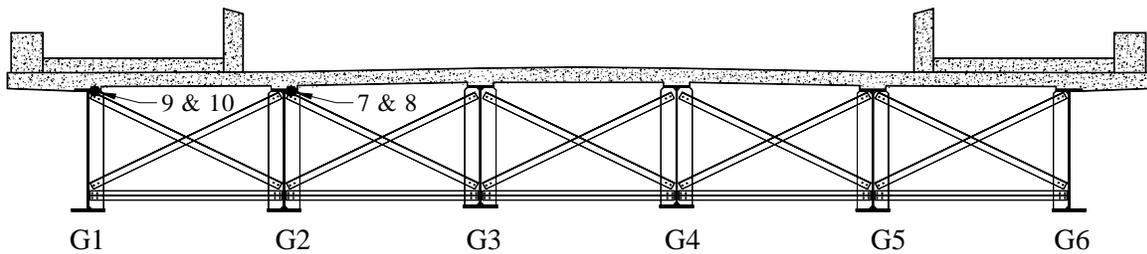

d. Cross section D
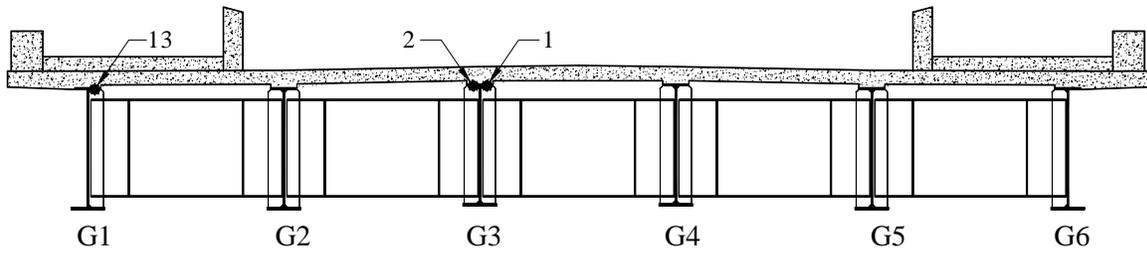
e. Cross section E
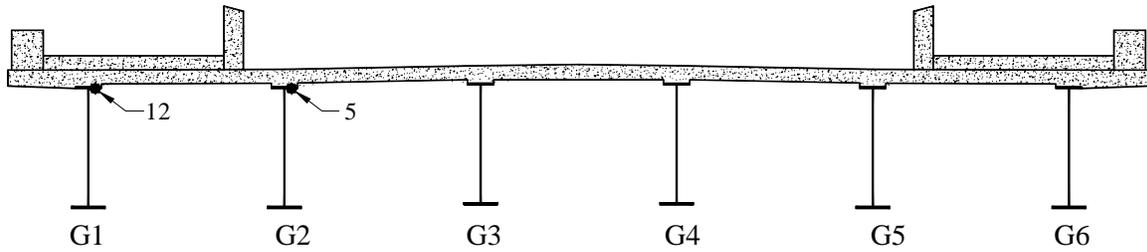
f. Cross section F
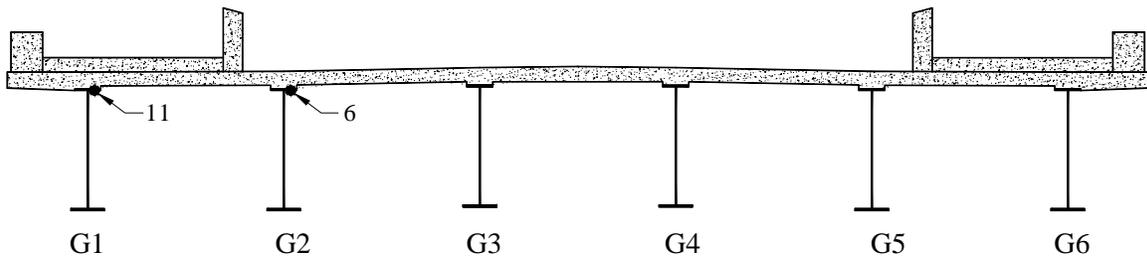
g. Cross section G

h. Cross section H
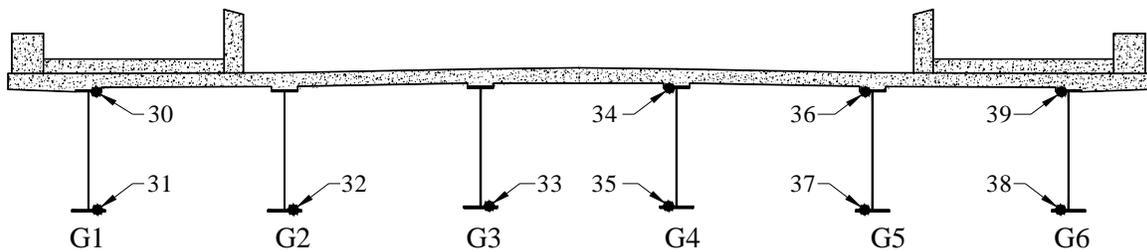
i. Cross section I

Figure 4.4. Sensor locations and designations looking north
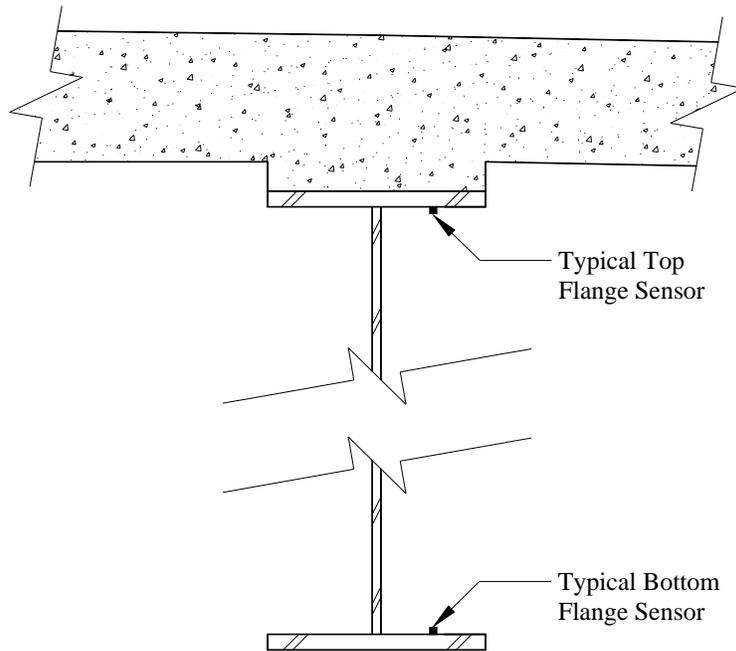
a. Typical top and bottom flange sensor placement
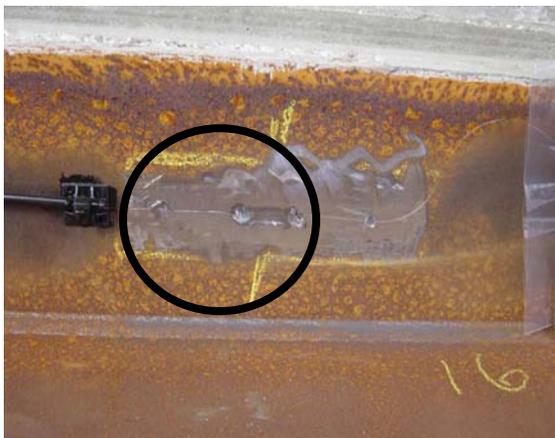
b. Typical top flange sensor   **c. Typical bottom flange sensor**

Figure 4.5. Typical top and bottom flange sensors
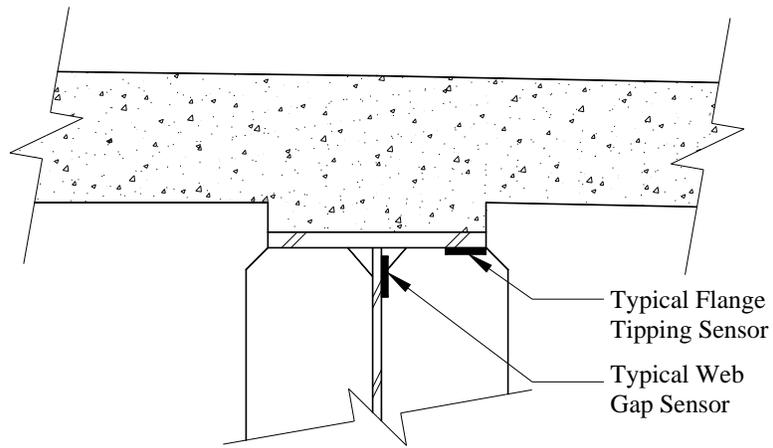
a. Typical flange tipping and web gap sensor placement

b. Typical web gap sensor (lower circle) and flange tipping sensor (upper circle)

Figure 4.6. Typical flange tipping sensor and web gap sensor
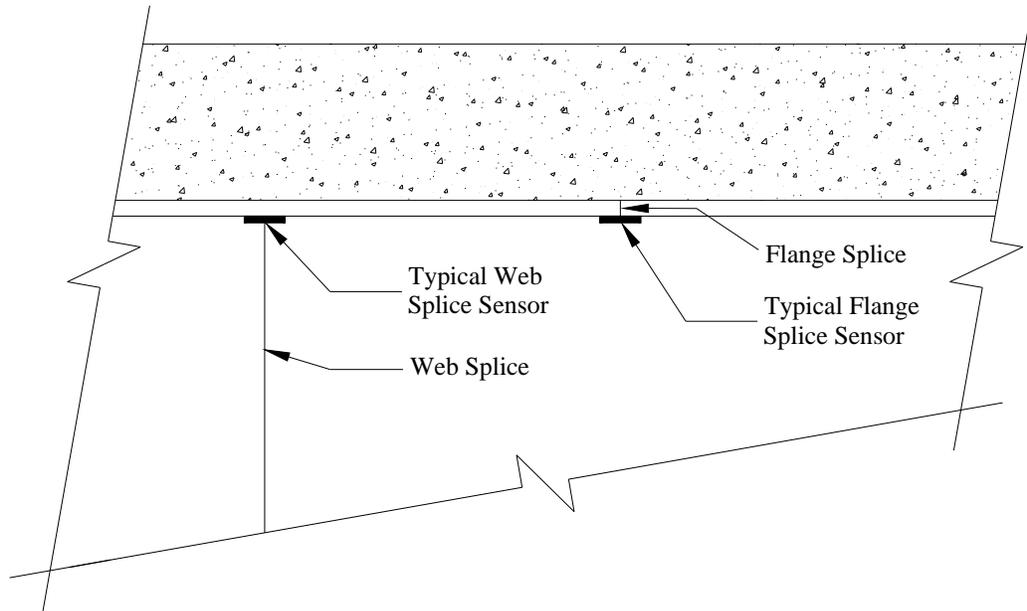
a. Typical splice sensor placement (elevation view)
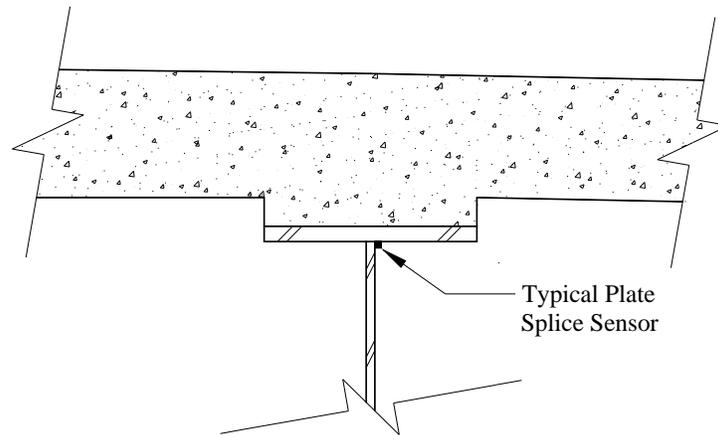
b. Typical splice sensor placement (cross-sectional view)

Figure 4.7. Typical plate splice sensor

Sensor Types

Three different forms of FBG sensors were used on the E. 12th St. Bridge:

- Bare FBG
    - Single sensors
    - Array of sensors
- Surface-mountable sensor

Single bare FBGs were used for 15 of the 40 sensors. These sensors, manufactured by AVENSYS Inc./Bragg Photonic Division, were written onto a SMF-28 fiber pigtail with no jacket. The pigtail distances on each side of the sensor were customized for the exact location of the sensor on the E. 12th St. Bridge. A bare sensor after installation can be seen in Figure 4.8.

Figure 4.8. Single bare FBG sensor after installation

An array of FBG sensors exists when several single bare FBGs are multiplexed onto a single continuous SMF-28 fiber pigtail. This type of sensor arrangement was custom manufactured by LxSix Photonics, Inc., for this project. Specified distances between the sensors were provided by the project team. Fifteen of the sensors on the E. 12th St. Bridge were installed in seven arrays of sensors. An installed single sensor multiplexed into an array looks the same as the single sensor illustrated in Figure 4.8.

A surface-mountable sensor is a single FBG sensor written into a pigtail with the sensor then embedded in an 8 x 3/4 in. piece of carbon fiber reinforced polymer. For the specific surface mountable sensors used in this project, FC/APC connectors were provided at the ends of the pigtails for multiplexing the sensors together. The ten surface-mountable sensors used on the subject bridge (sensors 30 to 39) were, again, manufactured by AVENSYS Inc./Bragg Photonic Division. Figure 4.9 shows a typical surface-mountable sensor. (Note that the surface-mountable sensors were received after the bare FBG sensors were installed, and the collection of associated data began at a later date. This will be apparent in the "Bridge Performance Indices" section.)
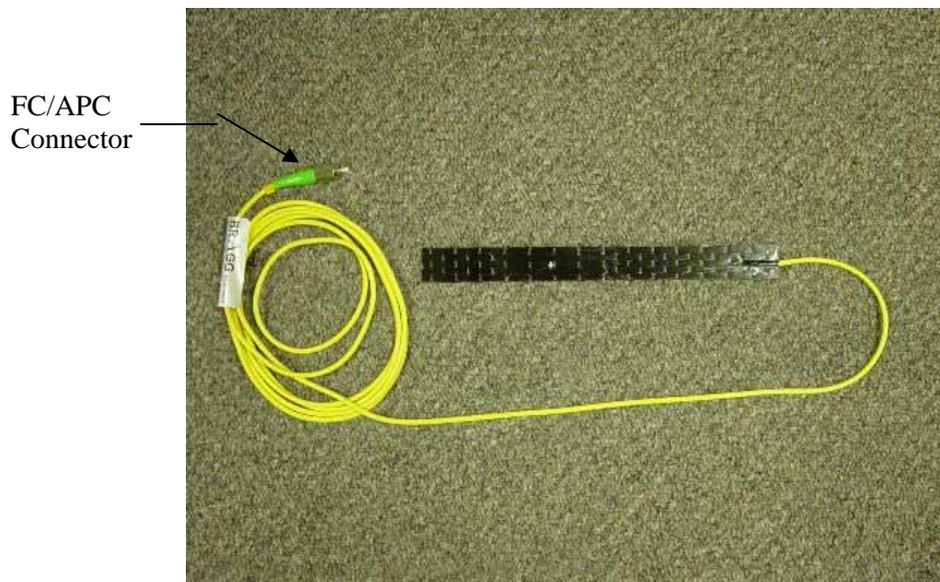
Figure 4.9. Surface-mountable sensor before installation

Jumper Cables

Fiber-optic jumper cables were used to multiplex groups of FBGs separated by longer distances. The jumper cable used on the subject bridge consisted of a round duplex cable with SMF-28 fiber, manufactured by Corning Cable Systems/Corning Division. Figure 4.10 shows a jumper cable that runs along the top flange of a girder to connect the Si425-500 and the first sensor on channel 2.

Splices

Splicing was performed to join individual fibers (either containing a sensor, an array of sensors, or a jumper). Two different types of splices were used on this project:

- Fusion splices
- Mechanical splices

Fusion splices consist of the aligned cores of two separate fibers that are then fused together. A Fiber optic splicing professional from Huxley Communication, located in Huxley, Iowa, performed the 37 fusion splices required for the project at a cost of $35 per splice. Figure 4.11 shows two fibers being fusion spliced together.

Mechanical splices consist of the previously mentioned FC/APC connectors at the ends of the surface-mountable sensors and FC/APC mating sleeves. Figure 4.12 shows a mechanical splice used on the bridge. Eleven mechanical splices were used during this project. To weatherize the splices (both fusion and mechanical), silicone was used to cover the spliced region. A weatherized fusion splice is shown in Figure 4.13.

Figure 4.10. Jumper cable installed on top flange of girder

Figure 4.11. Fusion splicing of two fibers
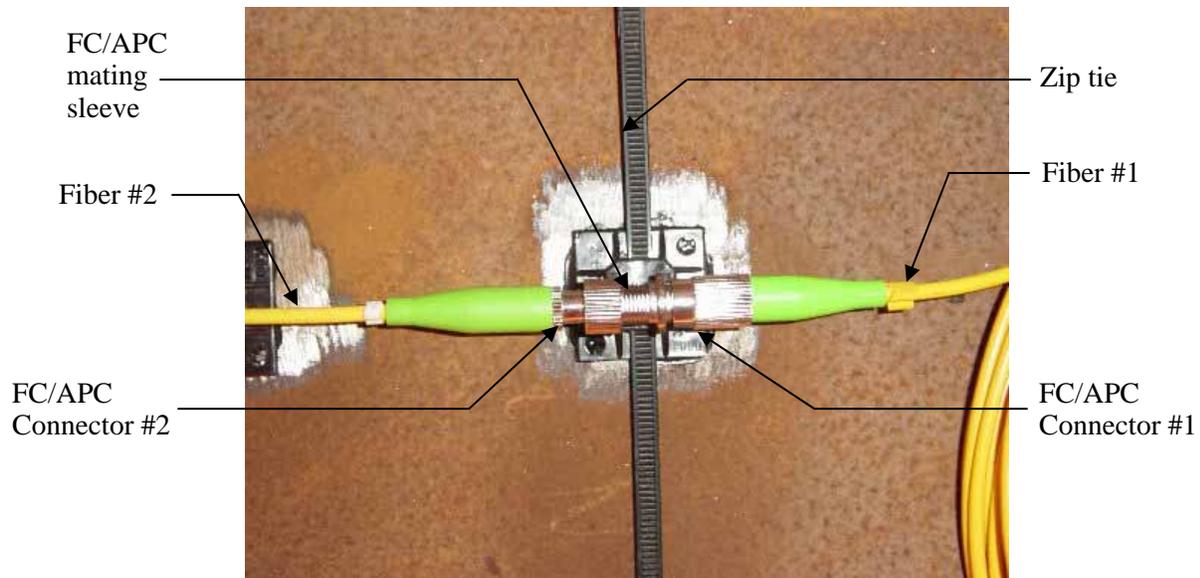
Figure 4.12. FC/APC mating sleeve connecting two fibers

Figure 4.13. Completed splice after silicone protection has been applied

Sensor Installation

Installation of the individual sensors began with surface preparation. A wire wheel on a hand-held grinder was used to remove the weathering layer from the steel. A hand-held grinder with a sanding disc was then used to polish the steel to a smooth finish. The area was then cleaned with a rag and acetone. The size of area prepared in this manner depended on the type of sensor being installed. The bare fiber FBG sensors required approximately a 6 x 1 in. area, while the surface-mountable sensors required approximately a 10 x 2 in. area.

The general approach for adhering the bare FBG sensors and the surface-mountable sensors is generally the same, but the details for each installation procedure depend somewhat upon the sensor type. The details for each installation procedure are described in the following paragraphs.

Bare FBG sensor: After the surface was prepared and the sensor properly aligned, a dot of epoxy was placed on the fiber-optic cable approximately 1 in. away from the sensor. After the epoxy had gained sufficient strength, a line of epoxy approximately 1/8 in. wide by 2 in. long was then placed on the steel where the sensor was to be placed. The sensor was then placed in the line of epoxy. After the epoxy had cured, another dot of epoxy was placed on the other side of the sensor. The function of the two dots of epoxy was to ensure that stress was not placed on the sensor if the fiber was inadvertently pulled taut. Figure 4.8 shows a sensor after these steps had been performed (the dots of epoxy on each side of the sensor can be seen, as well as the line of epoxy in which the sensor was placed). The epoxy used to install the bare FBG sensors was Loctite's Instant Adhesive, Clear 411. To decrease the set time, Loctite's 7452 Accelerator was used. The accelerator was misted over the epoxy following placement of the sensor. After the epoxy had fully cured, the area over and around the sensor was covered with silicone to protect it from environmental damage. A sensor covered in silicone is shown in Figure 4.14.

Surface-mountable sensor: After the steel surface was prepared in the manner discussed above, the steel surface was sprayed with Loctite's 7387 Activator. The side of the FRP sensor that was to be in contact with the steel was also sprayed with Loctite's 7387 Activator. After the activator had set, the contact side of the FRP was then coated with Loctite's Structural Adhesive, Rapid Fixture 39. The sensor was then correctly aligned and held in place for approximately 20 sec. until a bond was established. An installed surface mountable sensor is shown in Figure 4.15. After the surface mountable sensors were installed, they were also covered with silicone to protect them from damage.

Figure 4.14. Sensor covered in silicone

Figure 4.15. Installed surface-mountable sensor

Interrogator

The interrogator chosen for this project, the instrument that interprets and outputs the readings from the FBG sensors, was the Si425-500, manufactured by Micron Optics, Inc. Selected for its capabilities, size, and durability, the Si425-500 is a four-channel interrogator capable of reading up to 128 FBG sensors per channel. Maximum read rates are 250 Hz/channel for channels with less than 100 sensors and 125 Hz/channel for channels with more than 100 sensors.

The Si425-500 Swept Laser Interrogator (shown in Figure 4.16) is located at the hub of the DASS, which is centered on top of the bridge pier in the environmentally controlled steel cabinet (through the use of thermostats that control heaters and fans), pictured in Figure 4.17. The 35 lb. interrogator, which is approximately 17 x 17 3/4 x 5 1/4 in., has a published operating temperature range of 50°F to 104°F. The Si425-500 operates by emitting a broadband of light from a laser through each of the four data collection channels. Each of the sensors on the fiber-optic cable then reflects a single wavelength that the interrogator registers and stores. The Si425-500 is a wavelength-based interrogator, which means that the interrogator cannot determine the location of the sensor on the fiber-optic cable. Therefore, the reflected wavelength data are stored in ascending order. However, as long as one knows the initial reflected wavelength from each sensor, one can generally associate the unspecified location data with known locations.

The Si425-500 is constantly "listening" for a "read" command sent by the data relay server (DRS), discussed below). After receiving the command, the data stored in buffer by the Si425-500 are continuously transferred to the DRS in real-time until a "stop" command is given or the connection is terminated. The data are transferred from the Si425-500 using a static IP address and port, which are assigned to the Si425-500 through a TCP/IP connection. Due to the anticipated vehicle speeds and the projected end use of the data, a scan rate of 31.25 Hz was used in this project.

Figure 4.16. Front panel of the Si425-500 interrogator
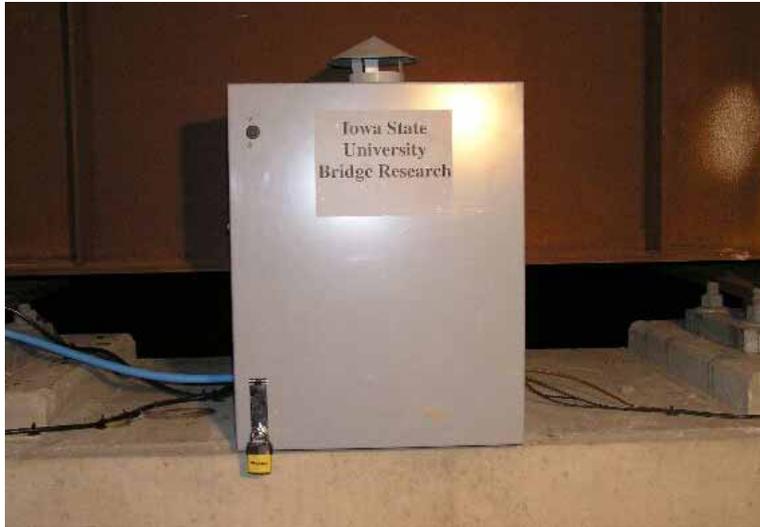
a. Steel cabinet

b. DASS equipment in steel cabinet

Figure 4.17. Steel cabinet on bridge pier that houses the DASS equipment

Wireless Access Point

The Si425-500 is connected to a Linksys wireless access point (WAP) using an Ethernet connection, creating a LAN (the DASS LAN) between the Si425-500 and the WAP. The DASS WAP transmits the raw data, in wavelength format, from the interrogator to another WAP, which is part of the GSS and located approximately 450 ft. from the bridge. Each of the WAPs have been assigned a static IP and configured to operate in wireless bridge mode, thereby allowing direct communication between the DASS LAN and the GSS LAN. The wireless data

51

transmission is protected by WEP2 (Wired Equivalent Privacy, 128 bits), and the service set identifier (SSID) is disabled to secure the network connection further.

To ensure reliable communication between the DASS and the GSS WAPs, the antennas for the DASS WAP were placed at the east edge of the bridge pier (see Figure 4.18) to provide line-of-sight communication between the WAPs. The use of the WAPs allowed transmission of the data between the DASS to the GSS without the need to run communications cable.

Gateway Sub-System (GSS)

The GSS, shown in Figure 4.19, is located in a secure building approximately 450 ft. from the bridge pier. Components of the GSS include the following (manufacturer in parentheses):

- Data management equipment (DME)
  - Data relay server (DRS)
    - Desktop computer – 700 MHz processor, 20.0 GB hard drive, 256 MB RAM (Gateway)
  - Data collection server (DCS)
    - Desktop computer – 733 MHz processor, 14.2 GB hard drive, 256 MB RAM (Dell)

- Communication equipment
  - 2.4 GHz Wireless-802.11g access point (Linksys)
  - 2.4 GHz Wireless-802.11g router (Linksys)
  - 678 DSL modem (Cisco)

- Video equipment
  - Canon VB-C10/VB-C10R network camera

The GSS WAP, DRS, DCS, DSL modem, and the video camera are all connected to one another by Ethernet cables through a Linksys router, which enables all of the GSS components to communicate with one another. All of the components were assigned a static IP address, thus creating a consistent GSS LAN. When data need to be transferred for permanent data storage (discussed subsequently) and client real-time data access, the Cisco 678 DSL modem is used. This modem has the ability to download at 1.5 MBps and upload at 1.0 MBps.

Figure 4.18. Data acquisition sub-system WAP antennas placed at the edge of bridge pier

Figure 4.19. Gateway sub-system located in secure facility near bridge

As stated above, raw wavelength data from the Si425-500 are transmitted to the GSS via the WAP, which then passes the data to the rest of the GSS via the router. The data are continuously called by the DRS from the Si425-500 using a TCP/IP connection. As the DRS continuously collects data, other applications can use a TCP/IP connection to the DRS to retrieve data in manner similar to the way the DRS collects the data from the Si425-500. When another application connects to the DRS (such as the DCS or the web line chart client, discussed below), the data stream is relayed to the other applications.

The DCS continuously obtains data from the DRS for processing and permanent storage. As the DCS downloads the data from the DRS, the binary data stream is parsed and converted to create ASCII text files of raw wavelength data. The ASCII files are automatically limited in size to 50 MB by a specially created data collection program; once the files reach the maximum size, they are saved and compressed. The compressed files are then automatically placed on an FTP server.

The data storage/processing sub-system (DSPSS), described below, automatically downloads and removes the files from that FTP server.

As stated above, a website provides live strain data along with a live video stream (http://www.ctre.iastate.edu/bec/structural_health/e12thst_dsm.cfm). When the website is accessed, the web line chart client program retrieves the live wavelength data from the DRS, converts it to strain, and transmits it to the website via a web portal. The interactive website allows the user to choose the sensor location from which the strain data is displayed. A Java application connects to the camera via HTTP to provide the live video stream.

Data Storage/Processing Sub-System (DSPSS)

Data Storage/Processing Overview

The DSPSS, housed at the Bridge Engineering Center (BEC) in Ames, Iowa, about 50 miles from the E. 12th St Bridge, is where the data files are permanently stored and processed. DSPSS components include the following:

- Data management equipment
  - Dell PowerEdge 4600 server - 3.0 GHz Processor, 1.2 TB hard drive, 4.0 GB RAM

After the wavelength data files are received at the BEC (via the FTP process described above), the wavelength data are checked and, if necessary, corrected to ensure that problems do not occur (discussed below), and the files are converted to strain data. Several processes are then performed to ensure that the entire system is operating properly, eliminate temperature strain from the complete strain record, compute global behavior indices of the bridge, and count strain cycles at the various sensor locations.

Temperature effects are eliminated to allow the long-term effects of live load on the bridge to be assessed. After eliminating temperature effect, the global behavior of the bridge is monitored by computing distribution factors (DF), neutral axis locations (NA), and end restraint ratios (ER). By monitoring these basic structural characteristics, a conceptual understanding of the time-dependent performance can be gained.

Rainflow counting is used to count the number and magnitude of strain cycles at the various sensor locations. With sufficient data, the results from the strain cycle counting can then be used to evaluate the susceptibility of the details to failure and possibly to estimate remaining life.

Data Storage/Processing Sub-System Software

Data Correction Program

To alleviate problems within the raw wavelength data (discussed in the following sections), the research team developed a data correction program. The program uses the absolute difference

between the last known good wavelength reading and the incoming raw data to select current readings that correspond to previously known good readings. In the event that extra data (extra sensor columns) are present, this procedure determines the valid data values.

The program then goes through a series of checks to determine whether the above process results in duplicate data entries selected for multiple sensors. Such an occurrence indicates that an insufficient amount of sensor columns was present in the raw data. The application again uses the absolute difference to determine the correct and incorrect duplicate values. The duplicate data entry that is incorrect is then "zeroed," resulting in a line of data referred to as the "zeroed corrected" data line. The program then repeats the procedure for the next line using the data from the "zeroed corrected" data line as the new last known good wavelength reading.

After an entire file is processed, the "zeroed" data entries are interpolated between the last and most recent valid known data for each sensor. The interpolation is performed so that abrupt discontinuities in the data are not created. The corrected wavelength data are then converted to strain data. It is important to note the data in the sensor columns that have been "zeroed" and interpolated are not considered reliable data by the research team. The correction program allows the reliable data to be extracted from the data stream and relayed to the research team in a format that is compatible with the remaining data processing software.

Data Sorter Program

As stated above, the DSPSS performs several functions, some of which are performed by the data sorter program (DSP). The DSP performs basic checks of the data integrity; finds the minimum, maximum, and average strain value for each sensor in the file; and creates a time history of both the temperature and live load strain records.

The DSP, developed by the research team, is adaptable to any data set that has a time, buffer, and temperature column in addition to the sensor columns. As shown in Figure 4.20, the user must enter the location of the time, buffer, and temperature columns, along with the beginning and ending locations of the sensor columns. For the E. 12th St. Bridge, the time is in Column 1, the buffer in Column 2, the sensors in Columns 3 to 41, and the temperature in Column 42. Multiple files can be selected at once, and the DSP will process them sequentially.
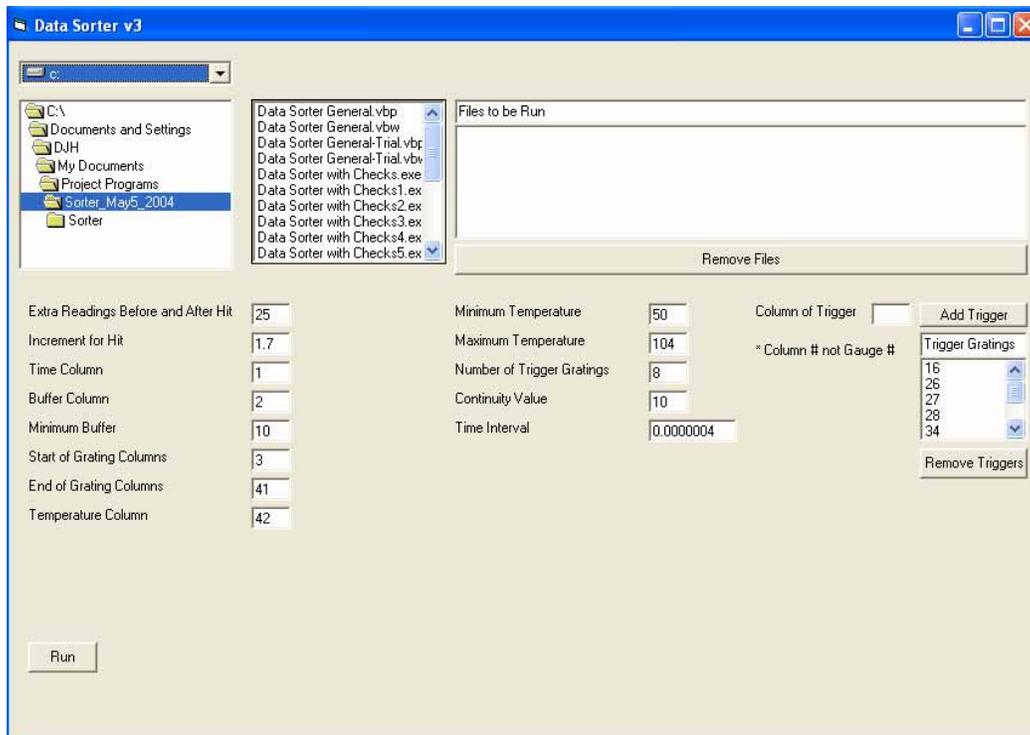
Figure 4.20. Screenshot of the DSP user interface

The following basic data integrity checks are performed:

- Time Gap determines whether two consecutive time values differ by more than the specified read speed. The difference between two successive time values is found, and if the difference is greater than the number entered into the Time Interval box (shown in Figure 4.20), a warning with the time of the occurrence is generated. This check is completed to ensure continuity in the data collection process and proper system operation.
- Buffer Check alerts the user if the buffer (a measure of the amount of the Si425-500's internal memory being used) drops below a specified threshold. If any value in the buffer column drops below the value entered in the Minimum Buffer box (shown in Figure 4.20), a warning with the time of the occurrence is generated. The buffer check allows the research team to monitor the data collection process. If the buffer value repeatedly drops, issues with the data collection software may be occurring.
- Continuity Check informs the user if the difference between two consecutive readings of one sensor is larger than a specified threshold. If the difference between two consecutive readings of one sensor is larger than the threshold specified in the Continuity Value box, a notice appears at the completion of the program's operating period. The continuity check is used to indicate a malfunction in a sensor or the data acquisition system.
- Temperature Check informs the user if the steel cabinet containing the data acquisition equipment drops below or rises above specified temperatures. If a value in the temperature column is less than the value entered in the Minimum Temperature box or greater than the value entered in the Maximum Temperature box (shown in Figure 4.20), a warning with the time of the occurrence is generated. This check ensures that the

56

environmental controls (heater, fans, vents, etc.) of the DASS protective box are functioning properly.

The DSP also creates a "minimum, maximum, and average" file. As the name indicates, the file consists of the minimum, maximum, and average reading for each sensor within a file. This statistical information can be useful to the research team for monitoring long-term trends of the sensors.
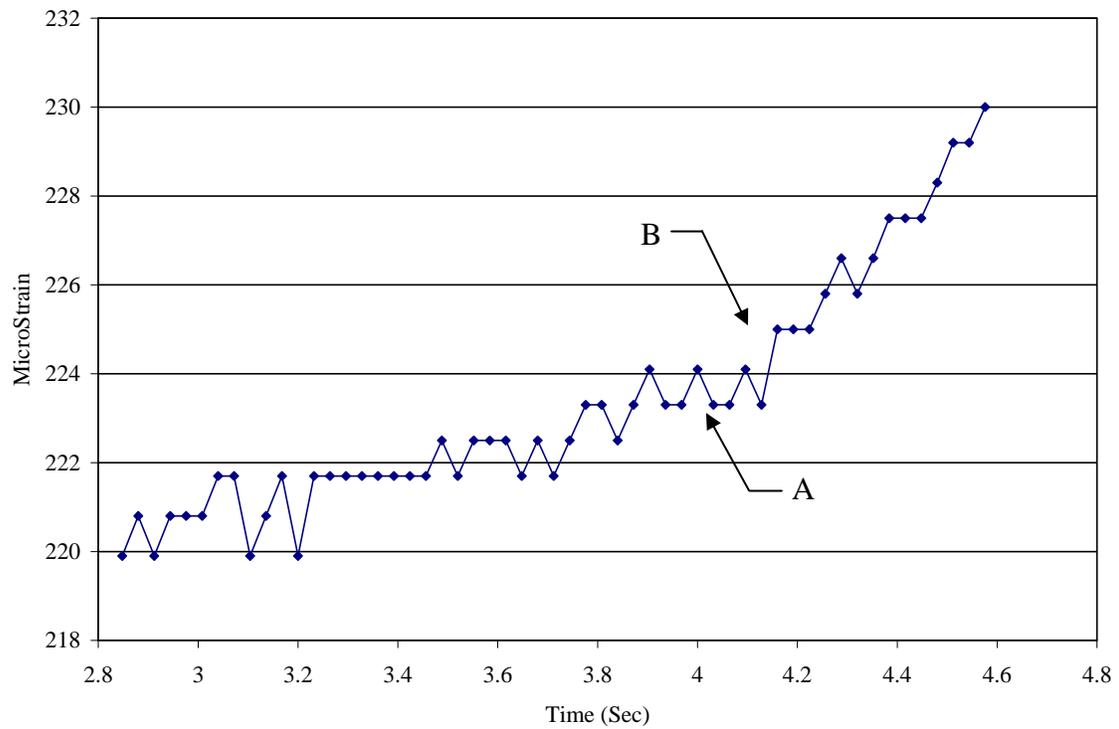
The temperature/traffic separation routine in the DSP is based on the concept that if one knows the temperature strain time history, one can subtract that time history from the raw strain time history to generate the live load strain time history. The algorithm developed for the DSP identifies traffic events based on machine-coded structural behavior concepts and removes those time periods from the raw data file. A file is created (called the temporary temperature file) that contains raw strains with gaps where traffic events occurred. Since the traffic events last a short time, the temperature effects during the traffic event are assumed to vary linearly from the beginning of the traffic event to the end. Linearly interpolated data points are then generated appropriately to complete the temperature strain file during periods when the traffic events occurred. The values in the complete temperature file are then subtracted from the values in the raw data file and a traffic file is created.

Traffic events are identified by searching for rapidly changing portions of the raw strain record. To accomplish this, the difference in raw strain between every fourth reading is computed. For example, points A and B in Figure 4.21 are compared to the "Increment for Hit" value entered as shown in Figure 4.20. When the difference exceeds that value, a traffic event is "identified." This comparison is performed every fourth reading, rather than every reading, to reduce false call occurrence.

To reduce processing time, the DSP is designed so that a limited number of sensors can be selected as "trigger" sensors, whose data are used to identify traffic events in the process described above. When the data in one of the trigger columns signify an event, the row in which the event occurs and a specified number of rows before and after the event are stored as the traffic event. To ensure that the entire traffic event is captured, the user can specify an additional number of readings to be considered part of the traffic event. The number of rows stored before and after a trigger is set by the DSP user through the Extra Readings Before and After Hit box, shown in Figure 4.20. The number of readings before and after the event that best captures the whole event depends on the location of the trigger sensors and the speed and properties of typical passing vehicles. For the E. 12th St. Bridge, 25 readings before and after a trigger event worked appropriately well.
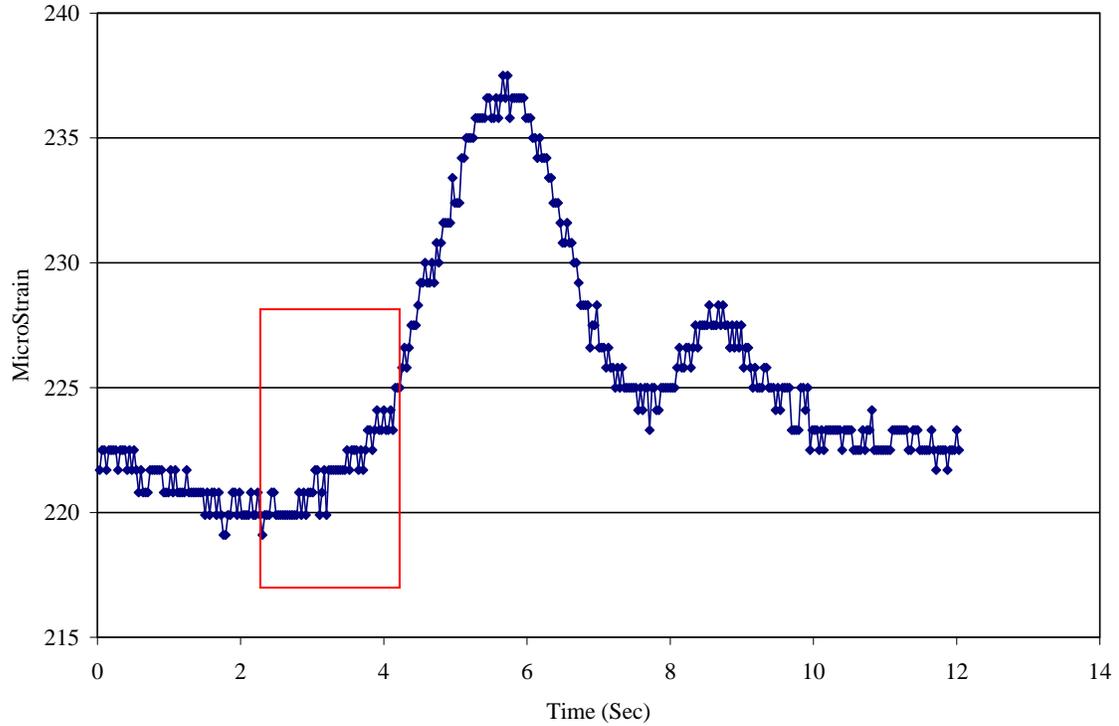
a. Traffic event in the raw strain data

b. Strain data in the box shown in 4.21a

Figure 4.21. Temperature/traffic separation process

There are several limitations to the type of bridge that the DSP developed for this project. During the day, the bridge must have a minimum number of time periods during which no traffic is present. In other words, enough temperature-only behavior needs to occur such that an accurate temperature strain time history can be generated.

To illustrate the separation process described above, Figure 4.22 shows an example set of raw data that DSP has processed. When the raw data for nine days are globally examined, it is immediately clear that the temperature effects for each day are larger than the live-load effects. After processing, the temperature-only data (Figures 4.22c and 4.22d) show a smoother trend without the peaks caused by the live-load effects. The traffic data (Figures 4.22e and 4.22f) show that strains are centered near the 0.0 me axis, as one would expect.

Data Processor Program

The data processor program (DPP) calculates several engineering parameters and indices that can be used to monitor the performance of the bridge over time. The DPP was designed specifically for the E. 12th St. Bridge SHM system and is not applicable to other data sets without changing the underlying computer code. The process in which a file is selected to be run through the DPP is the same as the process used for the DSP; the DPP also allows multiple files to be selected and run in succession to one another. To compute the various indices, the appropriate check boxes must be selected. The DPP user interface is shown in Figure 4.23.

The distribution factor (DF) is calculated at cross sections where there are bottom flange sensors on each girder laterally across the bridge. This occurs at the midspans of both the north and south spans of the bridge. The DF for each girder at each midspan is found by dividing the strain on the bottom flange of the particular girder at the particular cross section by the sum of all of the bottom flange strains at that particular cross section, as shown in Equation (1).

$$DF = \frac{\varepsilon_n}{\varepsilon_1 + \varepsilon_2 + \varepsilon_3 + \varepsilon_4 + \varepsilon_5 + \varepsilon_6} \quad \text{or} \quad \frac{\varepsilon_i}{\sum_{i=1}^{n=6} \varepsilon_n} \tag{1}$$

Where: ε_n = Strain from girder of interest
ε_1 = Strain from girder 1
ε_2 = Strain from girder 2
ε_3 = Strain from girder 3
ε_4 = Strain from girder 4
ε_5 = Strain from girder 5
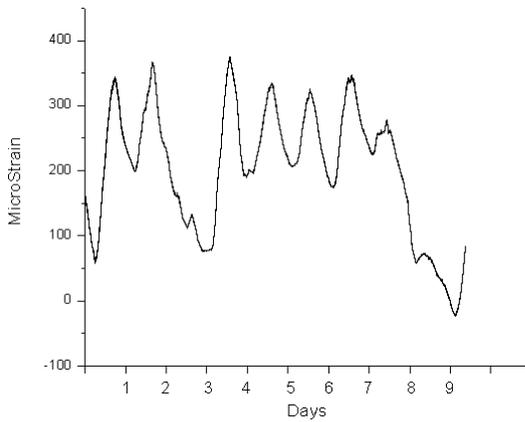ε_6 = Strain from girder 6

The DF is only calculated when the sum of the strains is greater than the threshold entered in the box labeled Minimum Total Strain in Figure 4.23. A DF file is created that has the DF for each girder at each cross section. Table 4.2 summarizes the sensors involved in calculating the DF at each cross section.
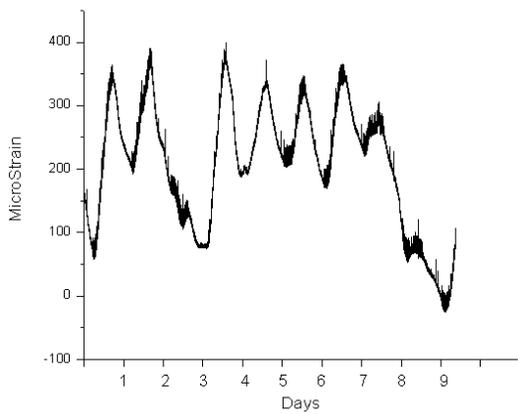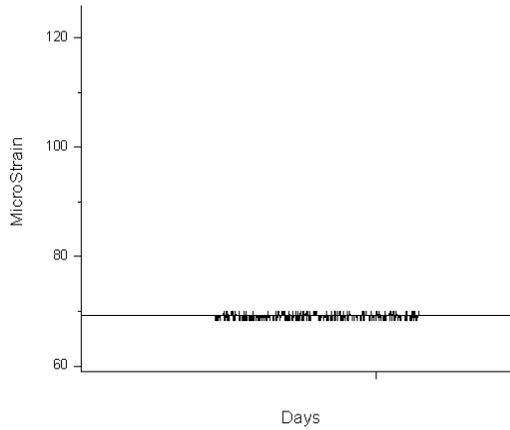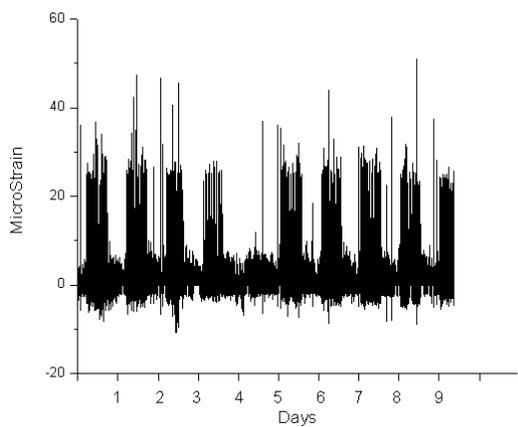
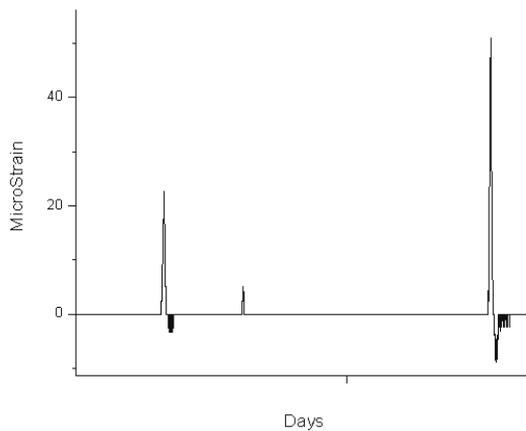**a. Raw data - 9 days**
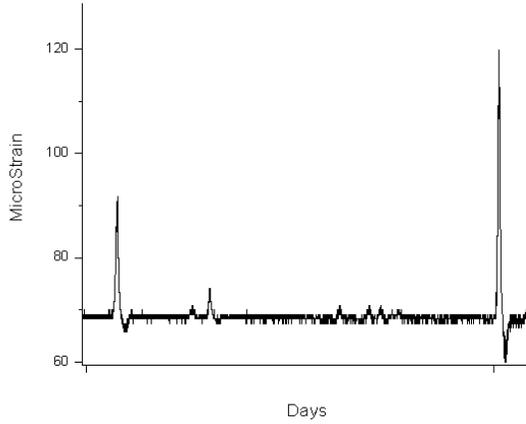
b. Raw data - 1 minute

c. Temperature data - 9 days

d. Temperature data - 1 minute

e. Traffic data - 9 days

f. Traffic data - 1 minute

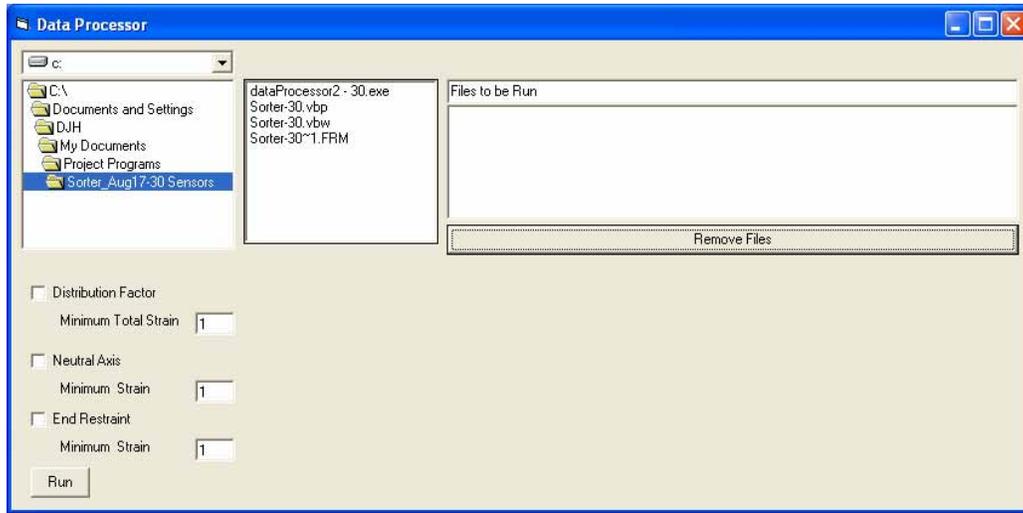**Figure 4.22. Raw temperature and traffic data for nine days and one minute**

Figure 4.23. Snapshot of the DPP user interface

Table 4.2. Sensors used in the distribution factor calculation

Description	Sensors
North midspan DF	17, 24, 14, 25, 26, 28
South midspan DF	31, 32, 33, 35, 37, 39

The neutral axis (NA) is calculated at points on the bridge where a sensor is on both the top and bottom flange of a girder at the same cross section. The distance of the NA from the bottom of the bottom flange is found by Equation (2):

$$NA = (\frac{\varepsilon_{BF}}{\varepsilon_{BF} - \varepsilon_{TF}})d_w + t_{BF}$$ (2)

Where: e_{BF} = Bottom flange strain
          e_{TF} = Top flange strain
          d_w = Web depth
          t_{BF} = Bottom flange thickness

The NA is only calculated when the bottom flange reading is greater than the value entered in the box labeled Minimum Strain, next to the Neutral Axis check box in Figure 4.23. The NA file, similar to the DF file, is created that has the NA locations listed for each time the NA is calculated. The FBG sensors used in the NA calculation are summarized in Table 4.3. The NA Position column is the designation used for identification purposes and will be used in subsequent sections.

61

Table 4.3. Sensors used in the neutral axis location calculation

NA position	Sensors
G1N	17, 18
G2N	24, 15
G3N	14, 23
G1S	31, 30
G4S	35, 34
G5S	37, 36
G6S	38, 39

The end restraint (ER) is determined for the three girders that have bottom flange sensors at the north integral abutment bridge. To monitor for changes in the longitudinal stiffness characteristics, the ratio of the strain on the bottom flange at the midspan to the strain of the bottom flange at the integral abutment is calculated in Equation (3):

$$ ER = \frac{\varepsilon_{MS}}{\varepsilon_{AS}} \tag{3} $$

Where: e_{MS} = Midspan bottom flange strain
         e_{AS} = Abutment bottom flange strain

As with the DF and NA, the ER is only calculated when the strain at the midspan of the bottom flange of the girder is greater than the value in the Minimum Strain box, next to the End Restraint check box in Figure 4.23. Table 4.4 lists the sensors used for the ER ratio, calculated by the DPP, and the girder number by which the ratios are identified.

Table 4.4. Sensors used in the end restraint ratio calculation

Girder	Sensors
1	19, 17
2	20, 24
3	22, 14

Averaging Programs

Programs were also developed to compute the average of the DF, NA, and ER files created (a separate program for each type of file). The programs create an Average File, which has an entry for each file averaged. So, for instance, if 30 DF files (30 days worth of data, for example) were processed by the DF average program, the output file would have 12 columns of data (two DFs for each girder, one for the north midspan and one for the south) and 30 rows (each row representing the average for one DF file). Using the average values from a single day, it is postulated that changes in the bridge performance indices might indicate changes in structural performance that could be related to damage and/or deterioration.

Rainflow Counting

The cycle counting method, rainflow counting, is used to determine the number and magnitude of strain cycles occurring at each senor location. Rainflow counting is performed on the traffic files only. Therefore, the number of strain cycles the bridge sees due to traffic loading is computed, and cyclic temperature cycles are not considered.

To prepare the files for rainflow counting, a program, Rainflow Extract, was created to generate a file containing only the strain data; therefore, columns such as time, buffer, and temperature are excluded. The output from Rainflow Extract is input into nCode's ICE-flow 2.0, which is commercial software capable of performing the rainflow counting procedure. ICE-flow is multifunctional software that allows the user to create many different processes using "glyphs," which are preprogrammed common routines used in data processing (i.e., basic and advanced mathematical and statistical functions, filtering, graphing, rainflow counting, etc.). For this project, a process was created that performs rainflow counting on a data set created by the Rainflow Extract program. The "Duty Cycle" function in ICE-flow is then used to combine the tabular output (the number of cycles for the each strain range) from each file, creating one table with the total number of cycles for each strain range from all of the files entered into the duty cycle. The final step is to convert the duty cycle output, which is in an ICE-flow format, into a comma delimited file using another ICE-flow process. Figure 4.24 shows the sample rainflow counting results in the form of a histogram for a typical week of data from a midspan bottom flange sensor.
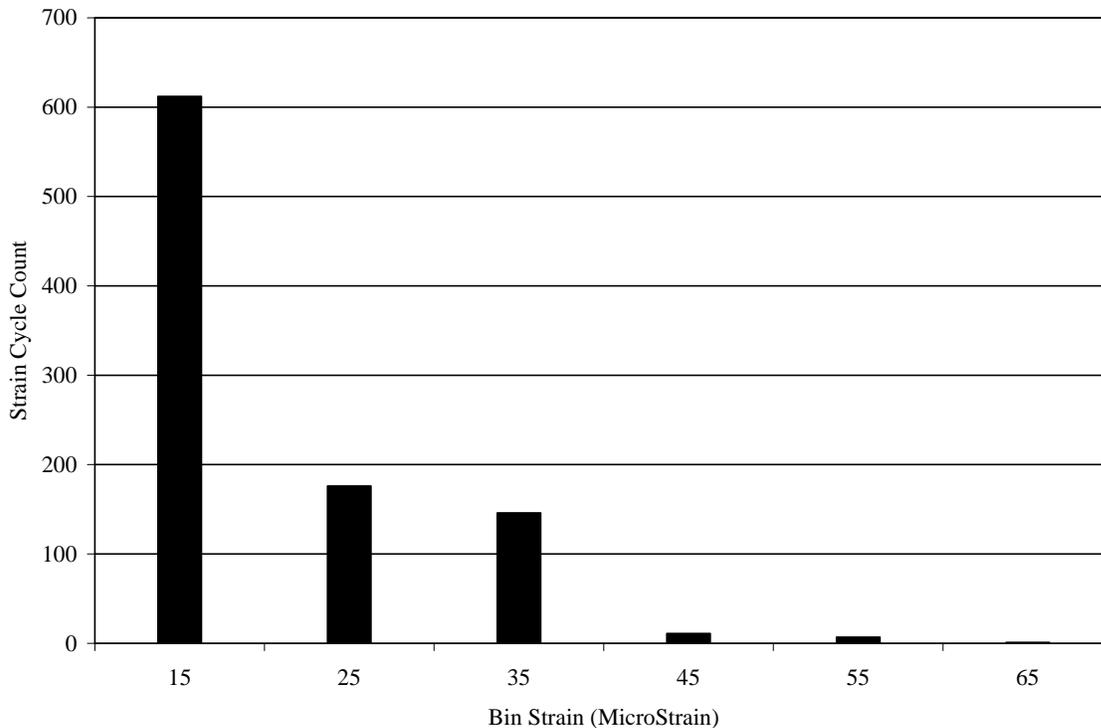

Figure 4.24. Strain cycles for one-week at the bottom flange of north midspan of girder 3

5. PERFORMANCE

The performance of the E. 12th St. Bridge and the structure health of the subject bridge were evaluated through multiple techniques, as discussed above. Information presented in this chapter is from the controlled load test, which was used to validate the performance of the FBG sensors. The responses of the bridge to random ambient traffic events are also evaluated. The bridge indices described in the previous section are presented for the controlled load tests and for ambient traffic during the monitored period of the bridge.

FBG Sensor Performance

To verify the accuracy of the FBG sensors during the live loading events, a controlled load test was performed. Of the 36 sensors used to measure the strain on the bridge, 23 had strain transducers, made by Bridge Diagnostics, Inc. (BDI), placed adjacent to the sensors. (The BDI transducers used a different acquisition system for data collection.)

Controlled Load Test Methods

The controlled load test was performed by collecting strain data while a truck of known weight and configuration was driven across the bridge. The configuration of the load truck used in the load test is shown in Figure 5.1. The front axle weight of the truck was 15,120 lbs., and the rear axle weight was 31,680 lbs. Table 5.1 summarizes the truck weight. The controlled load test consisted of nine runs; several runs were conducted at each location for repeatability. Runs 1 and 2 were conducted with the center of the west rear wheels 2 ft. from the west barrier rail. The truck was centered on the bridge for runs 3, 4, 7, 8, and 9. Runs 5 and 6 were conducted in a symmetrical fashion to runs 1 and 2 on the other side of the bridge, with the east rear wheel 2 ft. from the east barrier rail. The positions of the truck for the different runs of the load test are shown in Figure 5.2. Runs 1 through 6 were performed at crawl speeds, run 7 at 15 mph, run 8 at 25 mph, and run 9 at 35 mph. Runs 7 through 9 were conducted to collect data for dynamic observation. All of the runs were conducted with the vehicle traveling from north to south. Photographs of the truck before and during the load test are shown in Figure 5.3.

The FBG strain data from the load test were processed in the same manner as the ambient traffic data by first separating the temperature and live load traffic effects and then calculating the bridge performance indices.

Table 5.1. Axle weights of load truck for controlled load test (lbs.)

Front axle	Rear axles	Total
15,120	31,680	46,800
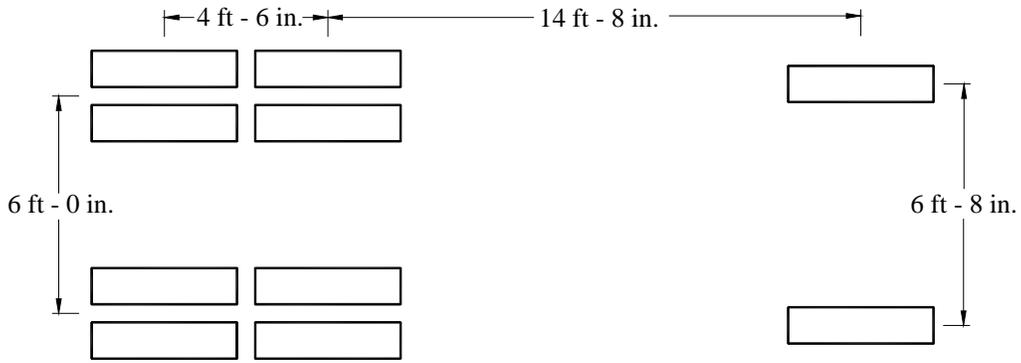
Figure 5.1. Configuration of load truck

4 ft - 6 in.

14 ft - 8 in.

6 ft - 0 in.

6 ft - 8 in.

Rear Axles Front Axle

2 ft - 0 in.

G1　　　　G2　　　　G3　　　　G4　　　　G5　　　　G6

a. Runs 1 and 2

G1　　　　G2　　　　G3　C̸L Truck　G4　　　　G5　　　　G6
　　　　　　　　　　　　C̸L Bridge

b. Runs 3, 4, 7, 8, and 9

2 ft - 0 in.

G1　　　　G2　　　　G3　　　　G4　　　　G5　　　　G6

c. Runs 5 and 6
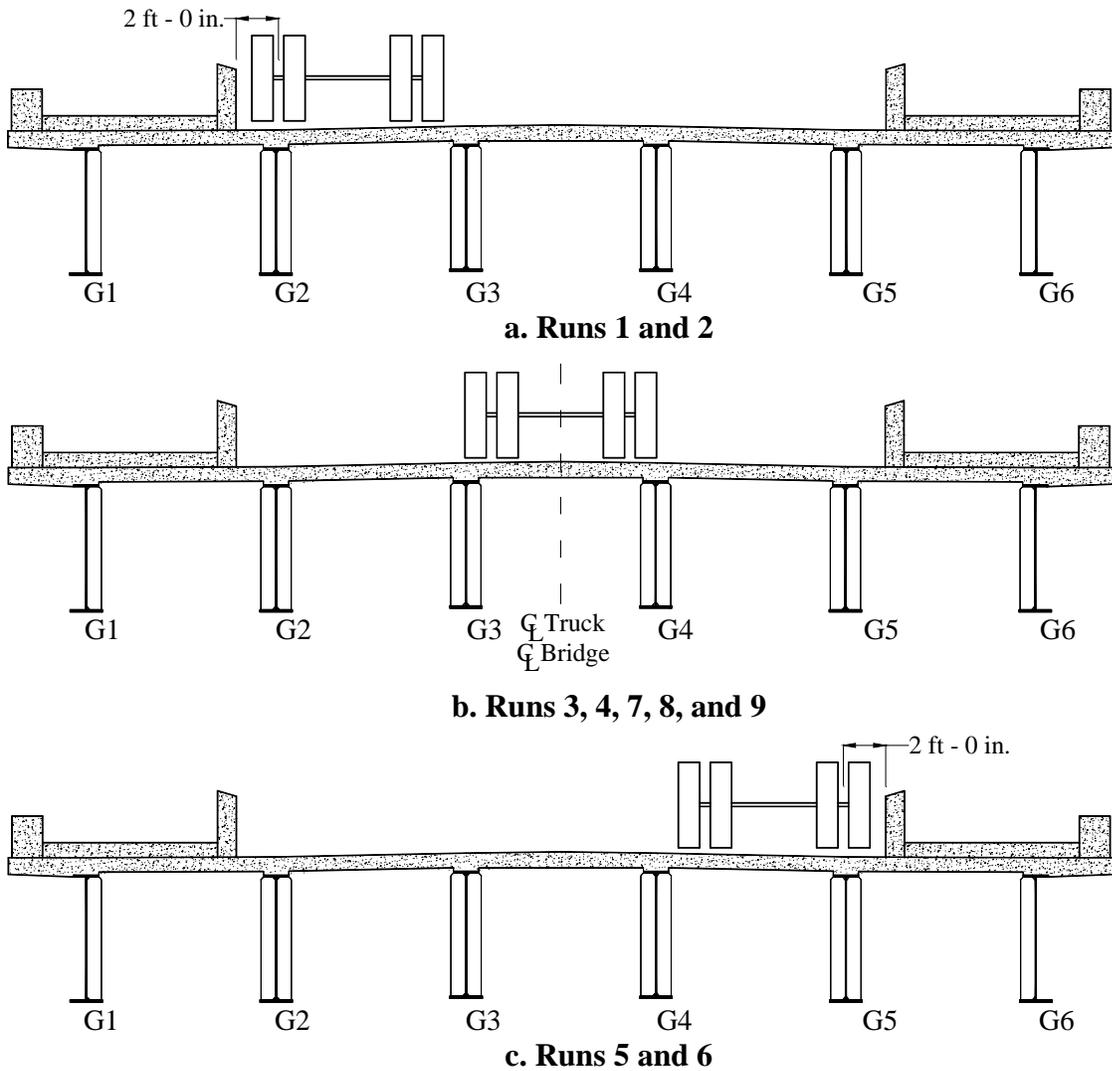
Figure 5.2. Position of load truck for the controlled load test looking north

a. Load truck prior to controlled load test

b. Load truck during run 2 of the controlled load test

Figure 5.3. Load truck used for the controlled load test

FBG Sensor Verification

Table 5.2 compares the peak strain results from the FBG sensors and the BDI strain transducers for run 2 of the controlled load test, in which the comparison results are typical for all of the controlled load tests. Due to location restrictions for BDI gage installation, the comparison was only performed for top and bottom midspan and abutment sensors. The differences in the strain measured by the FBG sensors and BDI transducers are listed, as well as the percent difference. The percent difference is considered no difference (ND) if the FBG reading, BDI reading, or difference between the two is less than 5 me. After reviewing the results of the load test comparison, only one sensor was considered unreliable under live load conditions. The girder 1 bottom flange sensor (sensor 19) at the abutment was consistently different than the BDI transducers.

Table 5.2. Comparison of peak strains for FBG sensors and BDI transducers from run 2 of

the controlled load test (values in microstrain)

FBG sensor #	FBG strain	BDI strain	Difference	% Difference
14	42	40	2	ND
15	8	8	0	ND
17	36	34	2	ND
18	1	4	-3	ND
19	-13	-28	15	54%
20	-26	-26	0	ND
21	3	2	1	ND
22	-18	-23	5	22%
23	-8	-3	-5	ND
24	48	49	-1	ND
25	20	19	1	ND
26	10	10	0	ND
28	3	3	0	ND
30	3	3	0	ND
31	39	37	2	ND
32	50	53	-3	ND
33	42	44	-2	ND
34	-3	-3	0	ND
35	22	23	-1	ND
36	-2	-1	-1	ND
37	12	13	-1	ND
38	3	3	0	ND
39	3	1	2	ND

ND = no difference

The FBG sensors and the BDI transducers were also compared by reviewing the strain time
history from the controlled load test. Typical results from runs 3 and 6 are presented here.
Generally, the time histories compare very well. The exception to this is the girder 1 bottom
flange abutment sensor, as discussed above and shown in Figure 5.4 (the BDI strain does not
return to zero probably because slippage of the epoxy between the BDI transducer and the steel).
Figure 5.5 shows the strain plots from a midspan bottom flange sensor with a relatively large
strain magnitude, in which the sensors follow the same profile with similar magnitudes. A
bottom flange location with a lower strain magnitude is shown in Figure 5.6, with fairly good
accuracy between the two sensors. A top flange location with a very small strain magnitude,
which also includes several localized strain spikes, shown in Figure 5.7, illustrates very good
correlation. Notice that even with high levels of oscillations (from "noise"), shown in Figure 5.8,
the different sensors behave similarly. Also shown in these figures is the difference in the
magnitude of the noise band between the different types of sensors. The information presented in
Table 5.2 and Figures 5.4 to 5.8 confirms that the majority of the FBG sensors are performing
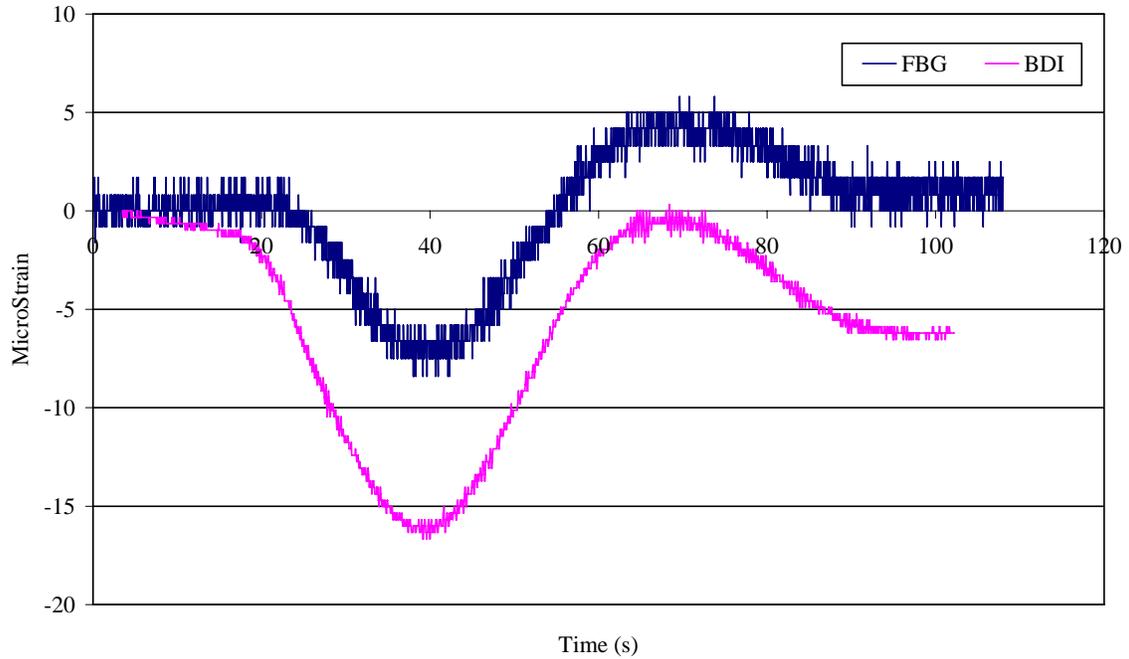accurately under short-term loading conditions.

Figure 5.4. FBG and BDI strain comparison from the bottom flange of girder 1 at the abutment, run 3 of the controlled load test
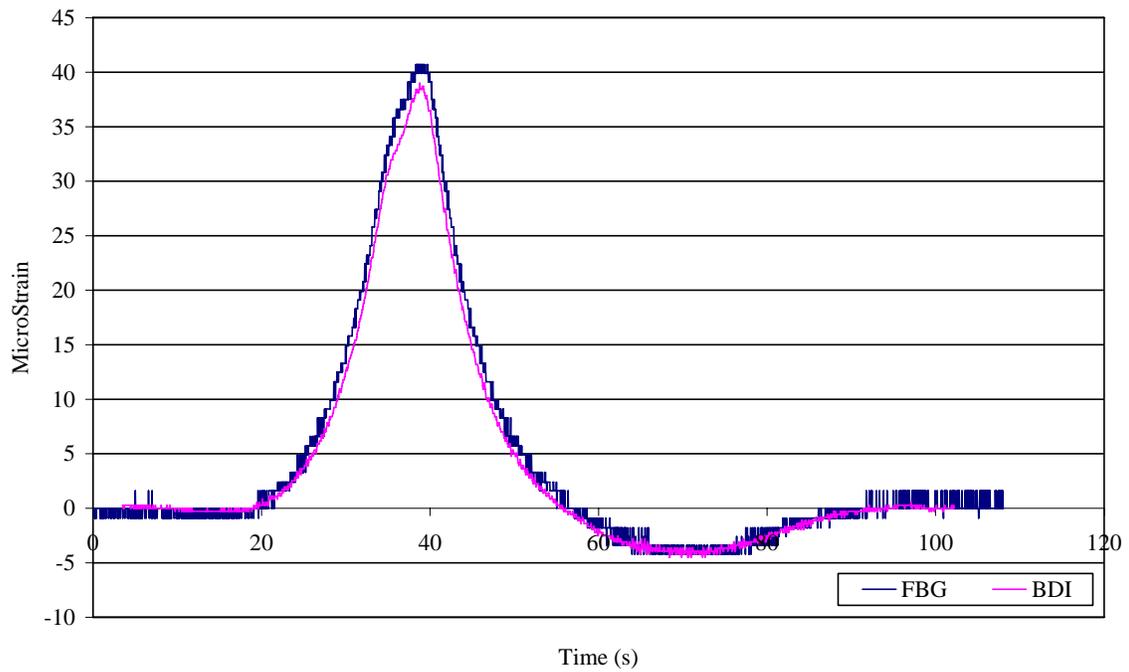

Figure 5.5. FBG and BDI strain comparison from the bottom flange of girder 4 at the north midspan, run 3 of the controlled load test
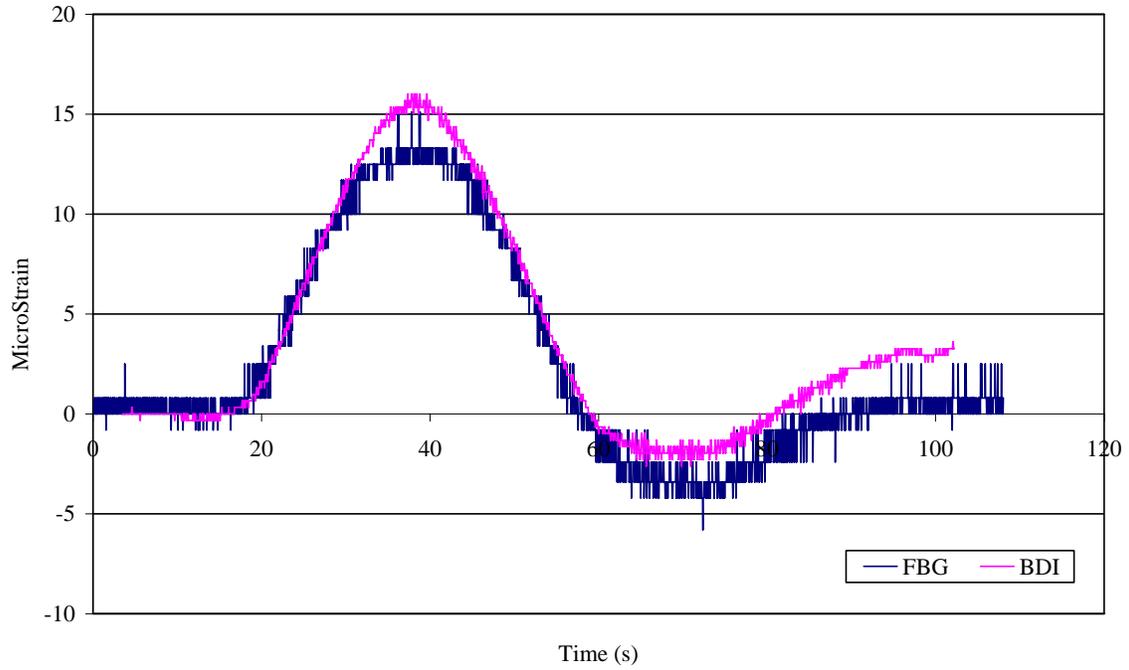
Figure 5.6. FBG and BDI strain comparison from the bottom flange of girder 6 at the north midspan, run 3 of the controlled load test
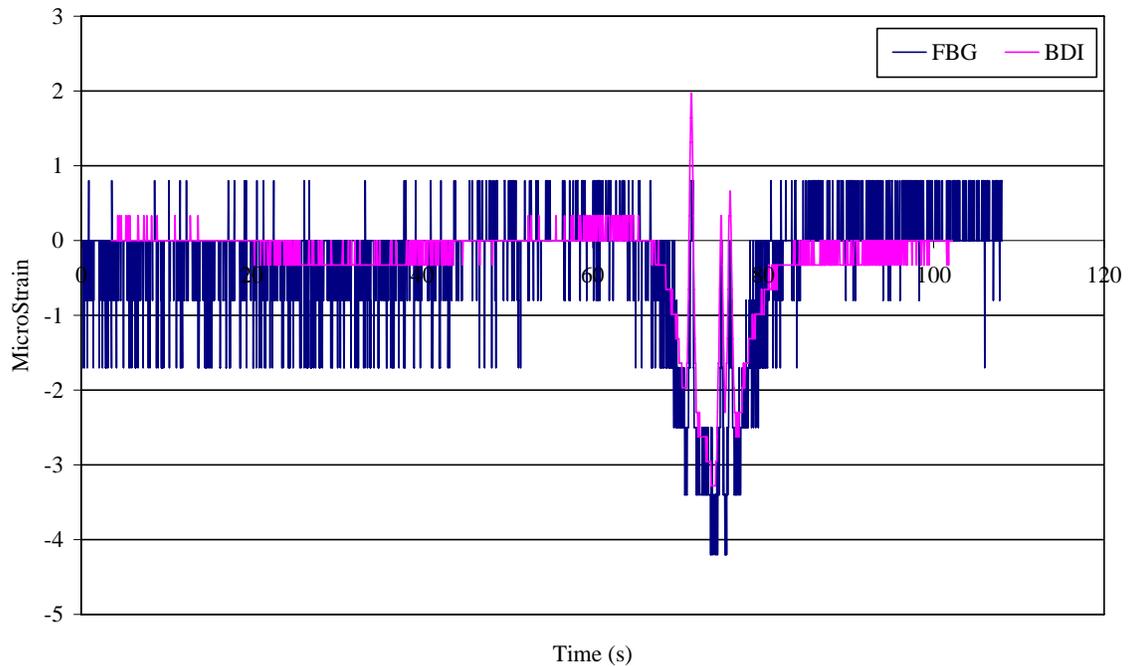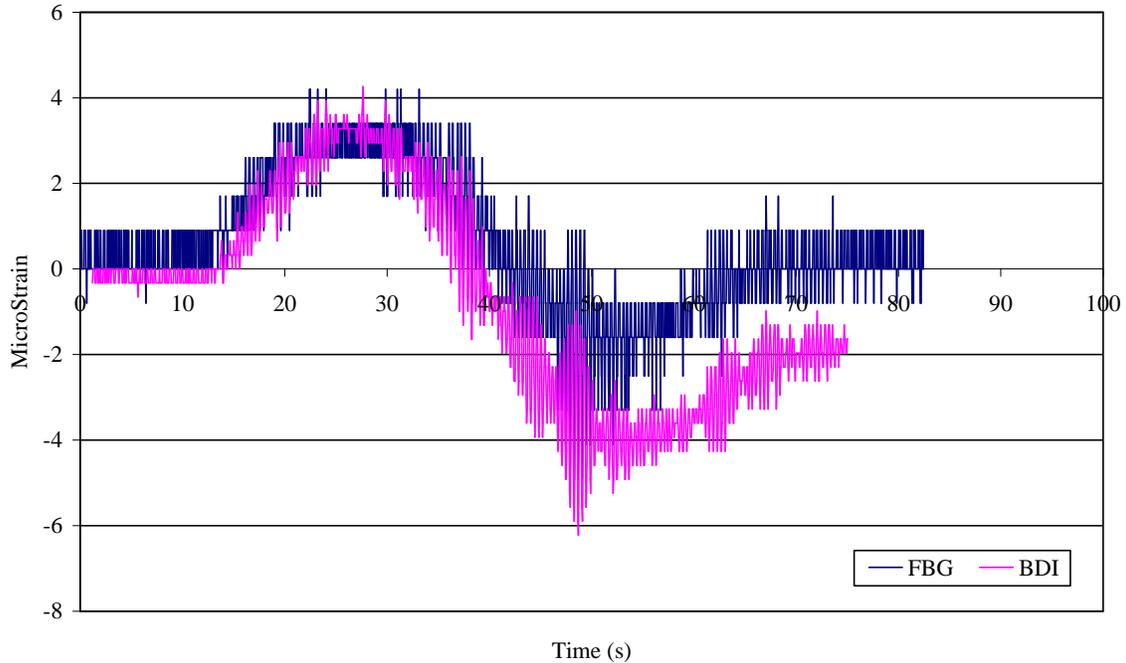

Figure 5.7. FBG and BDI strain comparison from the top flange of girder 4 at the south midspan, run 3 of the controlled load test

Figure 5.8. FBG and BDI strain comparison from the bottom flange of girder 1 at the north midspan, run 6 of the controlled load test

FBG Sensor Performance Issues

Although the sensors were shown to perform well under short-term loading, several problems have appeared that may be related to the performance of the sensors, including the following:

- Optical loss
- Interference between sensors
- Large strain range of sensors
- Large compressive drops
- Backscatter

Optical Loss

When the instrumentation scheme for the bridge was designed, channel 1 had 14 sensors. After all 14 sensors were installed and the system was powered, only 13 sensors initially responded. The fusion splice between sensors 13 and 14 was completed again to ensure that the splice provided a quality connection between the two cables. With still only 13 sensors appearing, sensor 14 was replaced, but sensor 14 still could not be found by the interrogator. Sensor 14 was then considered non-existent, but was left intact with the rest of the channel 1 sensors.

On several occasions when the temperature rose to approximately 50°F above the installation temperature (80°F to 90°F), data from sensor 13 were also not obtained. This phenomenon leads

the research team to believe optical loss in the system is the cause of the initial and subsequent problems with sensors 13 and 14. The hypothesis is that when the temperature rises and the bridge experiences thermal expansion, the fiber is tightened. In some places where the fiber needed to be curved, the fiber is then pulled too tight, creating too small of a radius. This prevents the higher wavelengths of light from reaching the end of the FO cable on channel 1.

Interference between Sensors

The data collected from the bridge have been problematic at various times (starting less than a month after the system was functional), with two adjacent sensors interfering with each other. The problem occurs when the wavelengths from at least two sensors are so close together that the Si425-500 can not distinguish between the sensors. This seems to occur when the difference approaches approximately 0.5 nm; at that point, only one wavelength reading is returned. A 3.0 nm center wavelength spacing was used for adjacent sensors for channels 1 and 2. The problem appears when a data set has a column of data missing and large differences in subsequent sequential readings from a sensor (approximately a magnitude of 3000 me).

Another issue related to this problem is the wavelengths of two adjacent sensors crossing. In this case, two sensors' wavelengths converge, cross, and then diverge. Unfortunately in this case, the data from the two sensors become unusable if a distinguishable characteristic between the two sets of data cannot be found.

Large Strain Range of Sensors

Some of the sensors on the bridge (from channels 1 and 2) had larger strain ranges (difference between daily maximum and minimum strains) than did other sensors. The ranges for these sensors have also increased since the system was installed. Possible reasons for this include the following:

- Change in the global physical properties of the bridge
- Change in the local physical properties of the bridge in the area of the sensor
- Sensor locations are more susceptible to temperature change
- Localized effect on the sensor (sensor not fully adhered to bridge)
- Sensor malfunction

At this time, the research team has not fully determined the source of the problem. The most likely cause is thought to be a localized effect on the sensor, such as epoxy loosening its bond with the bridge. This phenomenon could be the result of unsatisfactory installation, faulty adhesive, or insufficient sealing of sensors, which could allow moisture into the sensor area.

Large Compressive Change

A large compressive change in strain was noticed at different points in time from several of the various sensors on channel 1 and channel 2. One of the decreases was of a magnitude of 400 mε. These sharp decreases could be due to the following:

- Change in the global physical properties of the bridge
- Change in the local physical properties of the bridge in the area of the sensor
- Localized effects on the sensor (e.g., epoxy bond failure)
- Sensor malfunction

The cause of the decrease is yet to be isolated, but a localized effect on the sensor is currently thought to be the cause. The effect could be due to the loosening of the epoxy bond with the bridge, thus causing a residual force from the epoxy to be transferred from the attached surface to the sensor.

Backscatter

At various times through the monitoring period, extra data have been recorded. This situation would indicate that the interrogator is detecting sensors that do not exist. The problem has generally occurred on channel 1. The research team believes this problem is due to backscatter. Backscattering generally occurs from an inadequate termination of the fiber-optic cable at the end of the channel. Recall that 14 sensors were installed on channel 1, but only 13 sensors were recognized by the interrogator. These two issues may be related; however, a visual verification and repair of the problem have not been performed due to access limitations.

Summary

Although problems have occurred, which could be the result of installation defects or performance of the bare FBG sensors, a system has been created, through programs developed by the research team, to verify the accuracy of the data and produce only valid data for each sensor. It is important to note the short-term accuracy of the majority of the sensors is still acceptable (this was verified by the controlled load test). Due to the sensor problems discussed above, the long-term accuracy of some of the sensors may be unreliable.

The surface-mountable sensors (the FBG sensors bonded by FRP) have performed excellently, and the research team has very high confidence in their performance (both short- and long-term). The FRP sensors are highly recommended by the research team due to their ease of installation, robustness, and accuracy.

Bridge Performance

In this section, the performance of the bridge under live load events is evaluated in several ways. The first is by examination of the strain data from random ambient traffic on the bridge as well

as the strain data from the controlled load test. The second is by presentation of the bridge indices discussed earlier (distribution factor, neutral axis, and end restraint), which are calculated by the DPP. The indices are shown for both a short-term event (i.e., the controlled load test) and for long-term data from ambient traffic over the monitored life of the bridge. The strain cycle counting results for ambient traffic are also presented.
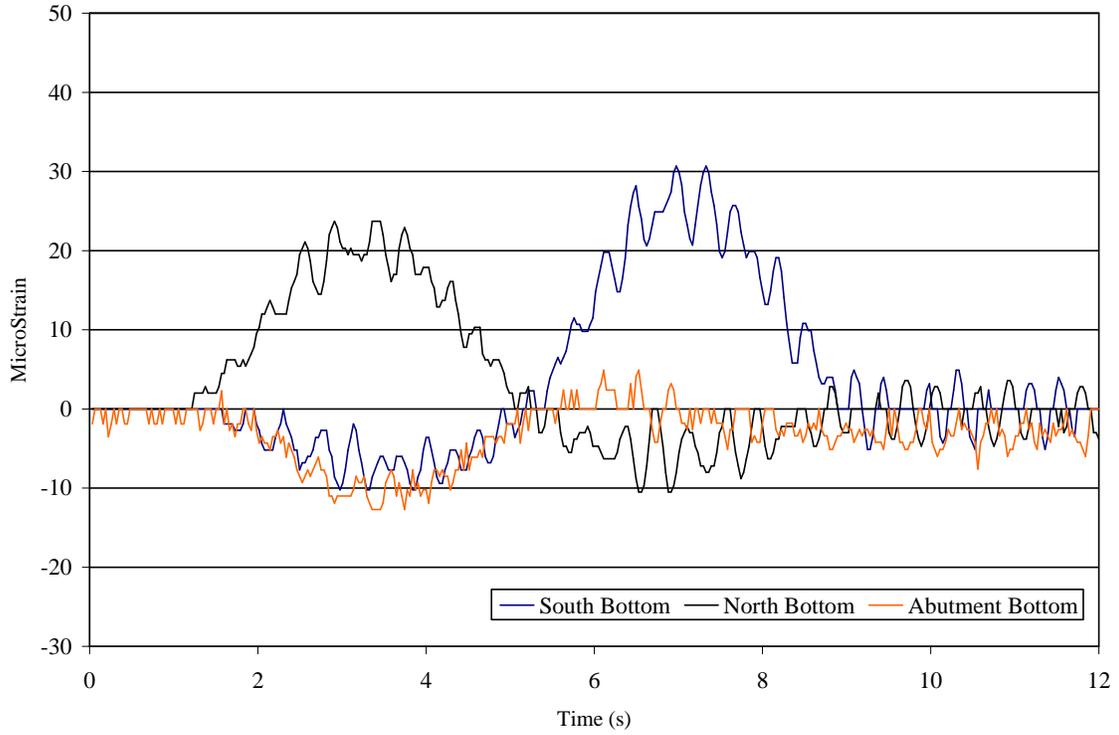
Bridge Response to Ambient Traffic Events

The data collected and processed from ambient traffic events on the bridge occurred over a one-year period (and is continuing) for south midspan sensors and over four months for other sensors. The real-time data and video from the bridge were helpful for the research team to become familiar with the general response of the bridge and the general vehicle population. Because the video was not recorded, the sizes and positions of the vehicles were unknown in most instances. Therefore, the information collected from the events had to be analyzed and studied to find information that was useful to the research team for determining the bridge's general performance under ambient traffic.

Strain Plots from Ambient Traffic Event

Figures 5.9 and 5.10 present strain plots from a typical ambient traffic event. These plots are shown to illustrate the format of the data obtained for each vehicle crossing over the bridge. The strain plots in Figure 5.9 are shown for all sensors on the six girders for measuring the global bridge behavior (i.e., flexure). Figure 5.10 shows sensor strain data from girders near the pier region that measure localized effects (i.e., connection details). In many of the strain plots, there are apparent gaps of data with strains of 0.0 με (see Figure 5.9e). This phenomenon occurs due to the data processing, in which the temperature strain and live load strain are separated; in this process, the data points between ±1.6 με (i.e., the noise band) are set to 0.0 με to eliminate that noise band and other insignificant strain data. The color coding represents the different sensor locations on the bridge.
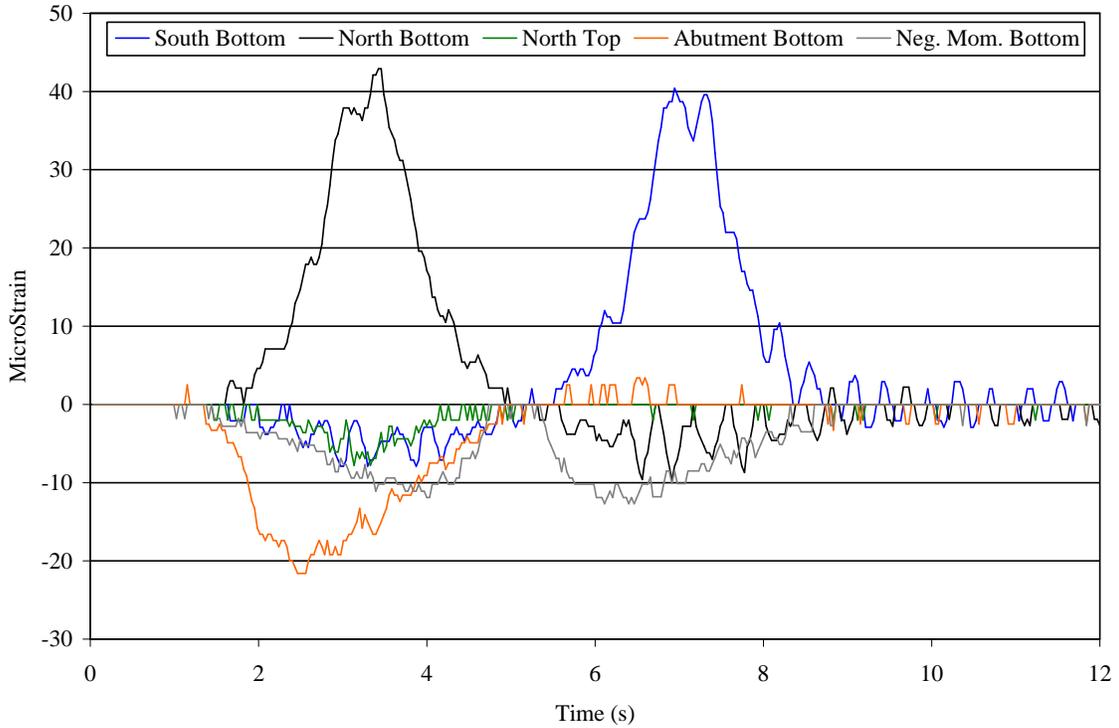
A more detailed discussion of these and other data is presented in the following subsections to describe the bridge's live load performance. Two arbitrarily selected ambient traffic events are referred to in this section: for reference, they will be known as Ambient Traffic Event 1 and Ambient Traffic Event 2. Ambient Traffic Event 1 data are shown in Figures 5.9 and 5.10.
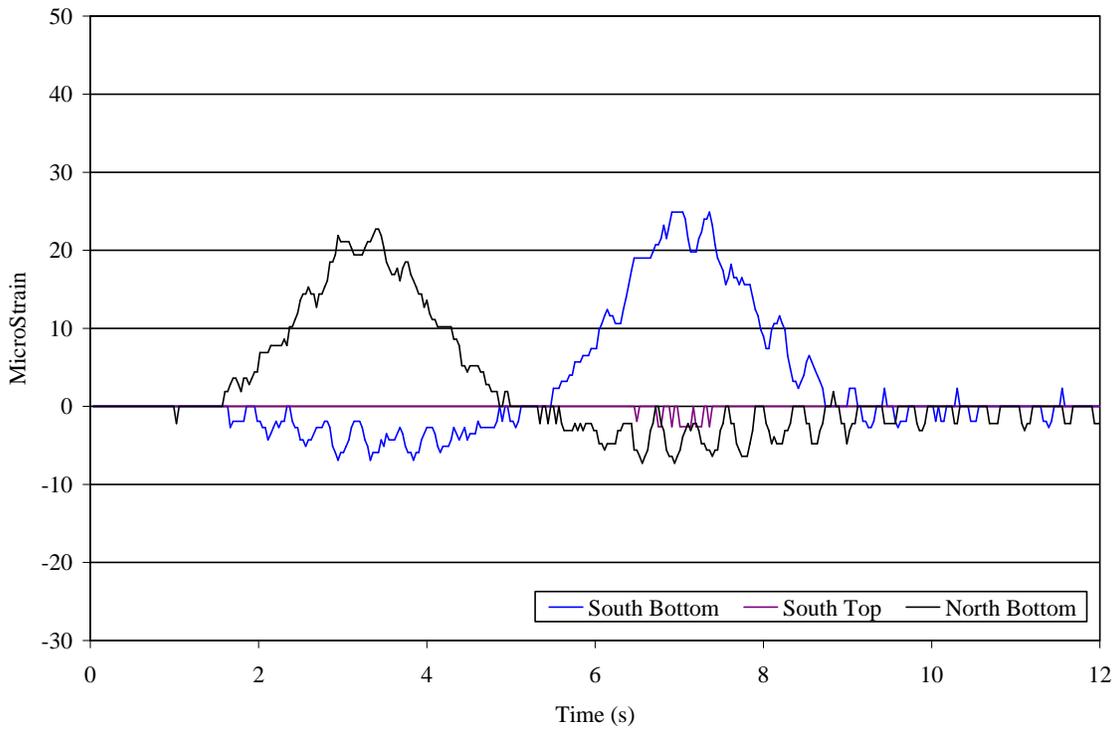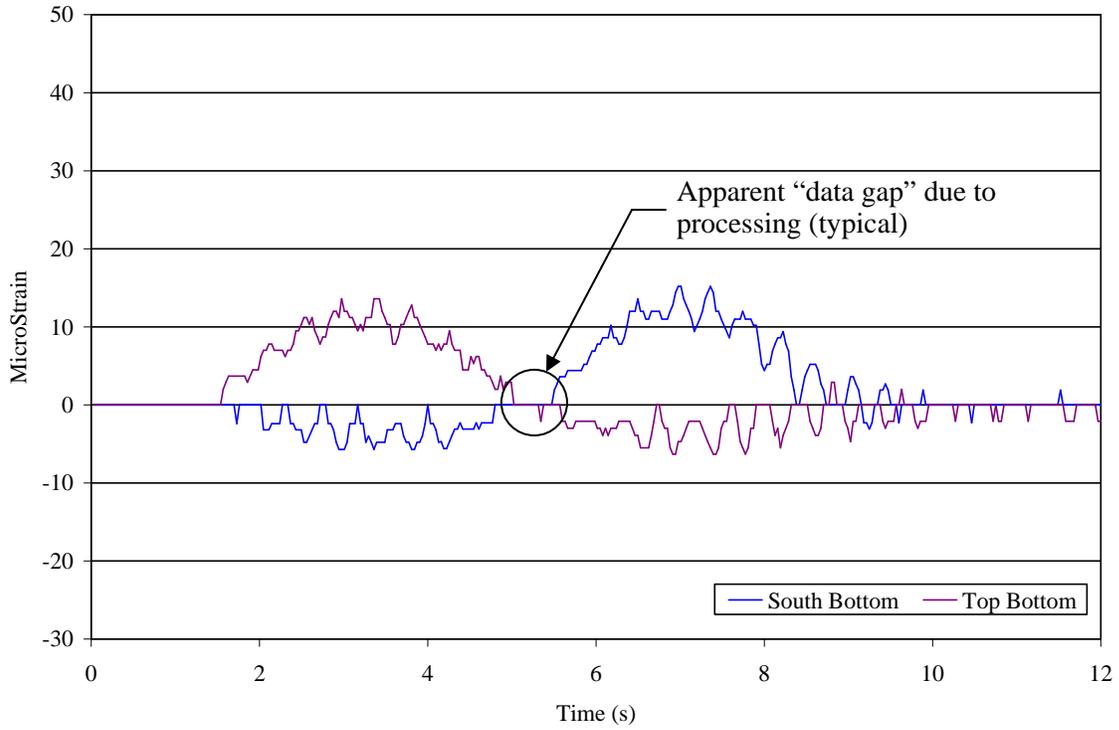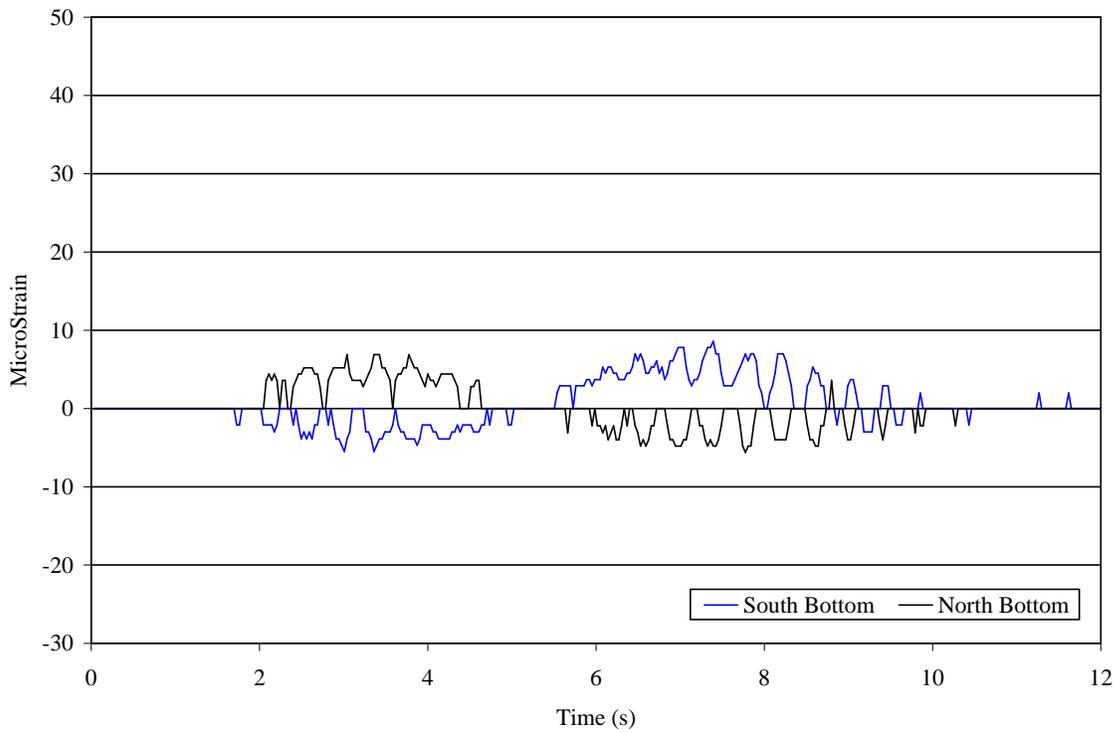
a. Girder 1
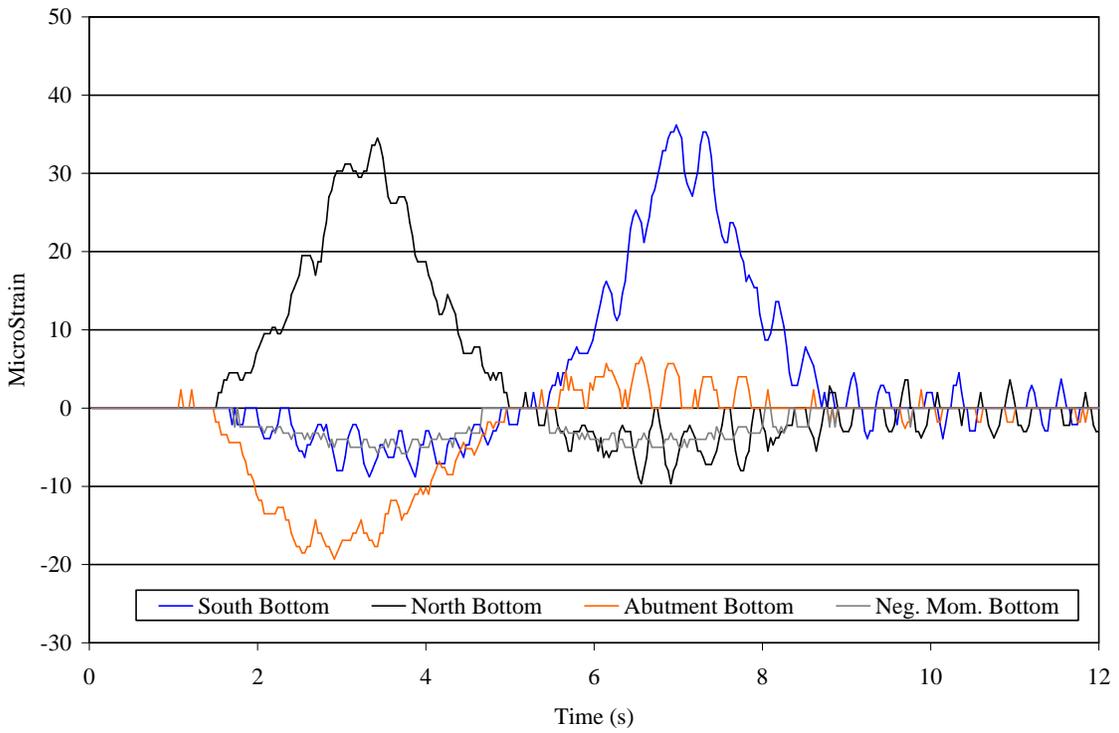
b. Girder 2

c. Girder 3

d. Girder 4

75

Apparent "data gap" due to processing (typical)

South Bottom — Top Bottom
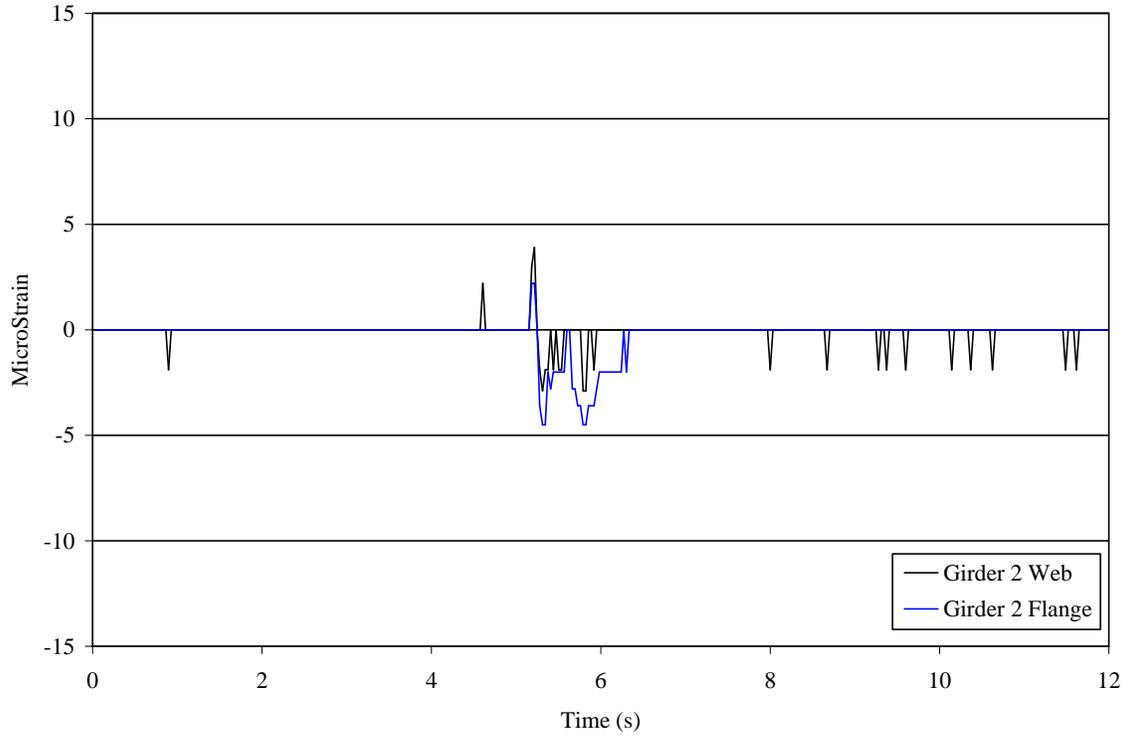
e. Girder 5

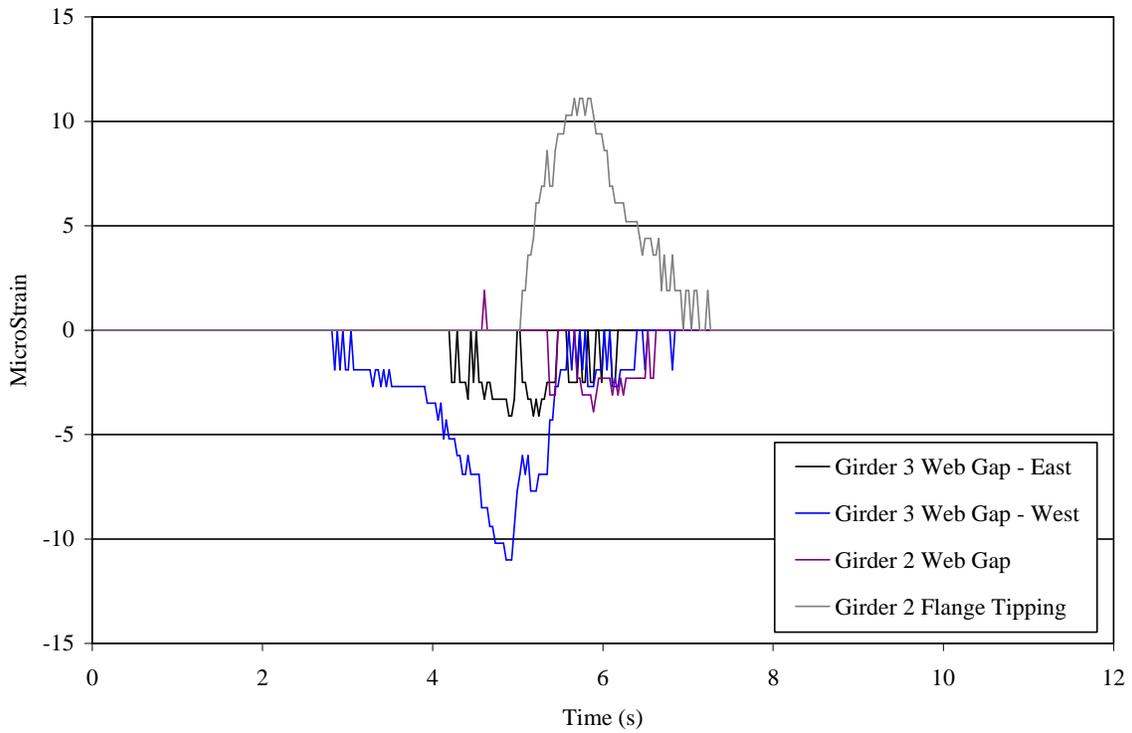South Bottom — North Bottom

f. Girder 6

Figure 5.9. Strain plot from an ambient traffic event

76

a. Welded plate splice in web and flange

b. Web gap region

Figure 5.10. Localized fatigue detail strain data from an ambient traffic event

77

Qualitative Bridge Performance Characteristics

Basic qualitative observations of the bridge performance under live loading are summarized below to verify that the bridge generally responds as expected. The observations are based on fundamental structural principles for a two-span continuous bridge with restrained ends and a vertical support at the pier.

- Bottom flange, midspan. Positive strain is recorded when the loading is on the same span as the sensor, negative strain when the loading is on the span opposite the sensor.
- Bottom flange, abutment. Negative strain is indicated when the loading is on the same span as the sensor, positive strain when the loading is on the span opposite the sensor. Lower strains are recorded when compared to the bottom flange strains at the midspans.
- Bottom flange, negative moment region near the pier. Negative strains are recorded throughout the loading period. The strain goes to 0.0 $\mu\varepsilon$ when the loading nears the pier.
- Top flange, midspan. Negative strain is recorded when the loading is on the same span as the sensor, positive when the loading is on the span opposite the sensor. Lower strains occur than those on the bottom flange strains at the midspans. This is expected, since the neutral axis of the effective girder depth due to the composite concrete deck is near the top flange.
- Localized fatigue details. Low levels of strain are recorded. The largest strain recorded at any of the details is equivalent to a stress of less than 1.3 ksi.

Vehicle Direction

The events recorded by the E. 12th St. Bridge SHM system can be characterized as northbound or southbound vehicle events through two methods. The first is by observing the strain value (compression or tension) from the bottom flange midspan sensors. southbound events are represented by initial positive bottom flange strains at the north midspan. The opposite is true for northbound events, with initial positive bottom flange strain at the south midspan. The second method compares the magnitude of the strain at the bottom flange midspan sensors. If girder 2 and 3 strains are larger than girder 4 and 5 strains, the vehicle can generally be assumed to be traveling southbound, and vice-versa for a northbound event.

Figure 5.11 shows the girder 3 bottom flange strain from Ambient Traffic Event 1. Based on the general observations given above, the vehicle direction associated with this event is southbound. Figure 5.12 shows the same ambient traffic event; in this case, the strain from the bottom flange sensor for each girder at the south midspan is presented. girder 3 has the highest strain magnitude, followed by girders 2, 1, 4, 5, and 6, respectively. This finding supports the observation that Ambient Traffic Event 1 is a southbound event. Figure 5.13 shows the strain for each north midspan bottom flange girder for the same ambient event. Since girder 4 has the highest strain, followed by girders 5, 3, 6, 2, and 1, the ambient event in Figure 5.13 is a northbound event. This is also evident in the initial negative strain from the north midspan bottom flange sensors.

Although the direction and a general transverse position (west or east lanes of the bridge) can be identified for ambient traffic using the strain magnitudes from the bottom flange sensors, this method cannot be accurately used to determine a more precise transverse position of a vehicle on the bridge. This is due to the unknown properties of the vehicles (i.e., relative weight of each wheel line, the dynamic properties of the vehicle, and the vehicle geometry).
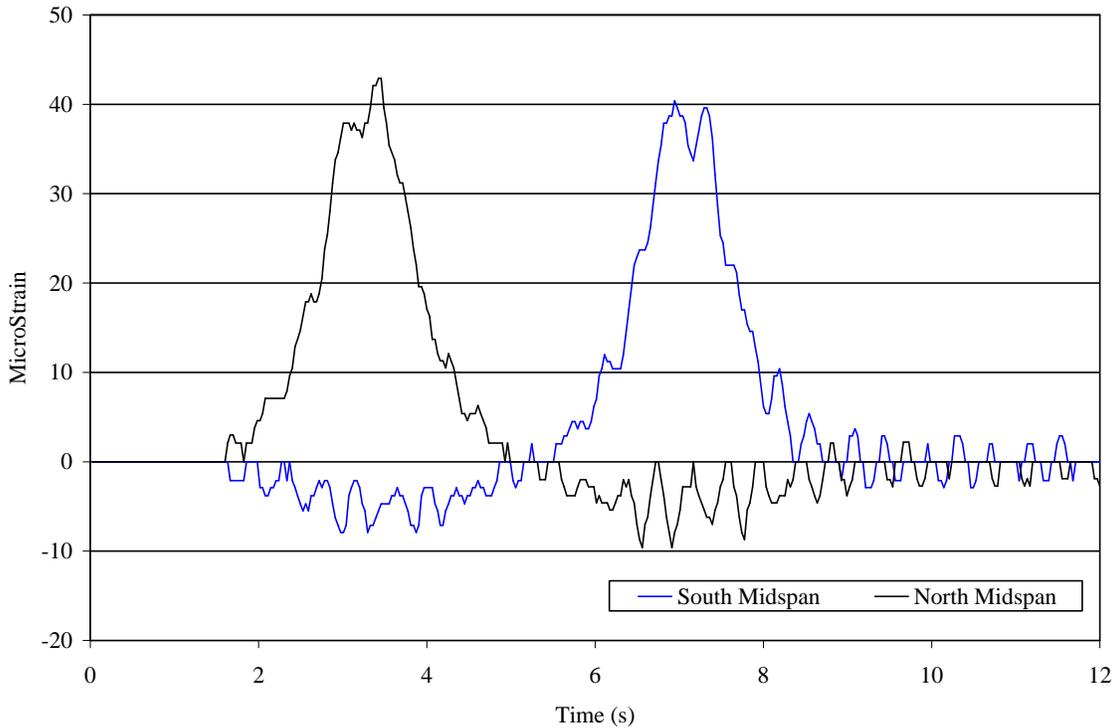

Figure 5.11. Strain plots of girder 3 bottom flange sensors (north and south midspan) from southbound Ambient Traffic Event 1
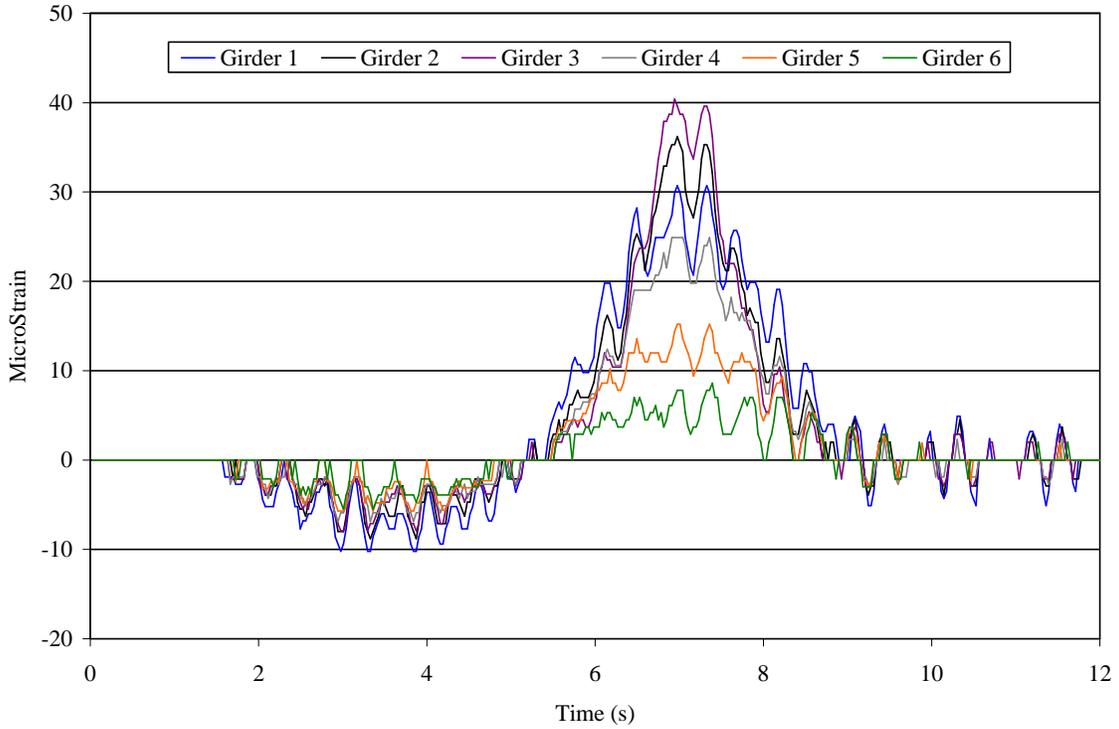
Figure 5.12. Strain plots of south midspan bottom flange sensors from southbound Ambient Traffic Event 1
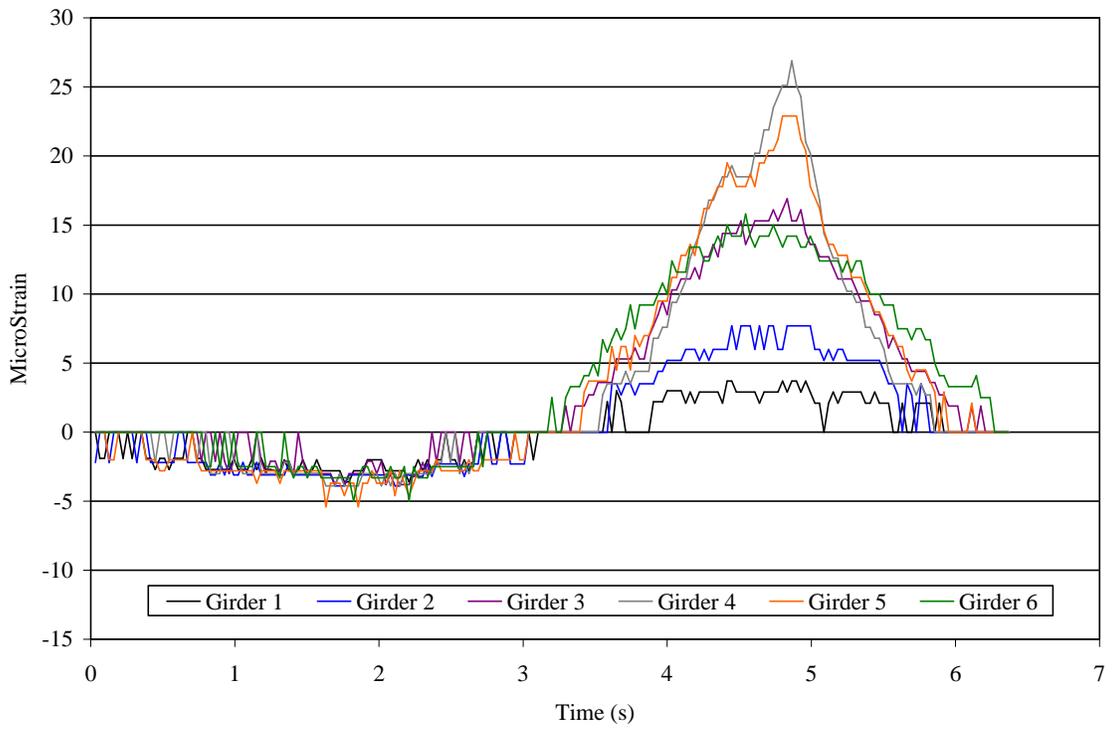
Figure 5.13. Strain plots of north midspan bottom flange sensors from northbound Ambient Traffic Event 2

80

Dynamic Response

The oscillations seen in Figure 5.14 represent the dynamic response of the bridge. Dynamic patterns are noticeable in the ambient traffic data, but the sample rate (31.25 Hz) is not sufficient to characterize the dynamic response fully. Furthermore, evaluation of the dynamic behavior of the structure was beyond the scope of this study.
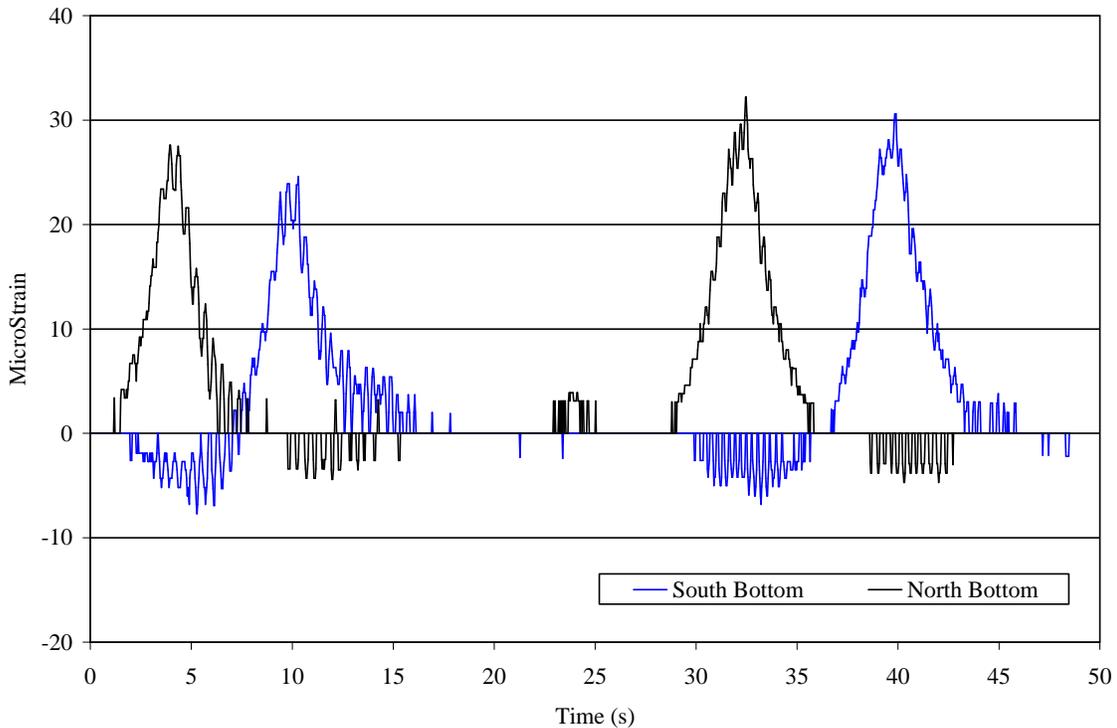
Figure 5.14. Strain plot of girder 2 bottom flange sensors from northbound Ambient Traffic Event 3

Bridge Response due to Controlled Load Tests

The strain data from the controlled load tests provide additional information that cannot be obtained from the ambient traffic data because the position of the truck and the truck geometry and weight are known. As discussed above, the load tests were performed by driving the load truck from north to south.

Strain Plots from Controlled Load Test

Strain plots from run 2 of the controlled load test are presented in Figure 5.15 (global performance sensors) and Figure 5.16 (fatigue detail sensors). During run 2, the test truck drove near the west barrier rail (see Figure 5.2 for test truck position), therefore creating a loading

condition similar to the ambient traffic condition resulting in the response shown in Figures 5.9 and 5.10.
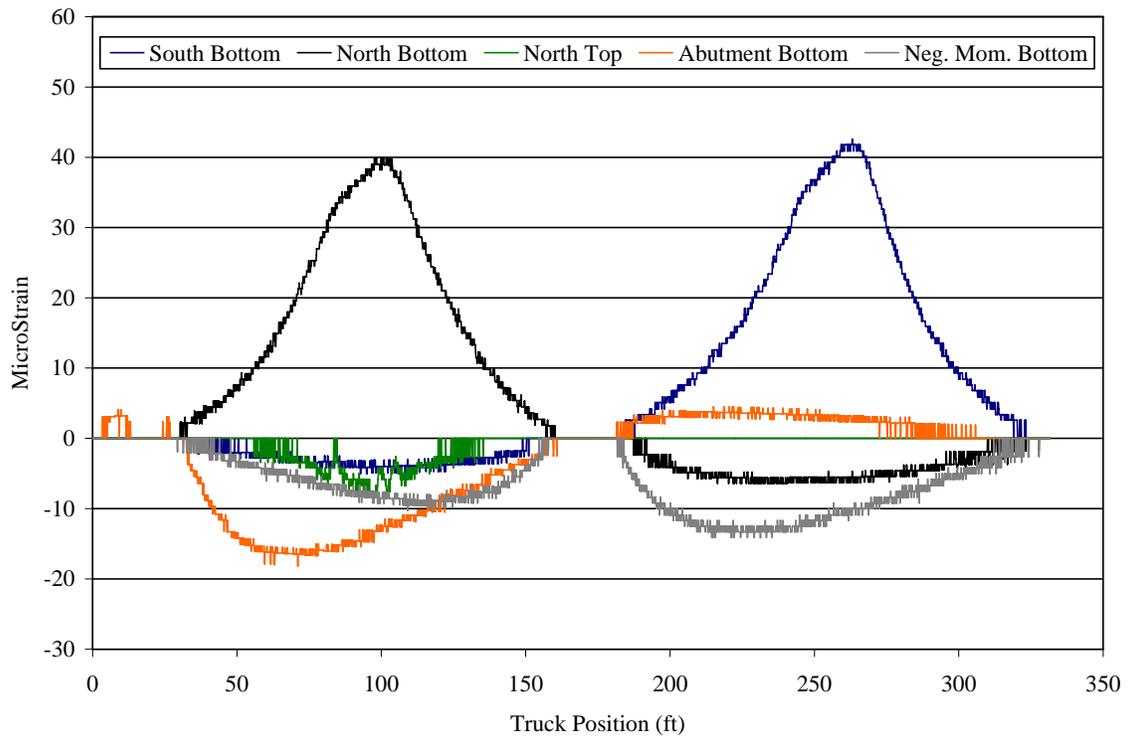
The bridge's live load performance is presented in the following subsection using data from runs 2, 4, and 6. Not all of the data from the load tests are presented, but the data shown are representative of all of the data collected.
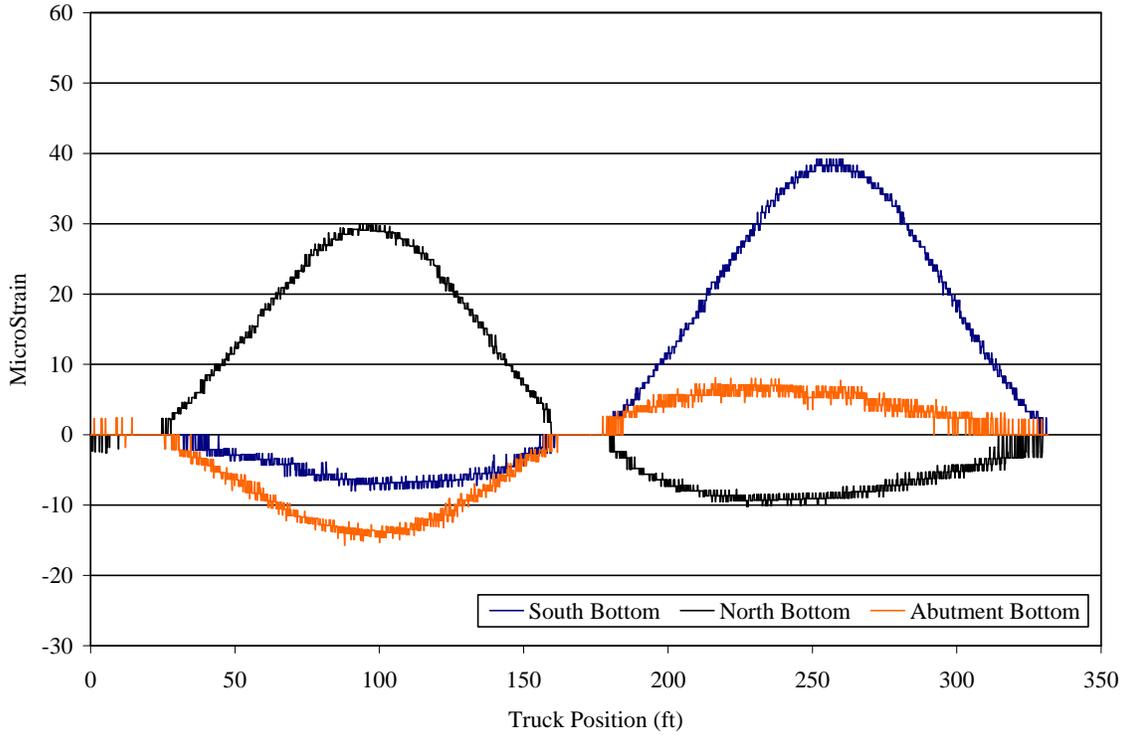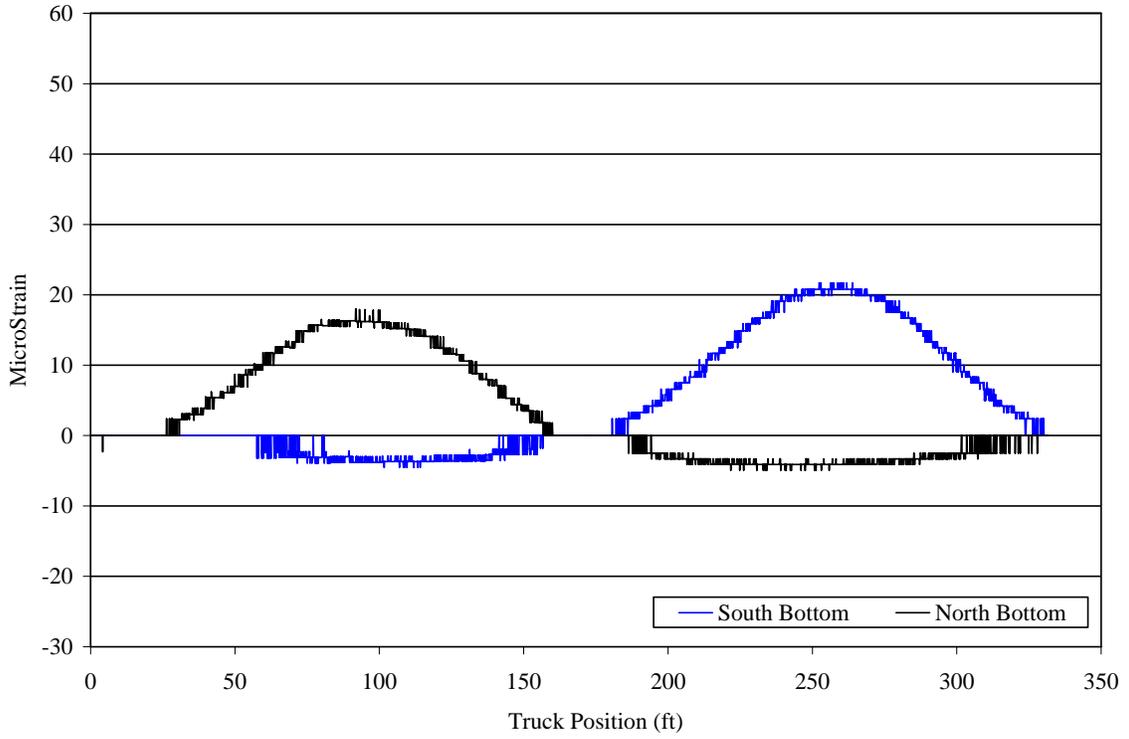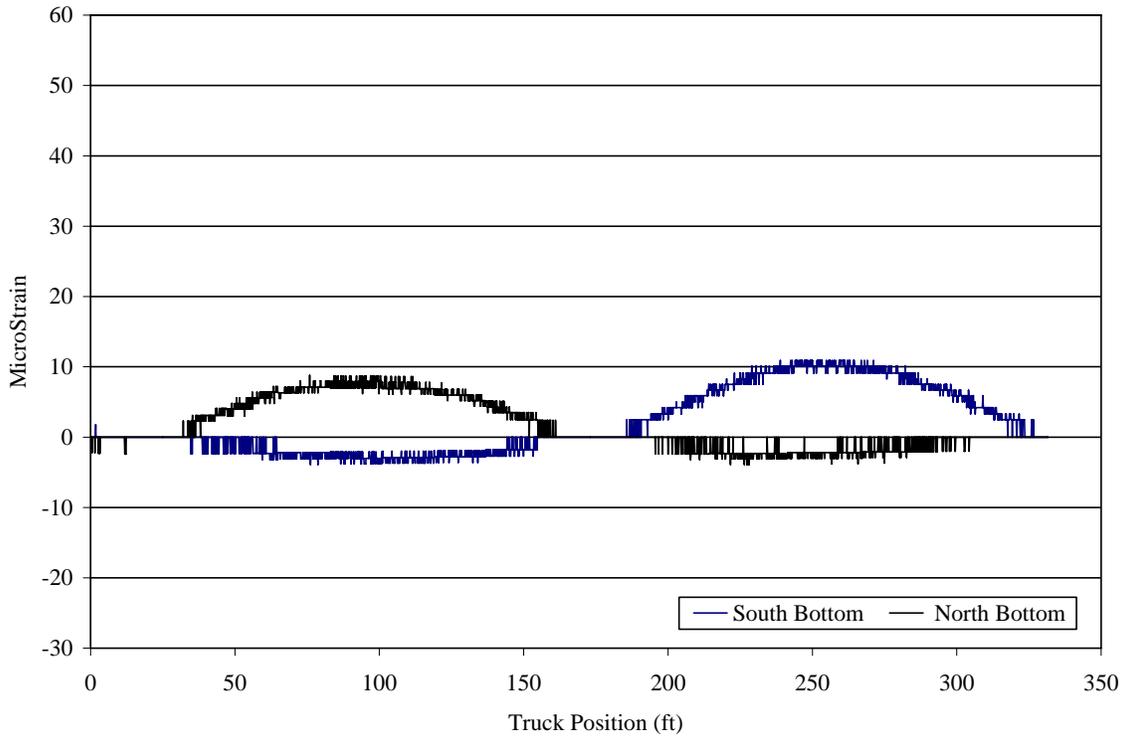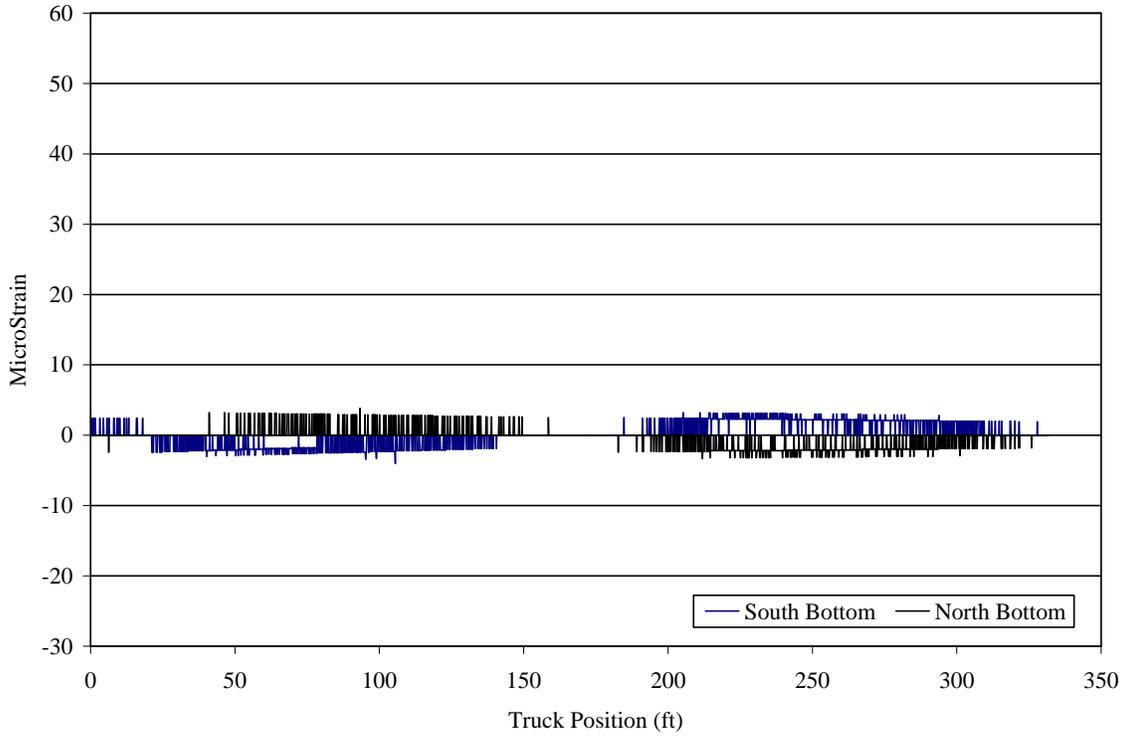

a. Girder 1
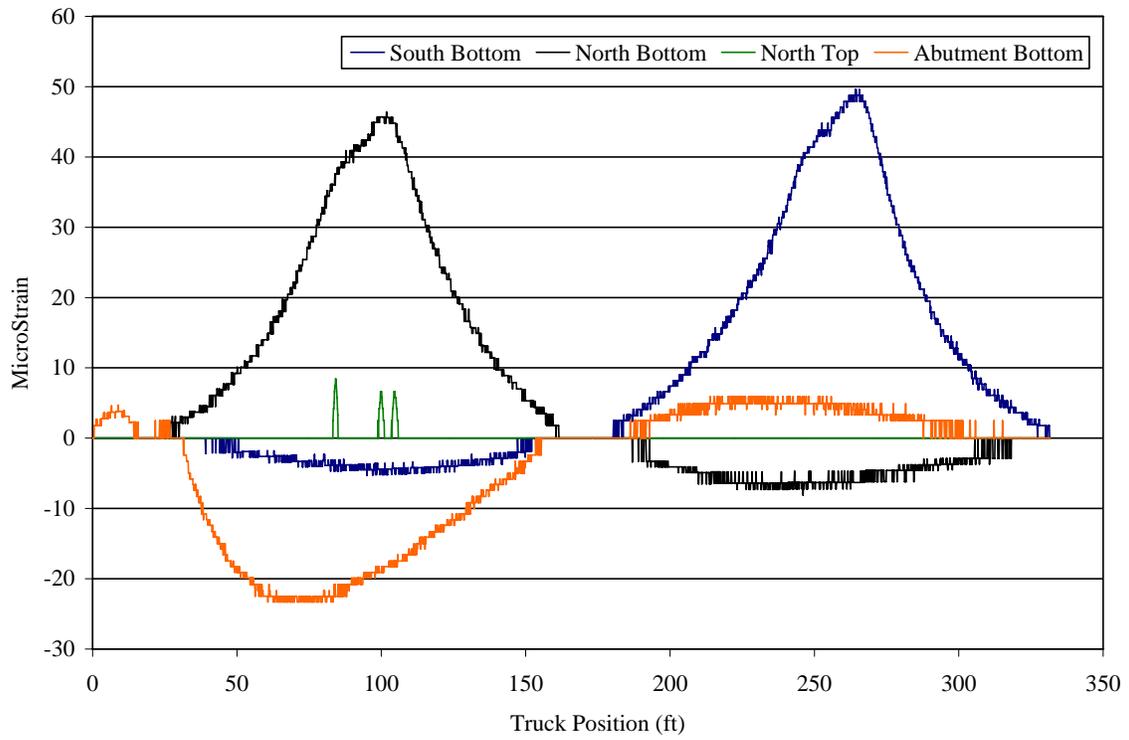
b. Girder 2

c. Girder 3

83

d. Girder 4

e. Girder 5

84

f. Girder 6

Figure 5.15. Strain plot from run 2 of the controlled load test
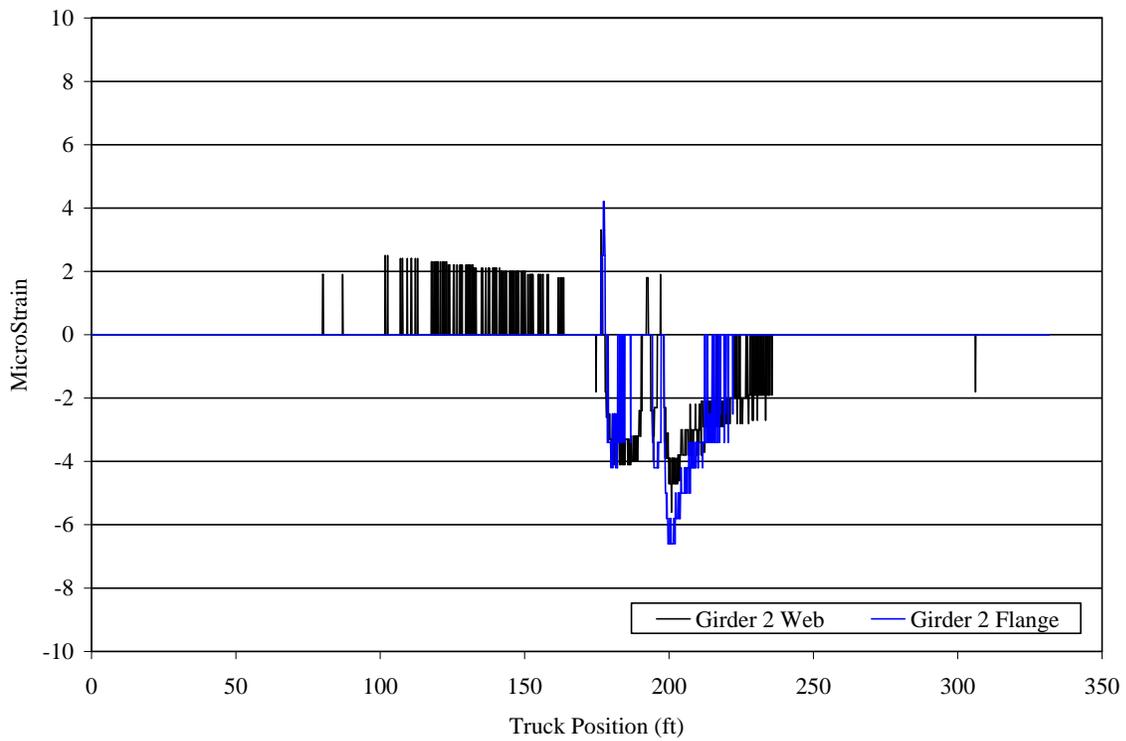
a. Welded plate splice in web and flange
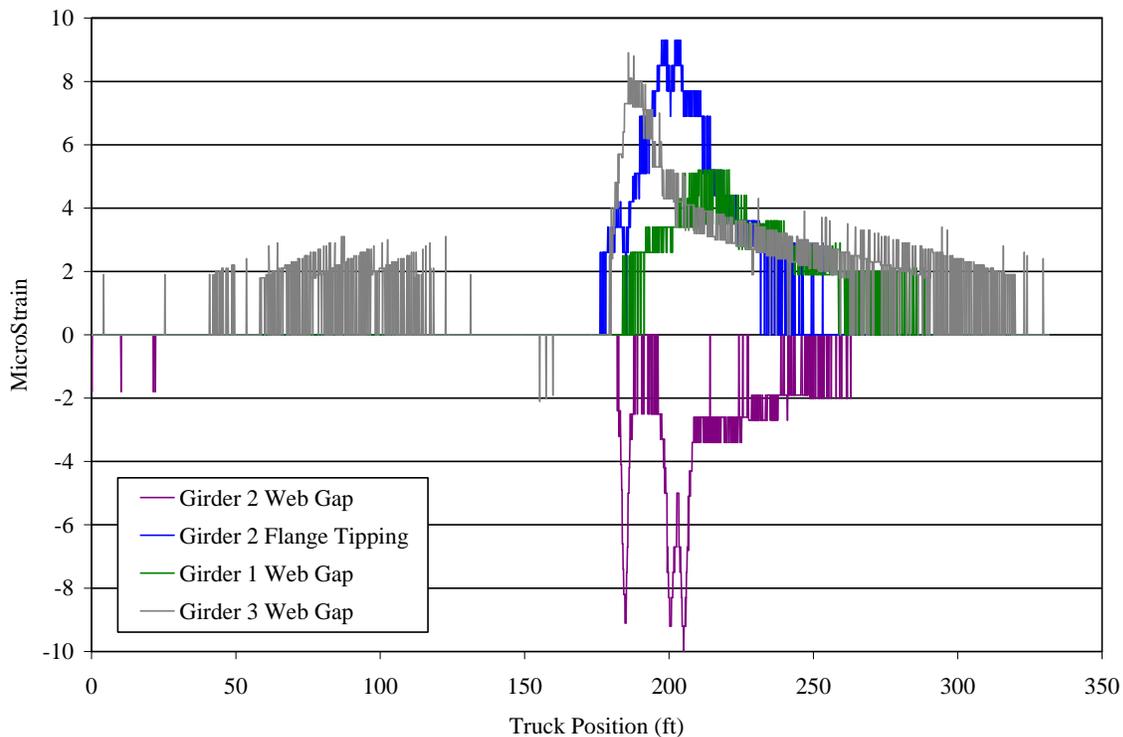
b. Web gap region

Figure 5.16. Strain plots of localized fatigue details from run 2 of the controlled load test

Comparison between north Midspan and south Midspan Strain

When the strain from the north and south midspan bottom flange sensors on each girder are compared in Figure 5.15, it is noted that the south midspan strains are larger than the north midspan strains, especially for girder 1. Primary reasons for this may include the differing inertia values between the north and south spans and the differing live load positive moments generated in each span due to the load truck geometry with respect to the fixed ends and roller support as the truck crosses the bridge in one direction. Other possible issues that may contribute to this situation include the following:

- Slightly different span lengths (north is 145.37 ft. and south is 153.24 ft.)
- Differing as-built conditions of the concrete barrier and deck across the bridge transversely and longitudinally, thereby creating different stiffness values between each girder and the north and south spans.
- Boundary conditions at each end of each girder, causing different stiffnesses in the girders

Localized Fatigue Detail Response

Figure 5.16 shows the response from the localized details during run 2 of the controlled load test. The strain magnitudes measured at the instrumented fatigue-sensitive details are relatively low.

Figure 5.17 compares welded plate splice strain data from Ambient Traffic Event 1 and run 2. (Note that the time in which the two events occur is different: run 2 was conducted at crawl speed.) The strain profile is the same for both: a positive spike is followed by multiple negative spikes. This demonstrates that the behavior of the weld as the vehicle approaches the area is a positive spike, followed by negative spikes as the vehicle crosses over the area. Similarly, Figure 5.18 compares the web gap region strain data from Ambient Traffic Event 1 and run 2. (Again, note that run 2 was conducted at crawl speed.) The profiles are similar, with positive flange tipping strains and negative web gap strains. The positive flange tipping strains may be caused by the weld between the flange and the vertical stiffener being placed under tensile strains as the cross-frames act to pull stiffener away from the flange. The negative strain in web gap region may be from the compressive axial forces placed on the region as the vehicle crosses the instrumentation location. Three spikes can be seen that are most likely due to the axles as they cross the region. The magnitudes are different. However, this is not surprising because the size of the ambient traffic event is unknown and this region would be affected by the exact transverse vehicle position, which cannot be verified for the ambient traffic event. It is important to note that the strains in these details are very small, and the behavior in these regions is caused by very localized effects of the vehicle on the region. Therefore, the above explanations of the behavior are only basic observations and engineering judgments.
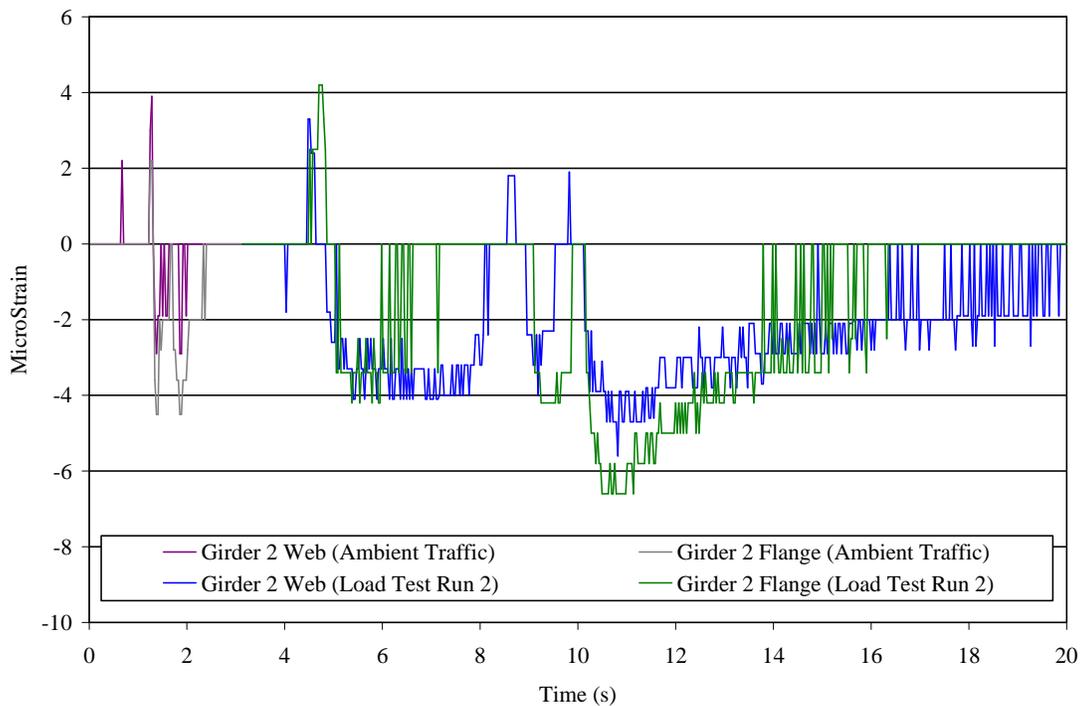

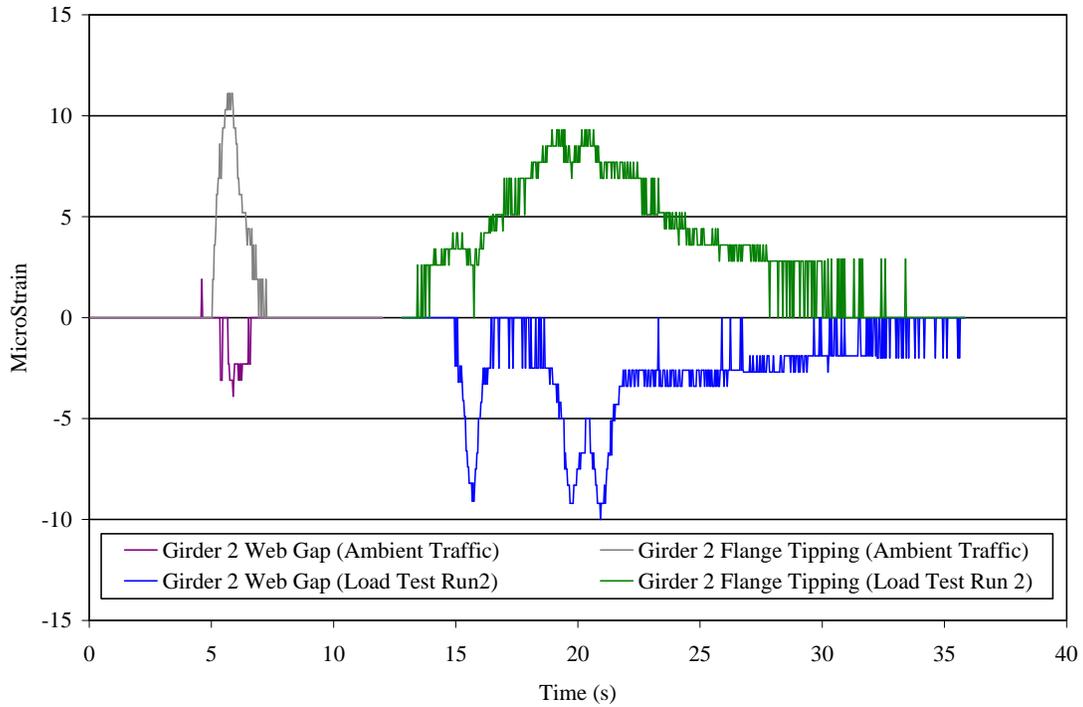**Figure 5.17. Girder 2 welded plate splice comparison for Ambient Traffic Event 1 and run 2**

Figure 5.18. Girder 2 web gap comparison for Ambient Traffic Event 1 and run 2

Localized Top Flange Strain

The top and bottom flange responses at the north midspan for run 2 are shown in Figure 5.19. Three positive strain spikes occur in the top flange as the truck crosses the top flange sensor location. These spikes represent localized strain effects on the top flange caused by the truck tires driving directly across the girder 2 instrument location.
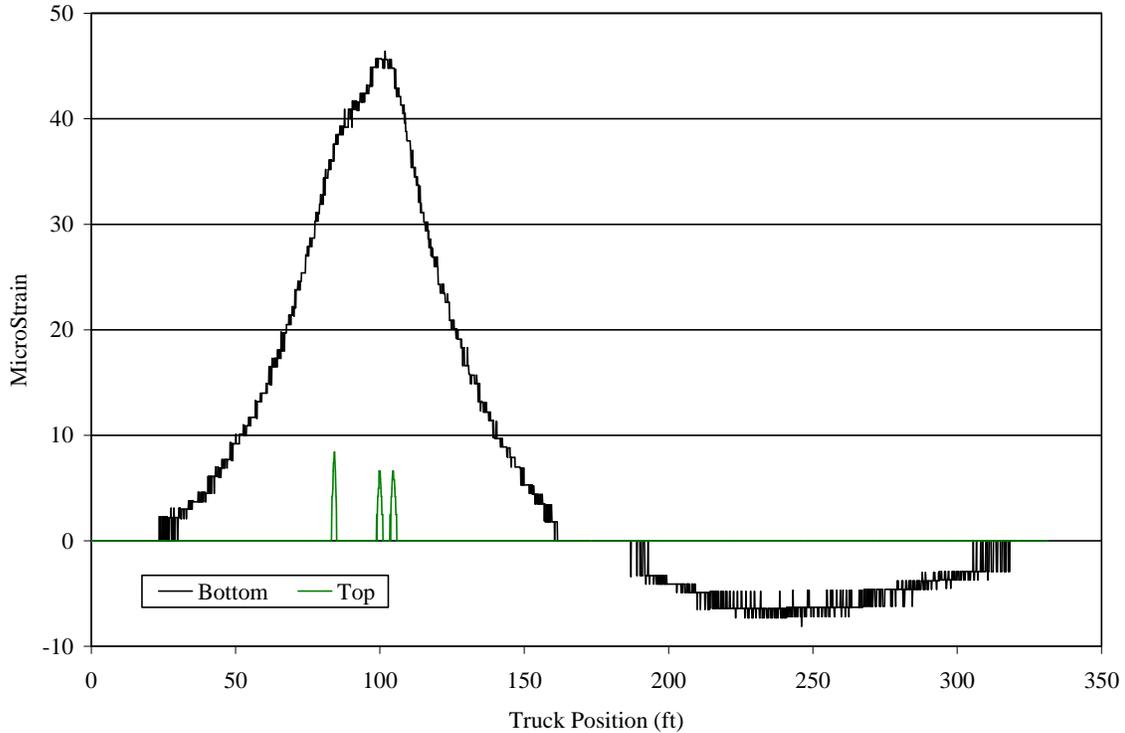
Figure 5.19. Strain plots of girder 2 top and bottom flange sensors at the north midspan, run 2 of the controlled load test

Symmetry of Bridge Response

The bridge is symmetrical about its longitudinal centerline, as shown in the Bridge Description section above (3.1). The symmetry of the bridge response from a symmetrical test truck position (run 4) can be seen in Figure 5.20, which shows the north midspan bottom flange strain. This symmetry is shown through the similar strain histories for girders 1 and 6, girders 2 and 5, and girders 3 and 4, which are transversely symmetrical. The bridge's symmetry can also be seen in Figure 5.21, which shows bottom midspan strain for girders 2 and 5 during runs 2 and 6, respectively. In this case, the strain histories, which are similar for both girders, are from girders that have a wheel line almost directly above them in the respective controlled load test runs.
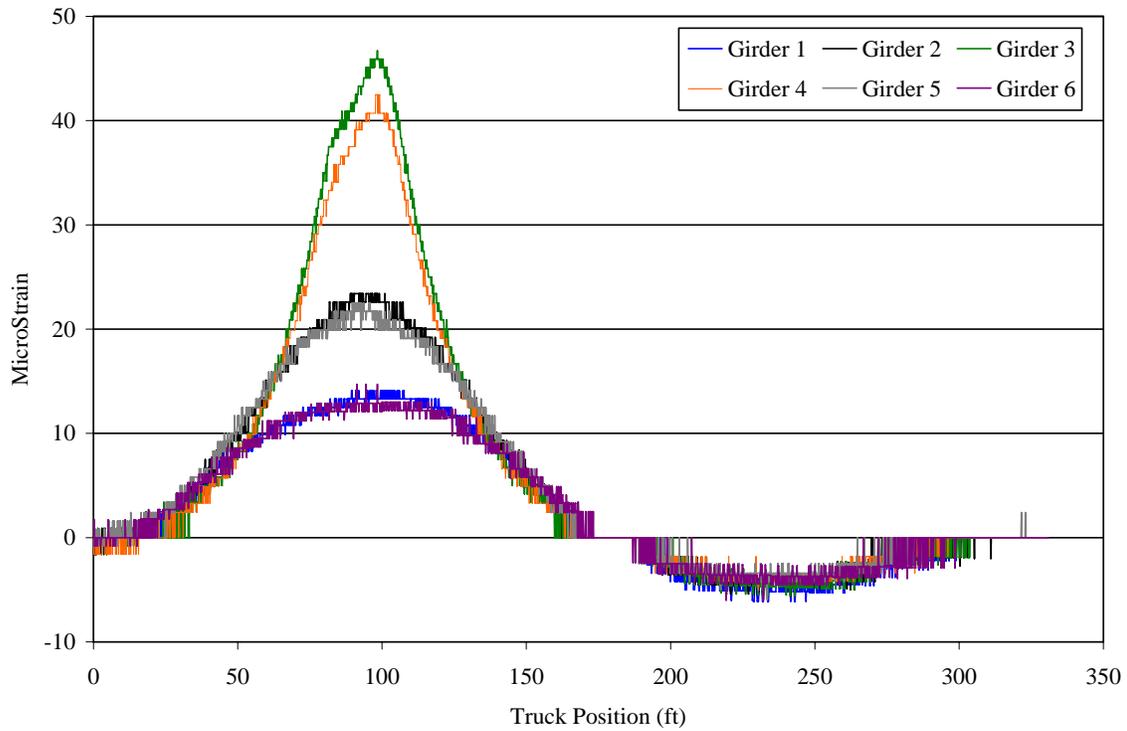
Figure 5.20. Strain plots of north midspan bottom flange sensors from run 4 of the controlled load test
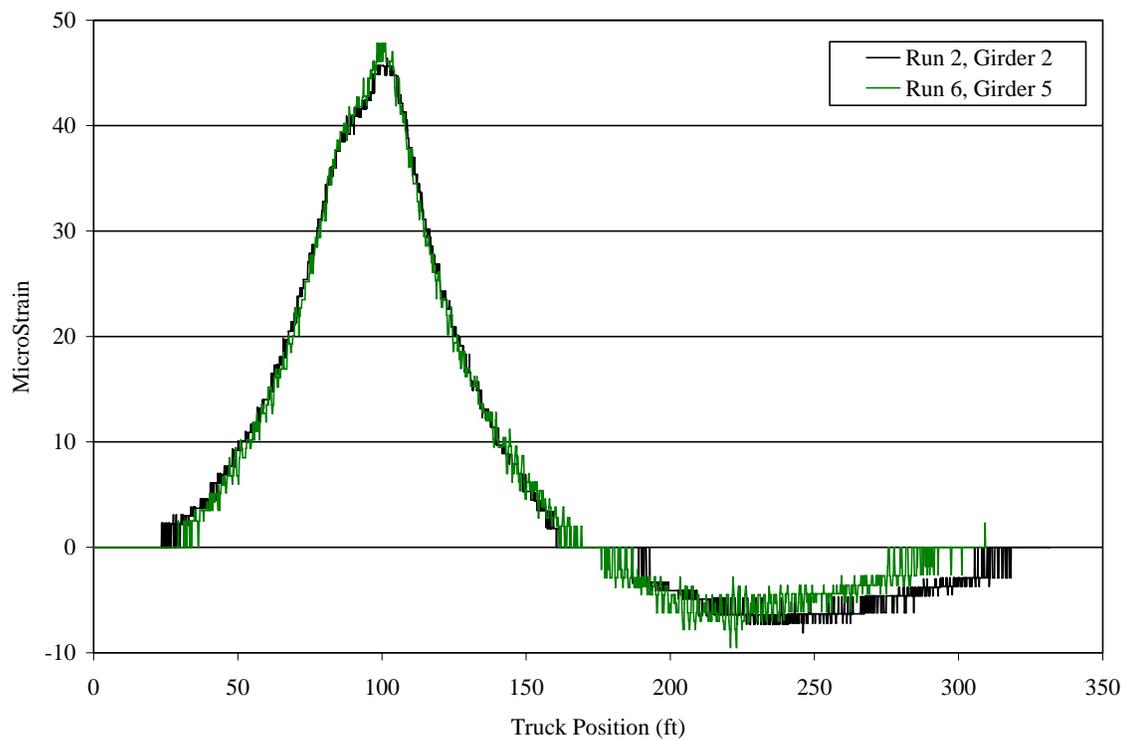

Figure 5.21. Strain plots of north midspan bottom flange sensors

Bridge Performance Indices

As stated above, the FBG strain data are processed with the DPP program, which calculates several bridge performance indices. The indices include the DF, NA, and ER ratio, which can potentially be used to evaluate the performance of the bridge during the controlled load test, as well as the bridge's performance over time.

Distribution Factor

The amount of load distributed to each girder (as a percentage or fraction of the total strain on the bridge cross section) is presented below. This distribution is calculated from data at the north and south midspans using the recorded bottom flange strains. In what follows, the DF at each midspan will be referred to as either north or south.

DF from controlled load tests. The DF for each girder for runs 2, 4, and 6 are presented below. Since the sum of the bottom flange strain at the particular cross-section must be greater than the threshold set by the user (45 me in this case), the DFs at the north midspan were computed only while the load truck was in the middle of the north span, and the DFs at the south midspan were computed only while the load truck was in the middle of the south span.
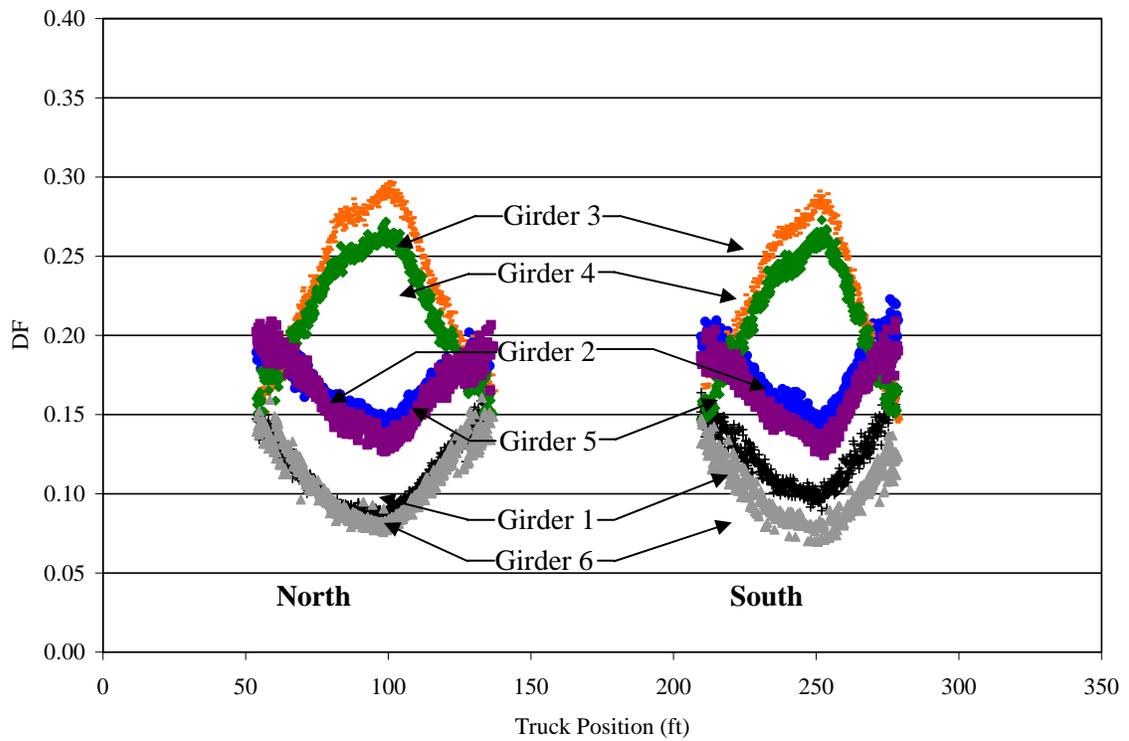
Figure 5.22a shows the DFs for run 2 of the controlled load test. The magnitudes of the DFs for girders 2 and 3, the two most heavily loaded girders, increase as the truck nears the middle of each span and decrease as the truck passes midspan. The DFs for the other girders generally have magnitudes proportional to the distance of the truck from the girder. When comparing the north and south midspan DF data, several things can be observed. Girders 2 and 3 (the most heavily loaded girders) have a larger DF at north midspan than at the south. Girders 1, 4, 5, and 6 have a lower DF at the north midspan than at the south. This indicates the south midspan is distributing load better than the north. The maximum DF for any girder was approximately 0.34, for girder 2.

The DFs for run 4 of the load test are shown in Figure 5.22b. The shapes of the individual DF plots for each girder are similar to those of run 2, where the more heavily loaded girders (i.e., girders 3 and 4) have concave down shapes, while the other girders have concave up shapes. Once again, the symmetrical behavior of the bridge is demonstrated when girders that are transversely symmetric exhibit similar DF profiles. The same behavior discussed for run 2 can be seen in run 4, in which the south midspan distributes the load slightly better than the north (the difference is not as significant in run 4 as in run 2). The maximum DF is less than 0.30.

The DF values for run 6, shown in Figure 5.22c, have similar shapes and magnitudes to the corresponding transversely symmetrical girders associated with the DF values from run 2. However, unlike the run 2 data, much better agreement is evident in the north and south DF for the more heavily loaded girders. Girder 5 has the largest DF (0.31), which is slightly less than the DF for girder 2 for run 2 (0.34).
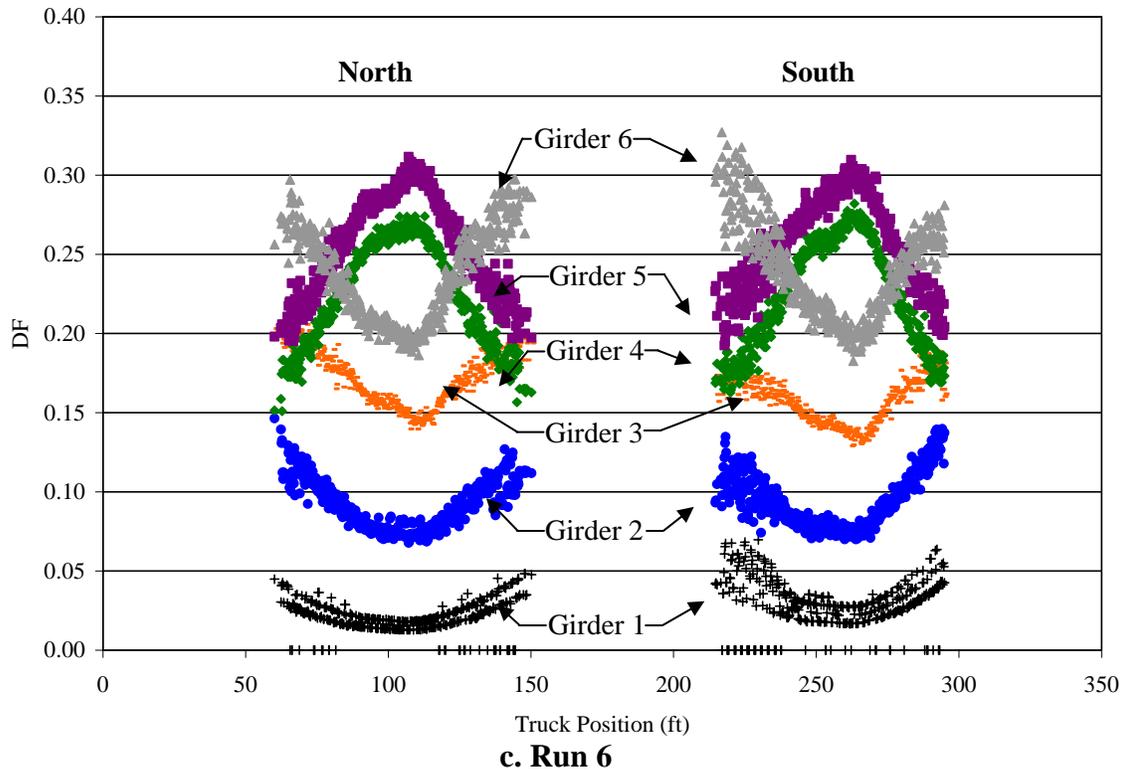
a. Run 2

b. Run 4

c. Run 6
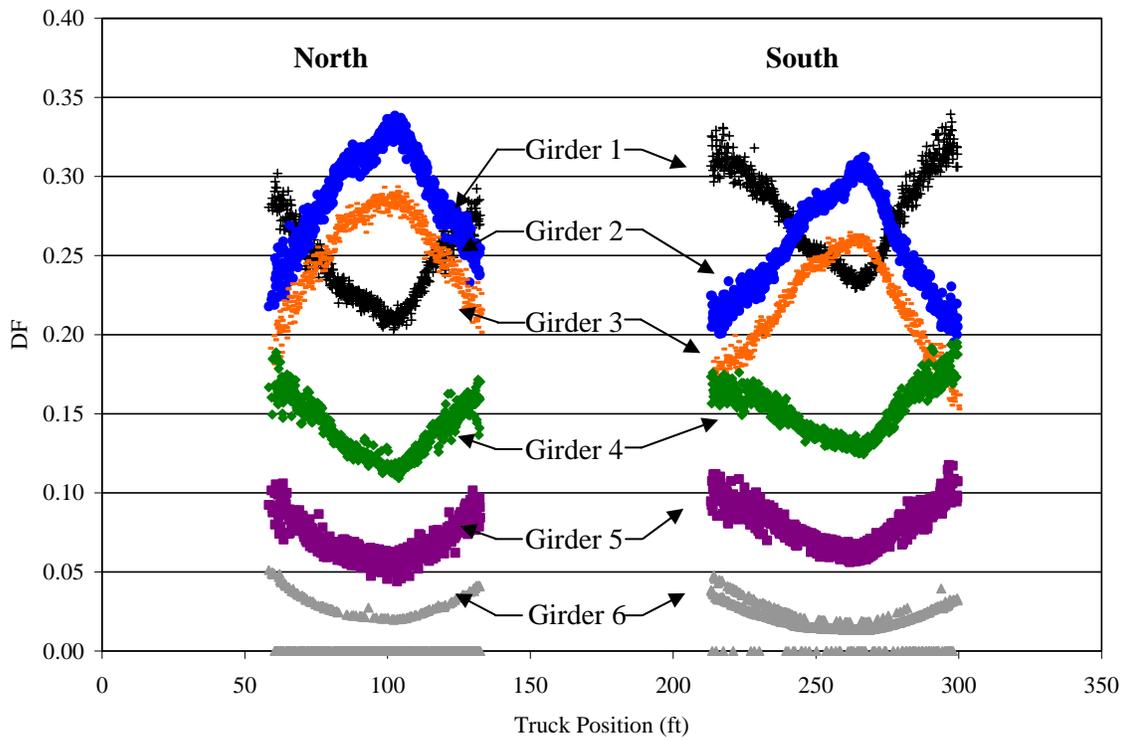
Figure 5.22. DF at north and south midspan for the controlled load test

The general profiles of the data in Figure 5.22 show that the DFs for the most heavily loaded girders increase as the vehicle approaches the midpoint of each span and then decrease as the vehicle moves past the midpoint of the span. Conversely, the DF for the lesser loaded girders decrease as the vehicle approaches the midpoint of each span and then increase as the vehicle moves past the midpoint of the span. This behavior is validated by considering St. Venant's Principle, the longitudinal and transverse flexibility of the bridge, and the change in load paths through the bridge resulting from dynamic loads.

In Figure 5.22, the heavier loaded girders show that the DF for the north midspan is slightly higher than that of the south midspan. These differences could be due to the stiffness differences between the girders in the north and south spans.

DF time history from ambient traffic. The information below presents the DF for each girder over time using ambient traffic data that exceed the DF threshold discussed above. Each data point represents the average daily DF for the particular girder for one day. The graphs are presented with a linear best fit trend line for the north and the south midspans. Since some north span sensors have periodically performed unreliably since October 2004, those data were not included in this analysis. The DF data for all of the girders presented below have outliers much higher and lower than the rest of the data set. This can be attributed to days with low volumes of traffic, in which one event can skew the results. On one Sunday, for example, only one event was large enough for the DF to be calculated; therefore, the data would be skewed for that day.

93

Figure 5.23 shows the DF for all six girders for the north and south midspans. The south DF for girders 2, 4, 5, and 6 is nearly equal to or lower than the north DF. For girder 1 the south DF is slightly higher that the north DF. This finding agrees with the strain data shown in Fig 5.15 and the DF load test data shown in Fig 5.22. The north DF is higher than the south DF for girder 3; this agrees with the findings of the controlled load test. With the exception of the north span of girder 3, the trend lines are slightly decreasing or nearly constant for each girder. Near day 30, the north girder 3 DF begins to rise. A possible reason for this is a change in traffic patterns (i.e., seasonal traffic change, change in the number of vehicles traveling in each direction, the size of the vehicles in each direction, etc.).

The DF trend lines for north span may not accurately represent the data shown. Because of the limited size of the data set, the outliers adversely affect the slope of the trend line. In contrast, the trend line for south span is more statistically significant and representative.

The root mean square (RMS) for each DF has more statistical significance and minimizes data outliers. Table 5.3 and Figure 5.24 show the long-term and load test DF RMS values for each girder for both the north and south spans. The difference in the long-term and load test DF RMS values can be expected, since the load test DF is based on a specific vehicle configuration (the load truck) while the long-term DF results from ambient traffic from which neither the vehicle configuration, location, nor direction can be determined. The difference between the north and south span RMS values for the long-term and the load test DFs can be attributed to differences in the stiffnesses of the girders with respect to the different spans, which affects the load path for each span.
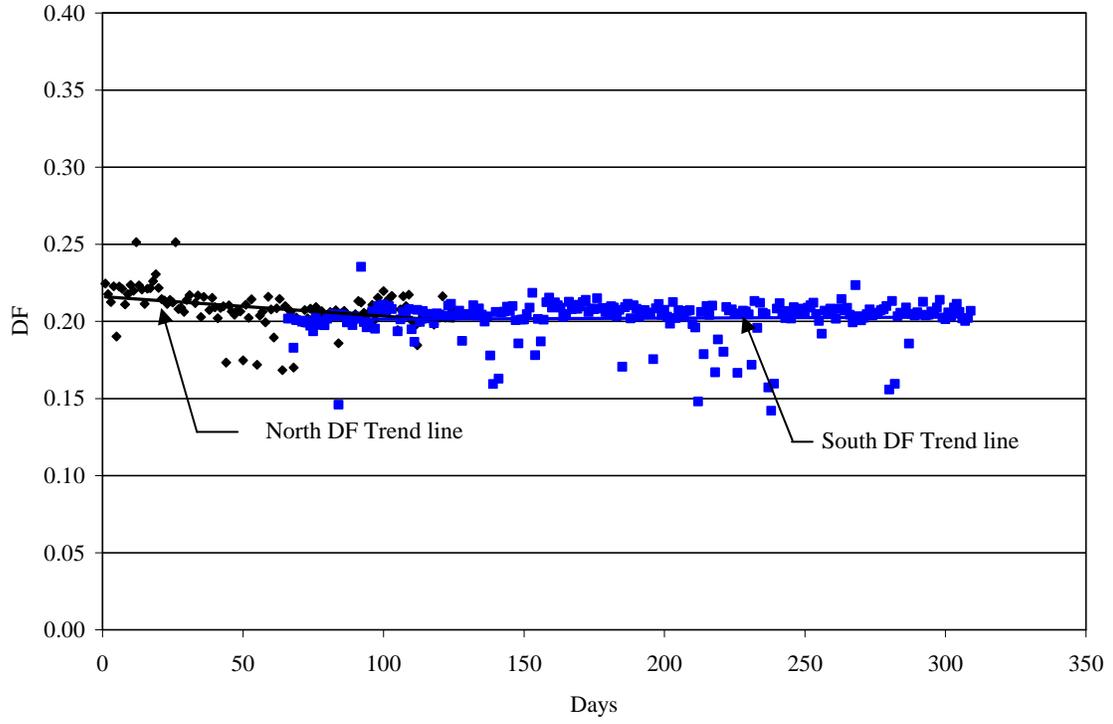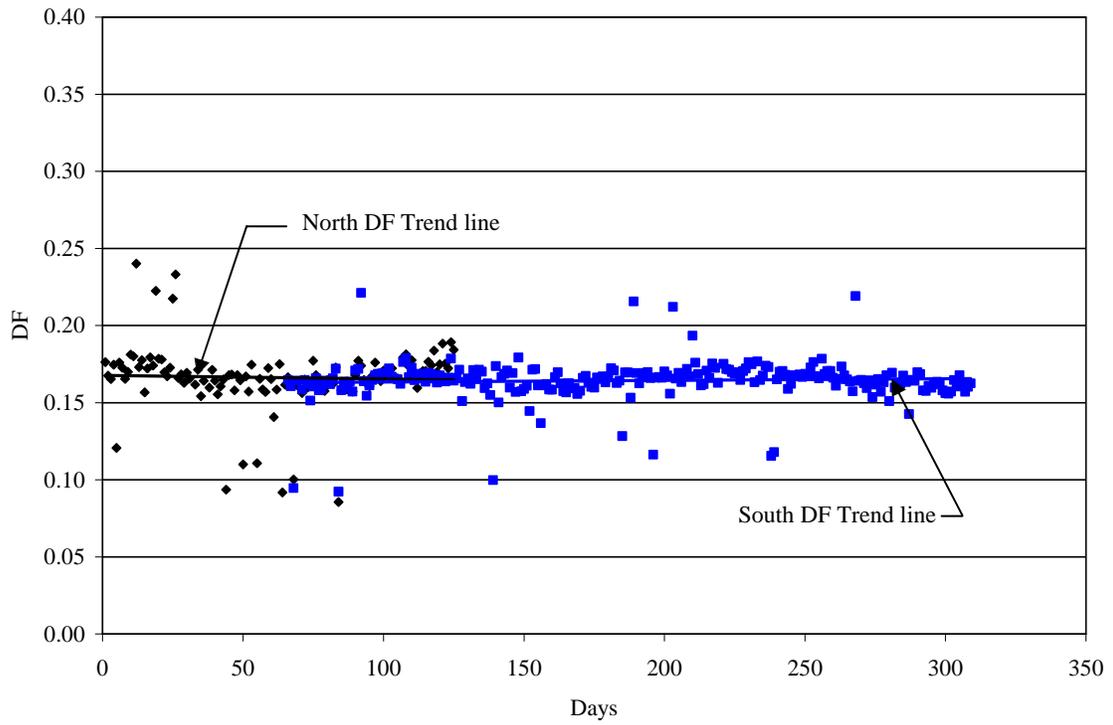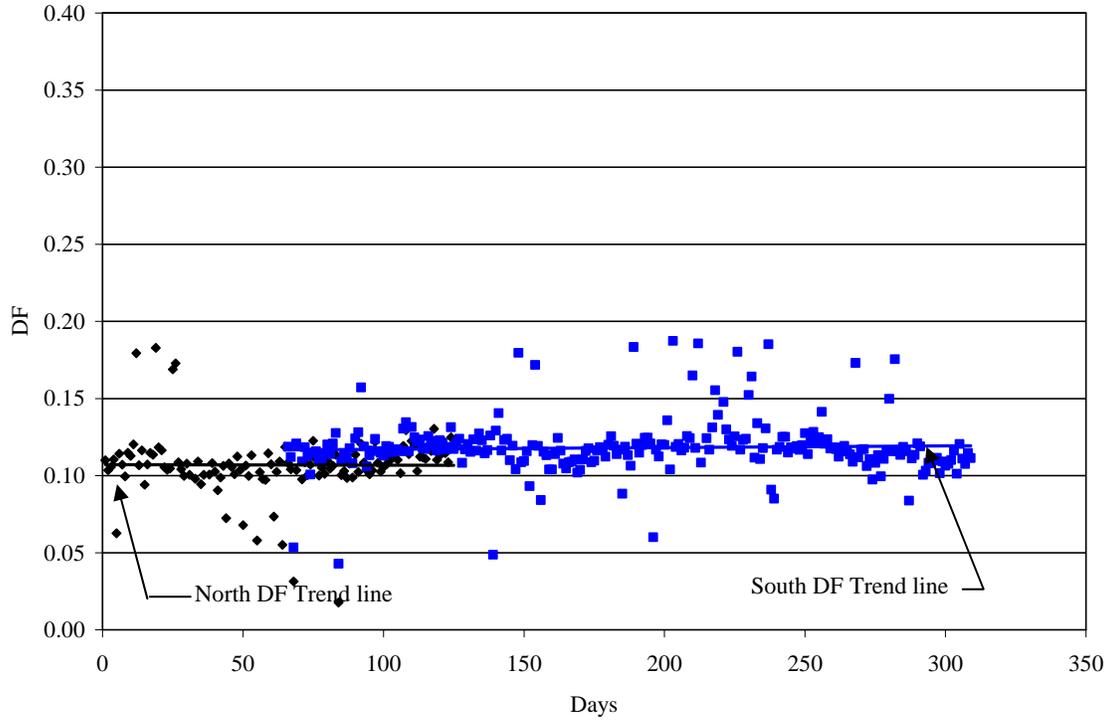

a. Girder 1

94

b. Girder 2

c. Girder 3

95
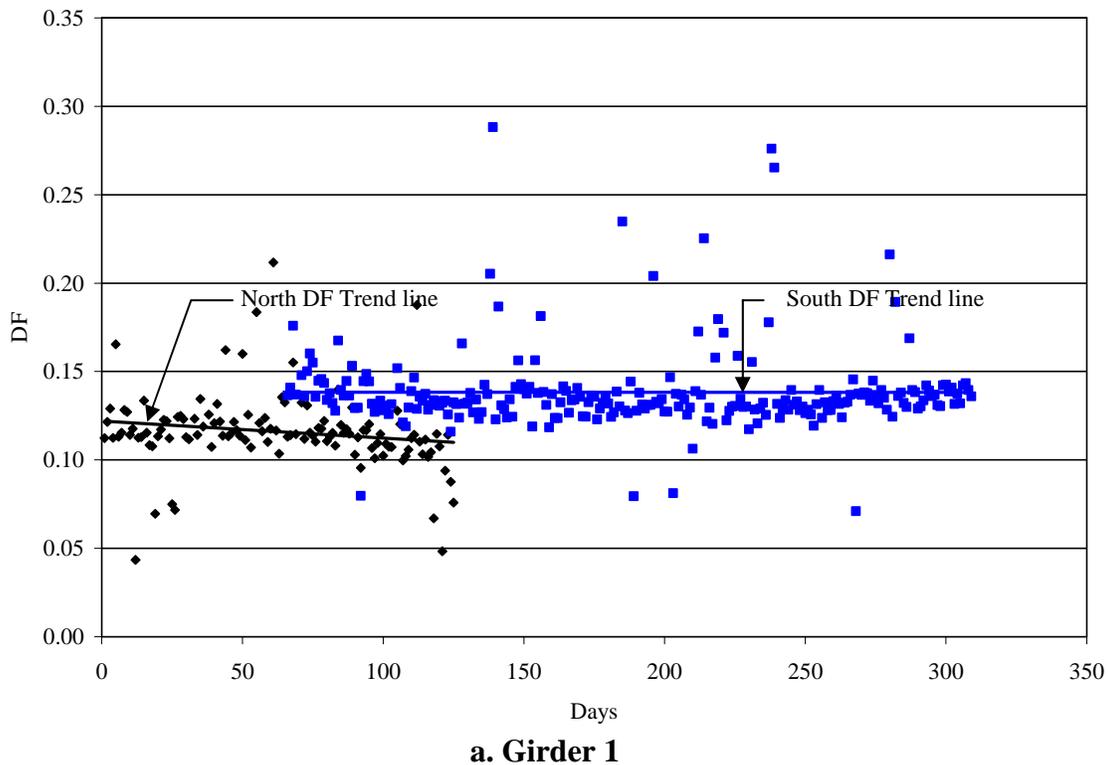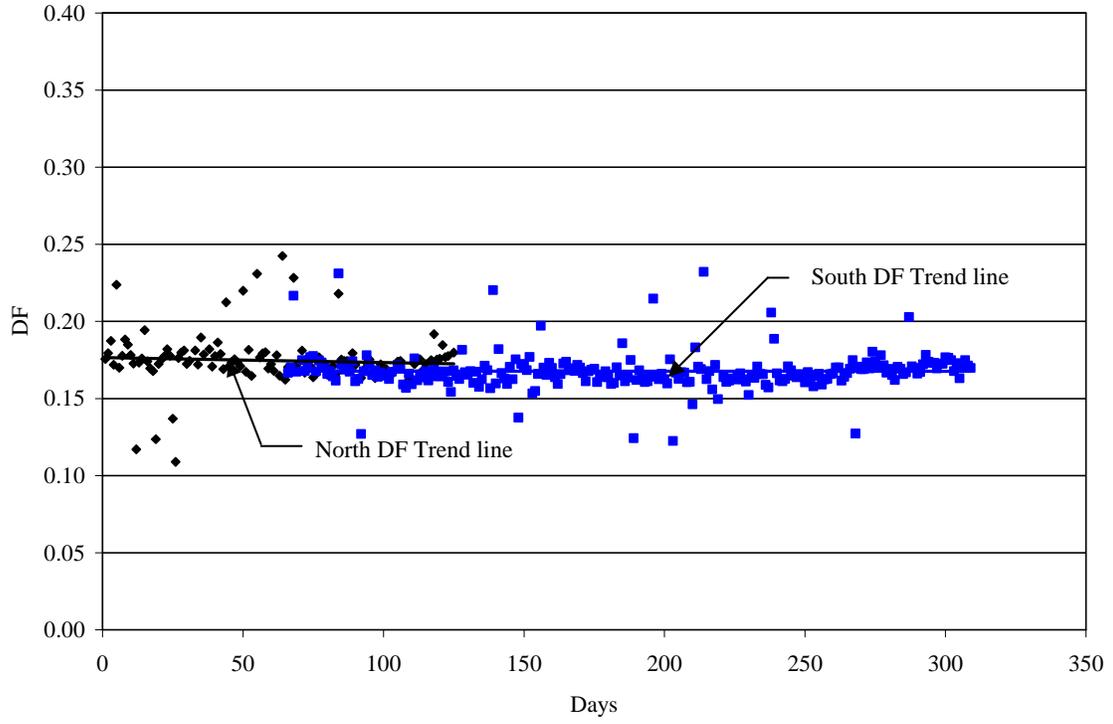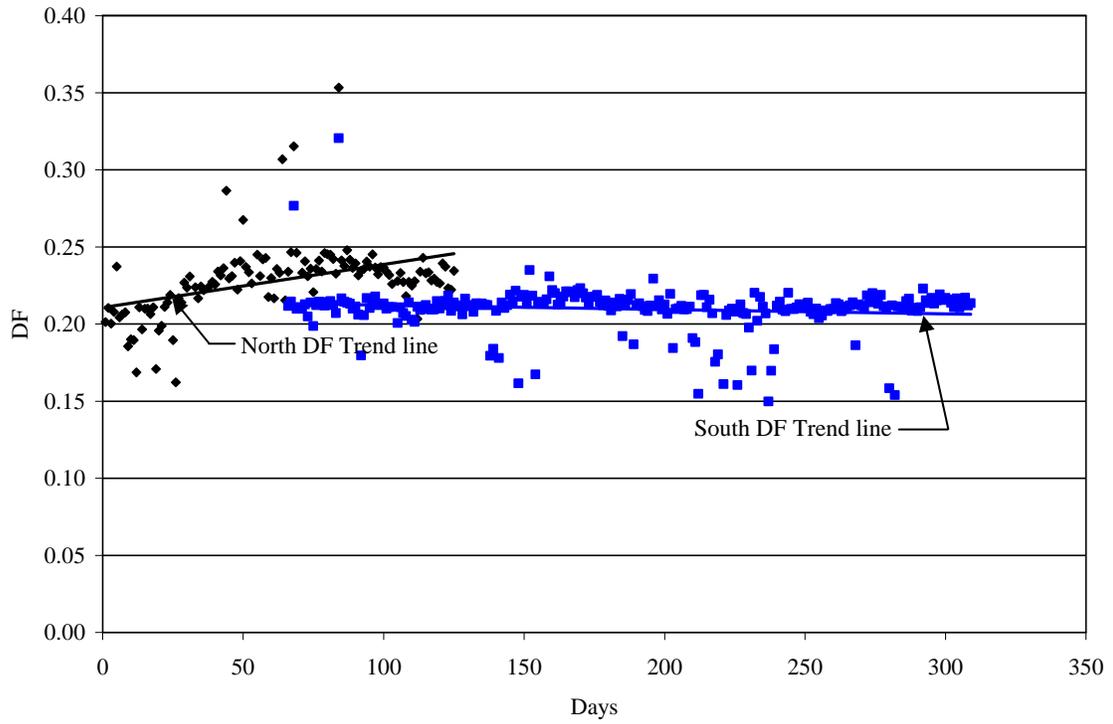
d. Girder 4

e. Girder 5

f. Girder 6

Figure 5.23. Average DF per day over time

Table 5.3. RMS data from long-term ambient traffic and controlled load test DFs

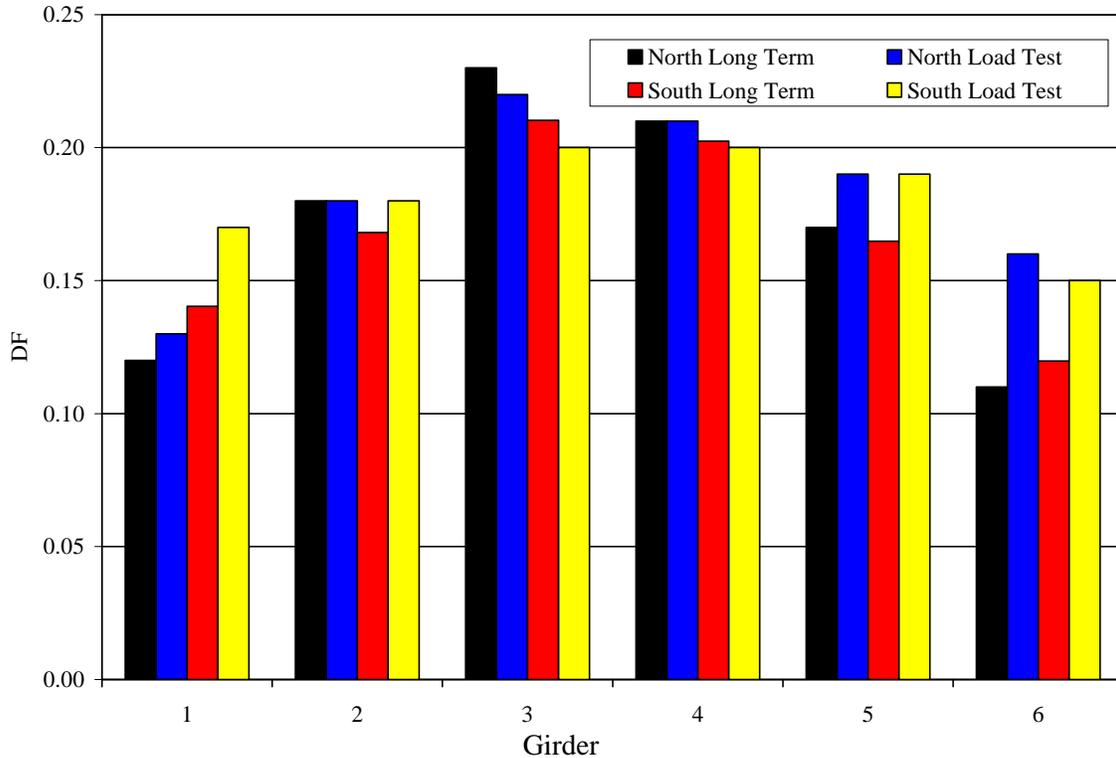|	Girder 1	Girder 2	Girder 3	Girder 4	Girder 5	Girder 6
Long-term DF RMS data						
North	0.12	0.18	0.23	0.21	0.17	0.11
South	0.14	0.17	0.21	0.20	0.16	0.12
Load test DF RMS data						
North	0.13	0.18	0.22	0.21	0.19	0.16
South	0.17	0.18	0.20	0.20	0.19	0.15

Figure 5.24. DF RMS data from long term ambient traffic and controlled load test

The American Association of State Highway and Transportation Officials (AASHTO) Standard Specifications for Highway Bridges (AASHTO 1996) specifies that the lateral load distribution factor for interior girders is determined by S/7.0, where S is defined as the spacing of girders in ft.. For this bridge, the DF for the interior girders would be 1.23 wheel lines per girder or 0.62 vehicles per girder. For comparison, the largest measured DF from the ambient traffic data was 0.35 vehicles/girder, but the typical DF values for interior girders were much lower (approximately 0.20 to 0.25). It must be noted that the ambient traffic lane position may not cause the worst-case DF values, as inferred by the AASHTO values, and that the experimental DF values only represent a single vehicle on the bridge, which the AASSHTO values are not meant to represent. Rather, they are intended to represent the local results from multiple vehicles.

Neutral Axis Location

The NA location is calculated at seven different positions on the bridge. Table 5.4 shows the relationship between the seven positions, labeled with an NA designation and the girder number and span location. The NA location is referenced from the bottom of the girder, and all dimensions are in inches.

Table 5.4. Location of NA designations on bridge

NA designation	Girder number	Cross section location
G1N	1	North midspan
G2N	2	North midspan
G3N	3	North midspan
G1S	1	South midspan
G4S	4	South midspan
G5S	5	South midspan
G6S	6	South midspan

NA from controlled load tests. Figure 5.25 shows the NA location for run 2 of the controlled load test. Data from all girders except girder 6 are presented. The NA was not calculated at G6S during run 2 due to insufficient strain in the bottom flange of girder 6 (i.e., the bottom flange strain did not meet the threshold of 25 me). The NA location on all of the plots can be characterized by three conditions: (1) NA location predominantly at the top flange, (2) NA location predominantly below the top flange, and (3) NA location at least partly above the top flange.
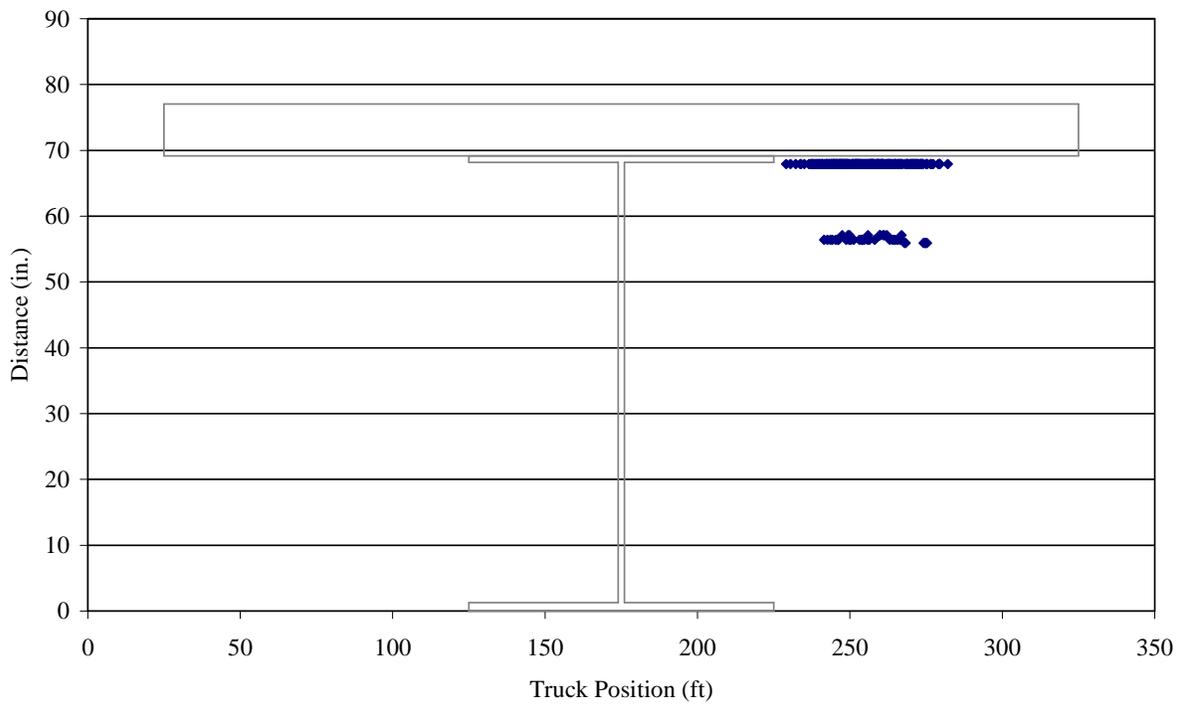

a. G1N and G1S

99

b. G2N

c. G3N
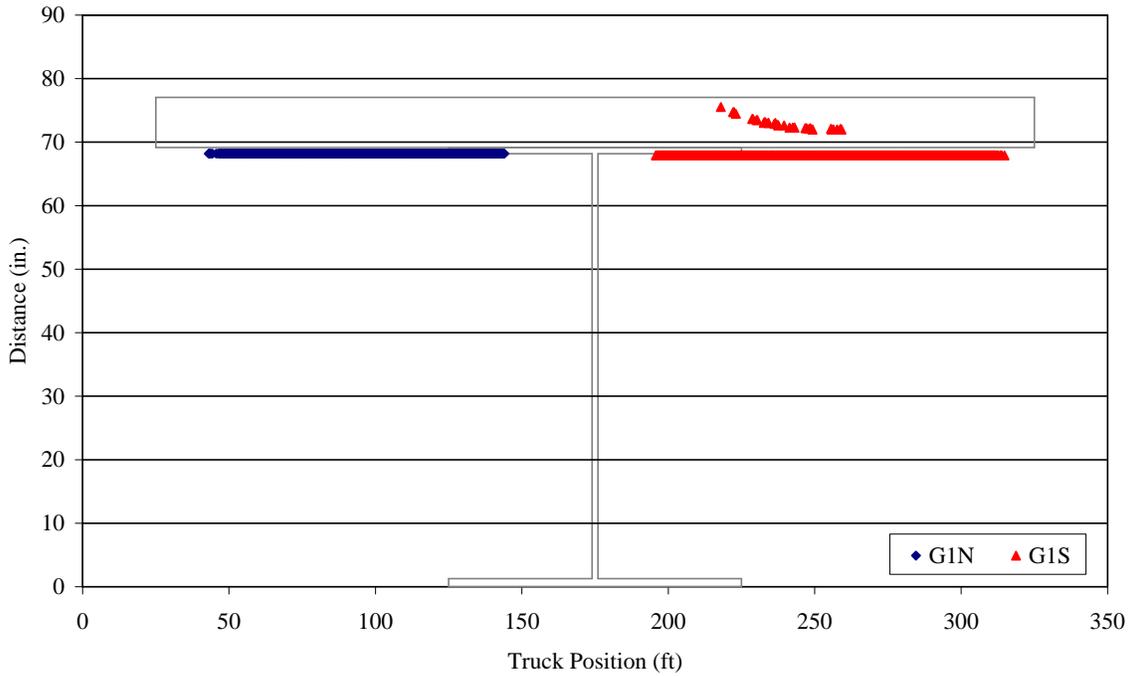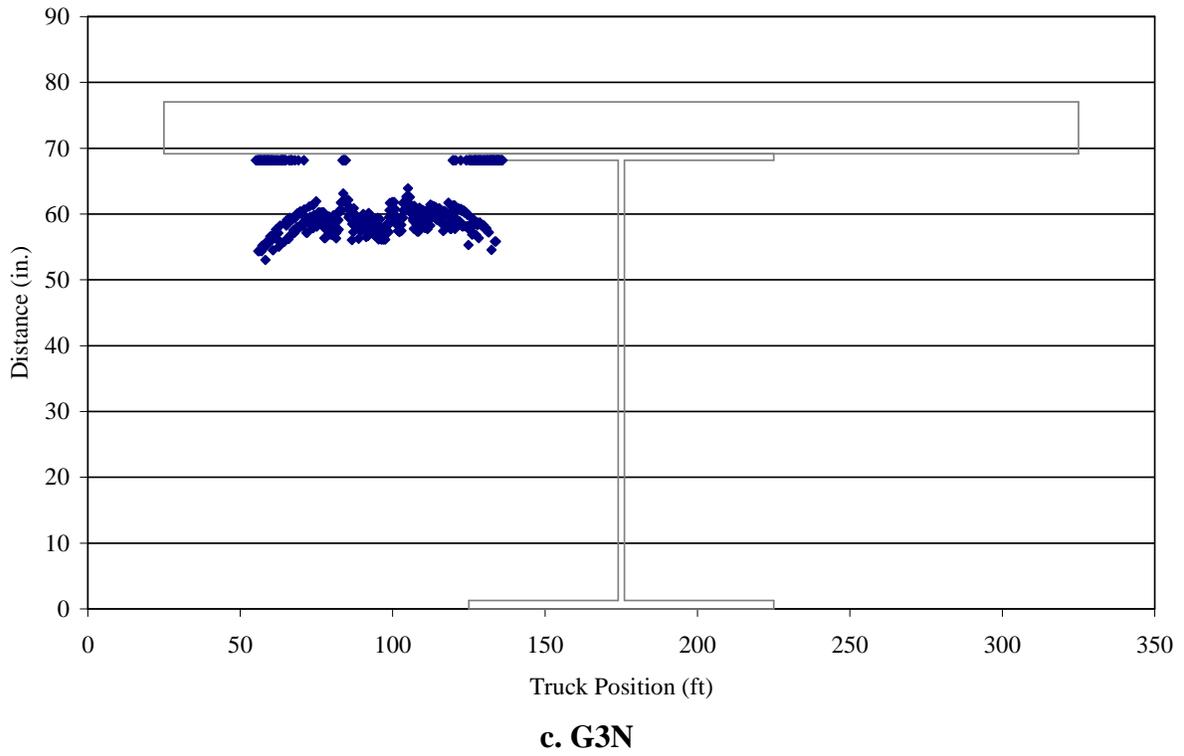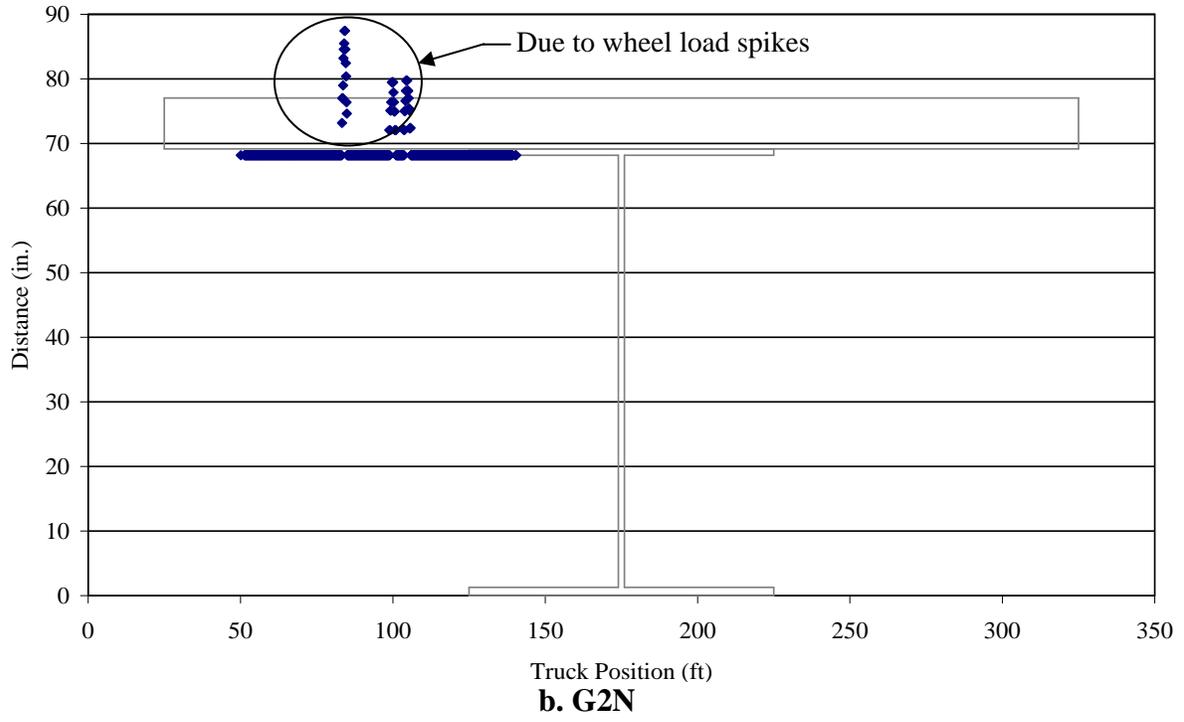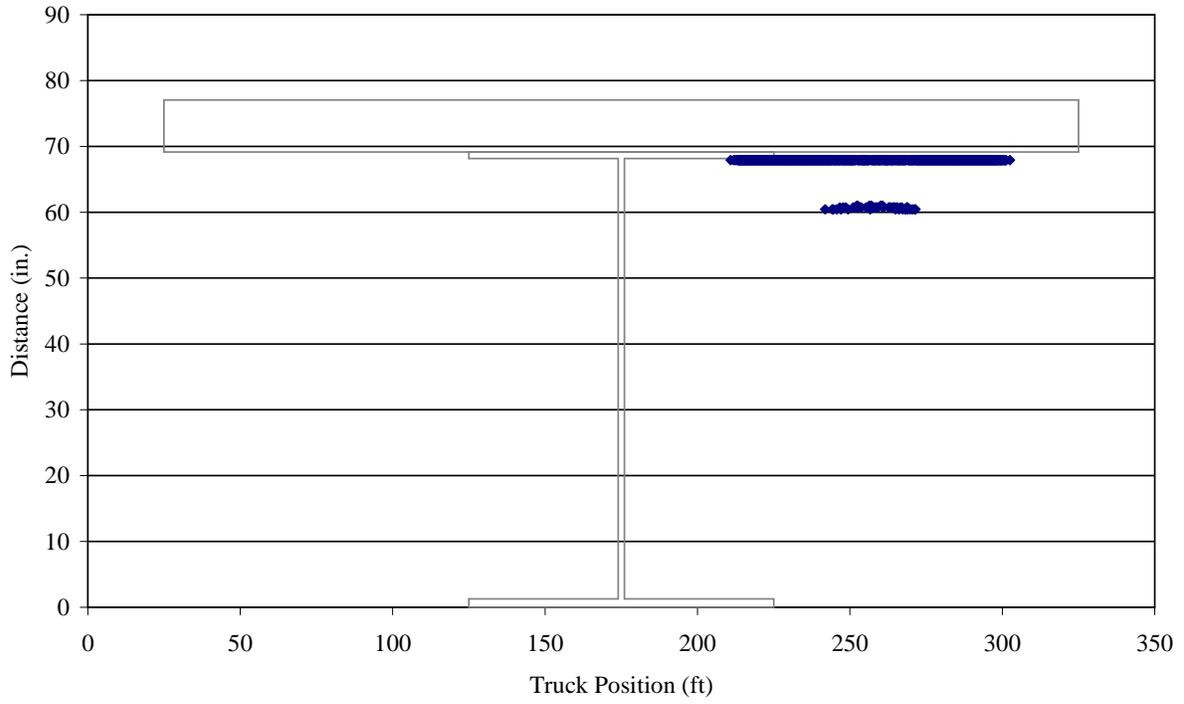
d. G4S

e. G5S

Figure 5.25. NA location from run 2 of the controlled load test

101

NA location predominantly at top flange. Figures 5.25a and 5.25b show girder 1 and 2 NA data, respectively, for run 2, in which the NA location at G1N and G2N is predominantly at the top flange location. The NA is calculated at two positions on girder 1: the north (G1N) and south (G1S) midspans. The NA at G1S rises above the top flange several times, unlike in the data for G1N. This anomaly will be discussed below. Figure 5.25b shows the NA data from girder 2 (G2N), where the NA location is at the top flange for essentially the entire run. The few spikes in the data, in which the NA location is above the top flange, can be attributed to localized effects. As shown in the previous sections, when the load truck axles cross directly over or extremely close to the location of the top flange FBG, a positive (tensile) spike in the strain occurs in the top flange. Figure 5.26 shows the location of the west load truck wheels for run 2 of the controlled load test in relation to the girder 2 top flange sensor.
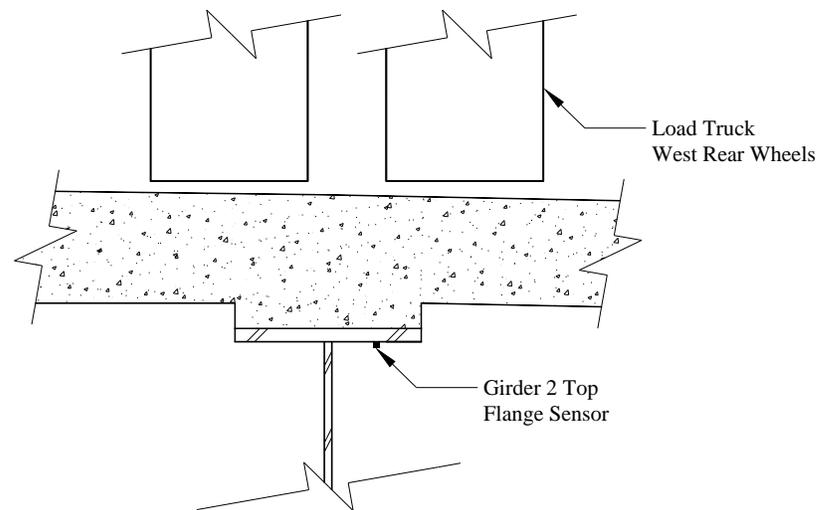

Figure 5.26. Load truck wheels in relation to girder 2 top flange sensor for run 2

NA location predominantly below the top flange. Girder 3 (G3N) and girder 4 (G4S) NA data from run 4 are shown in Figure 5.27. The NA location moves down when the load truck approaches the location of the sensor. Notice that when the NA is below the top flange there are no transition data points between the points at which the NA is at the bottom of the top flange and at which it is well below the top flange. This is an anomaly caused by the DSP, since strain values less than ±1.6 me are set equal to 0.0 me. Consequently, the NA is shown at the top flange when it may actually be slightly below the top flange. Since run 4 provides symmetric truck loading to girders 3 and 4, the NA locations should be similar for the two positions, assuming the north and south span lengths are similar (which is true) and the girder stiffnesses are similar (which is not true). G3N has a lower NA location, which is below the top flange more often than for G4S. This is likely due to the lower girder stiffness in relation to the deck stiffness in the south span than in the north span.
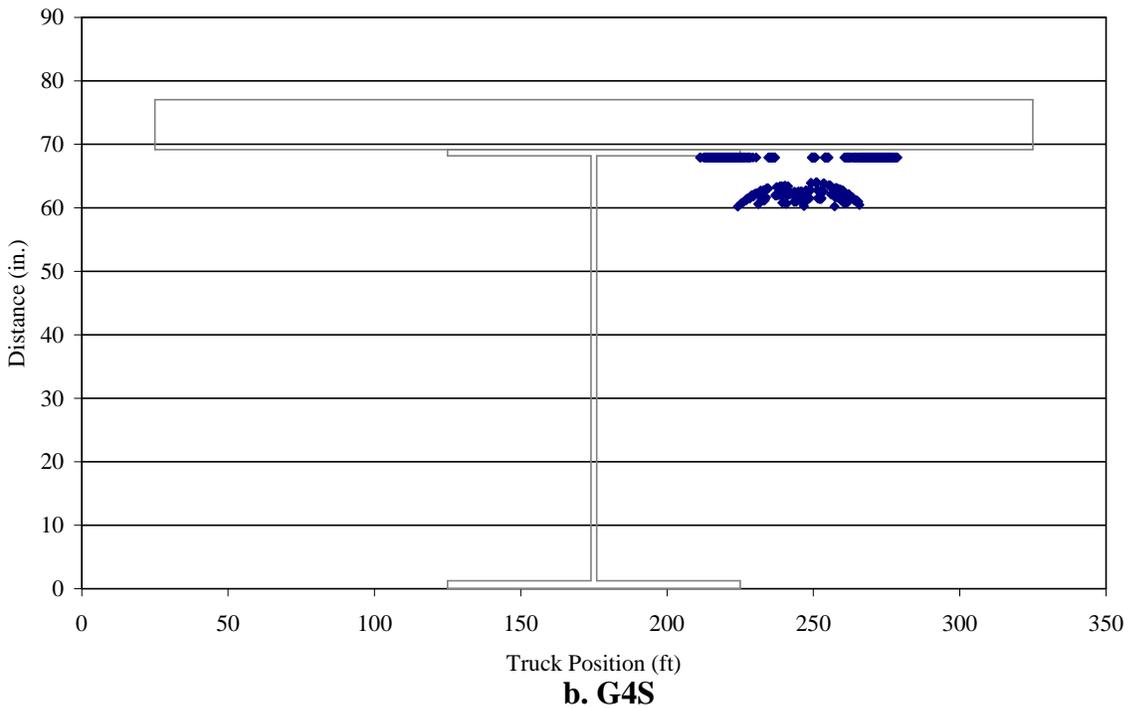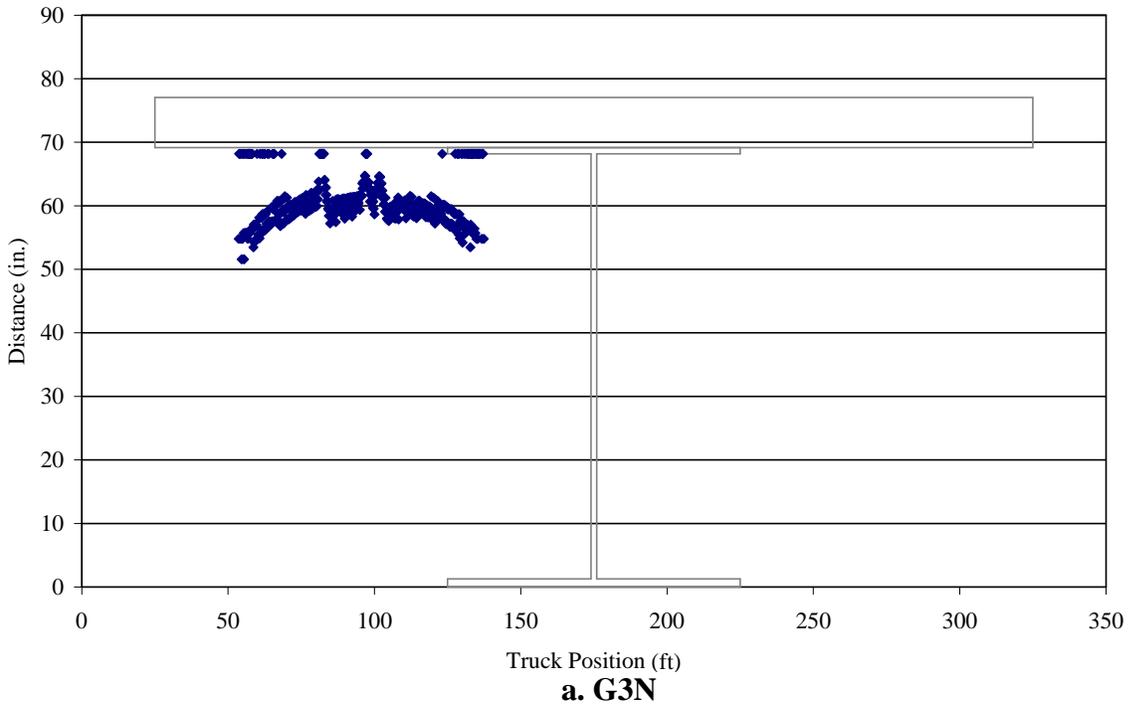
a. G3N

b. G4S

Figure 5.27. NA location from run 4 of the controlled load test

NA location at least partly above the top flange. Figure 5.28 shows several conditions in which the NA is at least partly above the top flange. The same anomaly discussed above occurs when the NA is also above the top flange. Therefore, NA is forced (through the DSP) to be at the top

103

flange when it may be slightly above the top flange. The girder 5 (G5S) NA is above the deck (the barrier near girder 5 in compression) at several points, some of which are most likely due to localized effects from the truck axle (the three peaks near the center). Note that the localized effects on G5S from the truck axle occurred during a situation that is symmetric to the localized effects on G2N discussed above. Girder 6 (G6S) has more data points above the top flange than does girder 5 (G5S). This signifies a higher deck stiffness in girder 6 than in girder 5, which is most likely due to the degree of contribution of the barrier rails near girders 5 and 6.

The NA locations for G1S during run 2 and G6S during run 6 (symmetrical loading on transversely symmetrical girders) are shown together in Figure 5.29. Notice how the data points have the same magnitude and trend. Although the exact reason for the shape of the anomaly is unknown, note the consistency and transverse symmetry behavior exhibited by girders 1 and 6 at the south midspan. The NA location above the top flange can be attributed to positive (tensile) strains on the top flange.

NA time history from ambient traffic. The NA location for each girder is shown below. Each data point represents the average NA location for a particular day in the monitored life of the bridge. If a point is not shown, the NA was not calculated at that position for a particular day because no traffic events satisfied the minimum strain threshold. The RMS of the NA location time history is also provided.

The G1N, G1S, G2N, G5S, and G6S long-term data (Figure 5.30) show that the NA location is very near the top flange. This is consistent with the controlled load test data for the girders near the barrier rails (i.e., girders 1, 2, 5, and 6). Also note that there are fewer G1N, G1S, and G6S data points than for the other girders. This validates the DF data presented earlier, in which girders 1 and 6 had lower DFs than the other girders. Since the load distributed on girders 1 and 6 is lower, the strain in girders 1 and 6 may not be large enough for the NA to be calculated. When G3N and G4S are compared, the NA location for G3N is lower and more varied than the NA location for G4S, indicating that G4S has a higher deck stiffness in relation to the girder stiffness than G3N. The same observation was made for the controlled load test data.

A summary of the long-term and controlled load test NA RMS data for each girder is shown in Table 5.5 and Figure 5.31. The long-term and load test RMS data are close for each girder except girder 3. This could be due to the difference in the geometry of the load truck compared to that of the ambient traffic (girder 3 may be affected by this more than the other girders for reasons discussed below). Comparisons can be made between transversely symmetric girders, although the symmetrical indices are not in the same span in most cases. Girders 3 and 4 show the largest difference in the symmetric girders, as one would expect from the discussion above. The difference in girders 3 and 4 could be due to the stiffness difference (due to differing cross-sectional properties and boundary conditions) between the north and south spans. Since girders 3 and 4 have the lowest stiffness (girders 1, 2, 5, and 6 have concrete barriers and sidewalks above them), the differences in stiffness resulting from different cross sections of the north and south girders would affect the NA location on girders 3 and 4 more than on girders 1, 2, 5, and 6. Table 5.6 compares the inertia (related to the stiffness) of the composite sections and the theoretical NA location at the north and south midspan of girders 3 and 4 for several different assumed f'c values. (Since concrete continues to gain strength after the specified 28 days, the actual f'c is

unknown.) The NA is about 1 in. higher in the south span than in the north span for each calculation. Table 5.6 implies that the difference in cross sections between the north and south midspan is most likely not the main factor in the difference between the NA location for girders 3 and 4.

After observing the controlled load test and long-term ambient data, an argument could be made that the threshold for the DPP to calculate the neutral axis (25 $\mu\epsilon$ on the bottom flange) is too low, since most of the data are concentrated near the top flange. This concentration would cause smaller traffic events, which occur more frequently than larger events and cause less significant potential bridge damage or deterioration than larger events, to skew the results of the NA data.
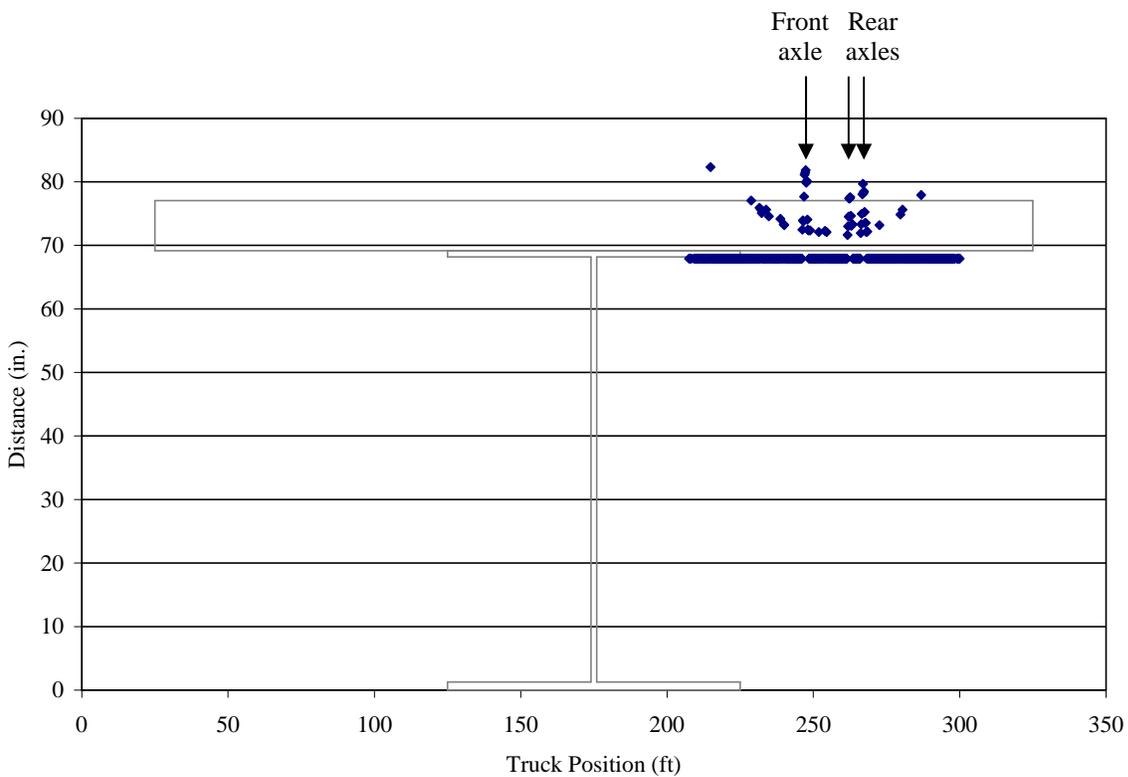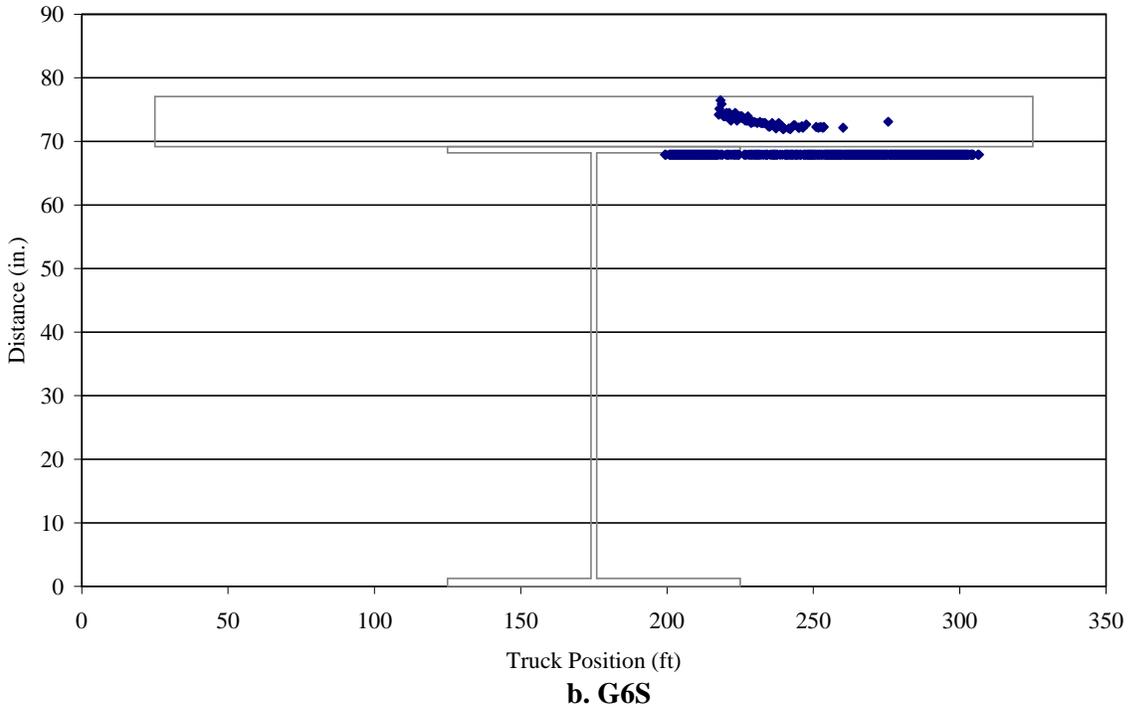

a. G5S

b. G6S

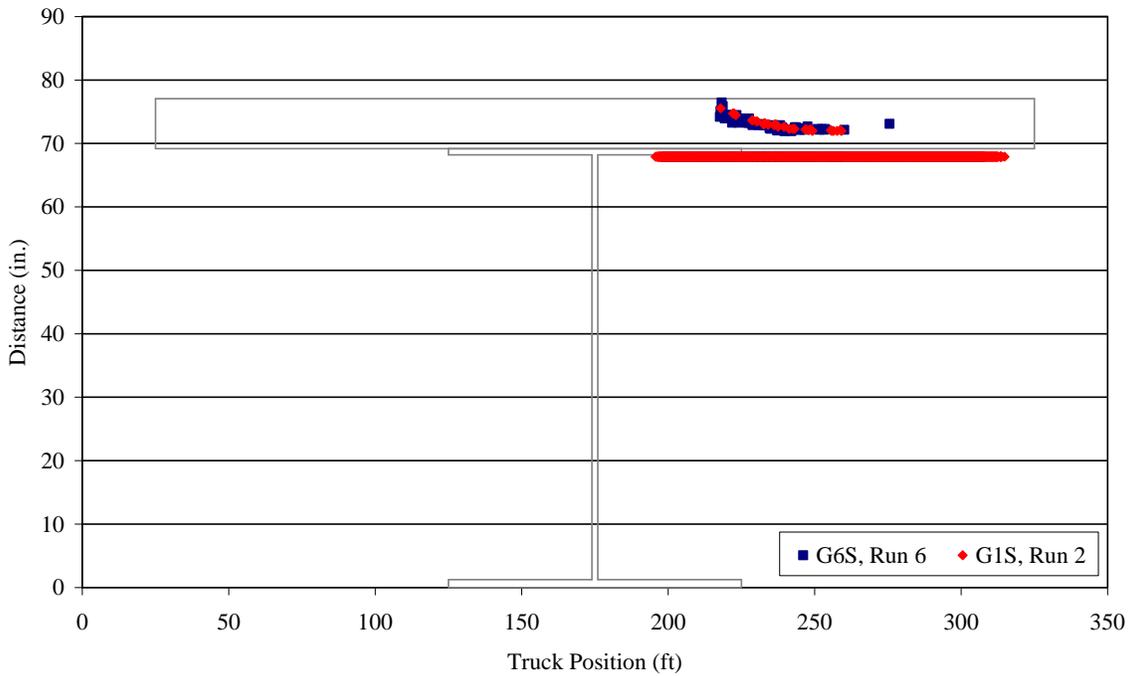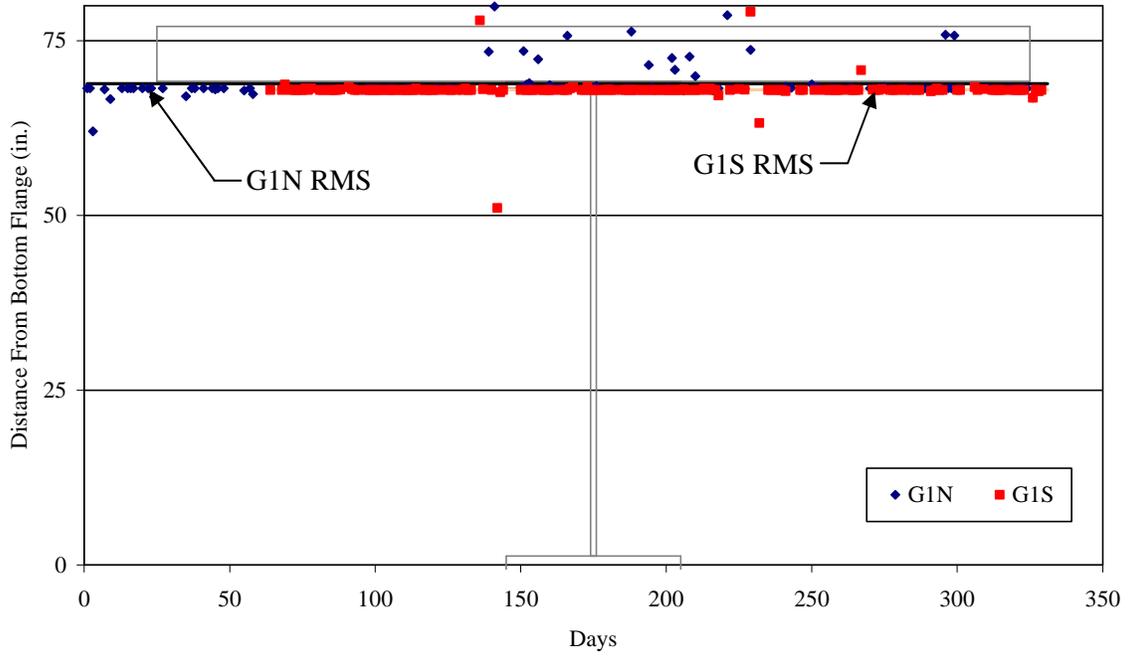**Figure 5.28. NA location from run 6 of the controlled load test**
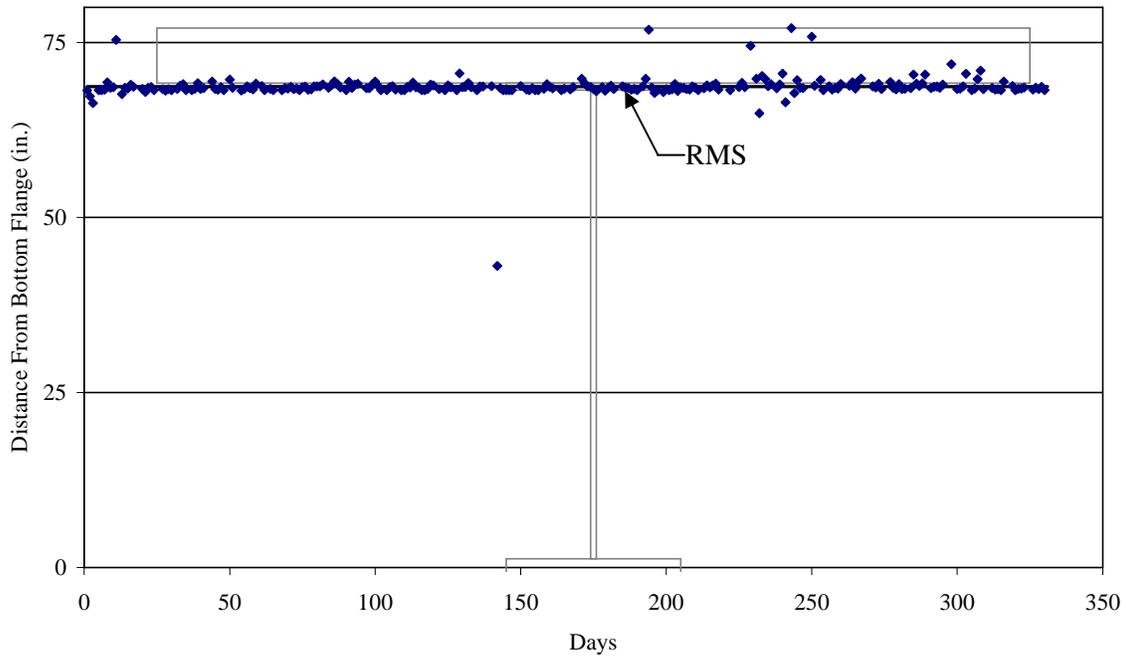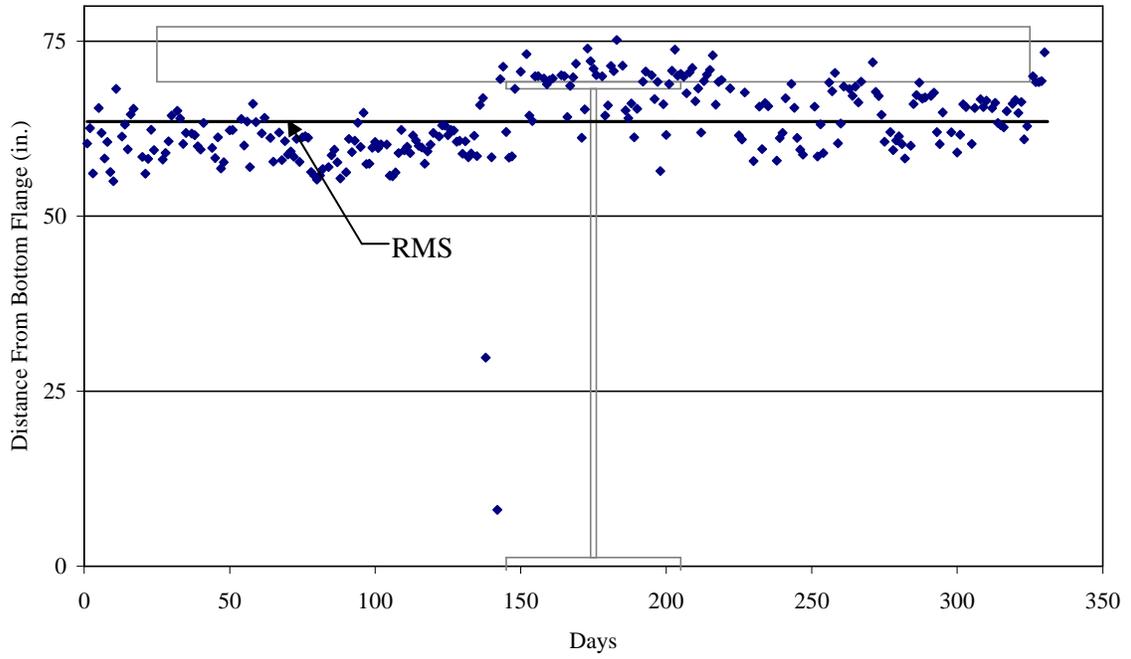

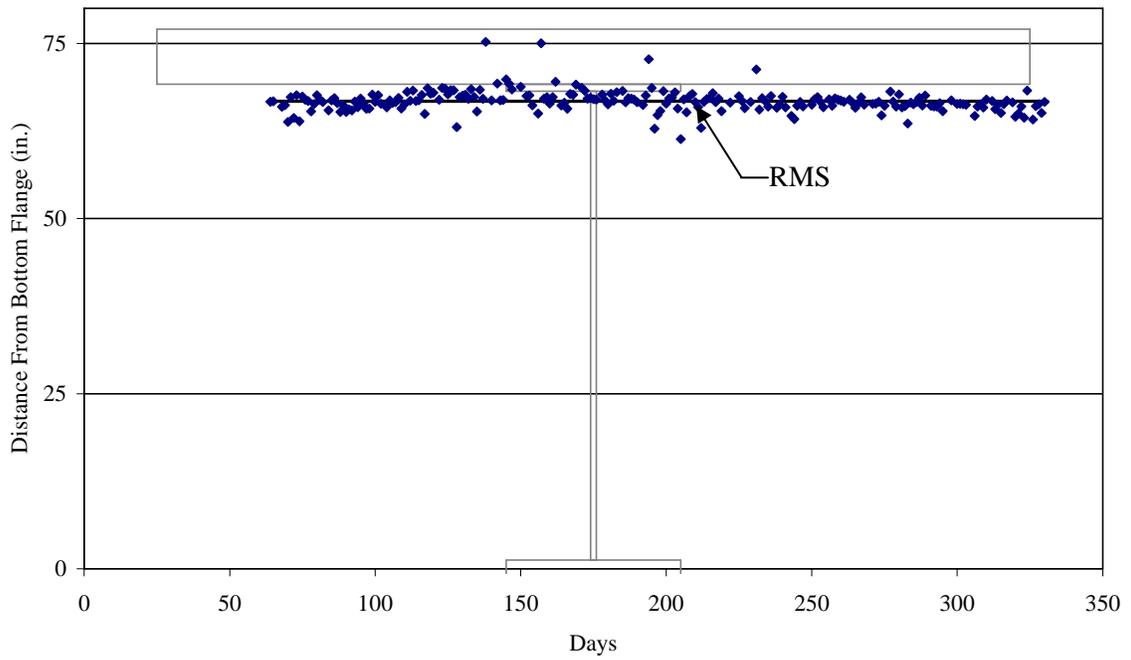**Figure 5.29. NA location from runs 2 and 6 of the controlled load test**

a. G1N and G1S
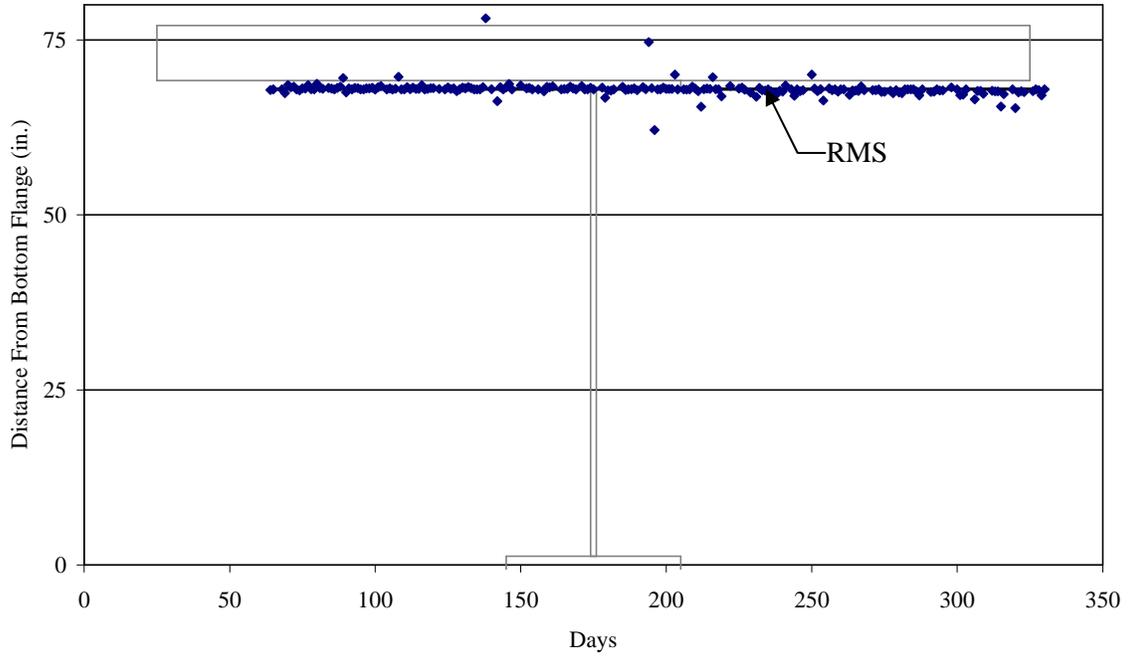

b. G2N

c. G3N

d. G4S

e. G5S
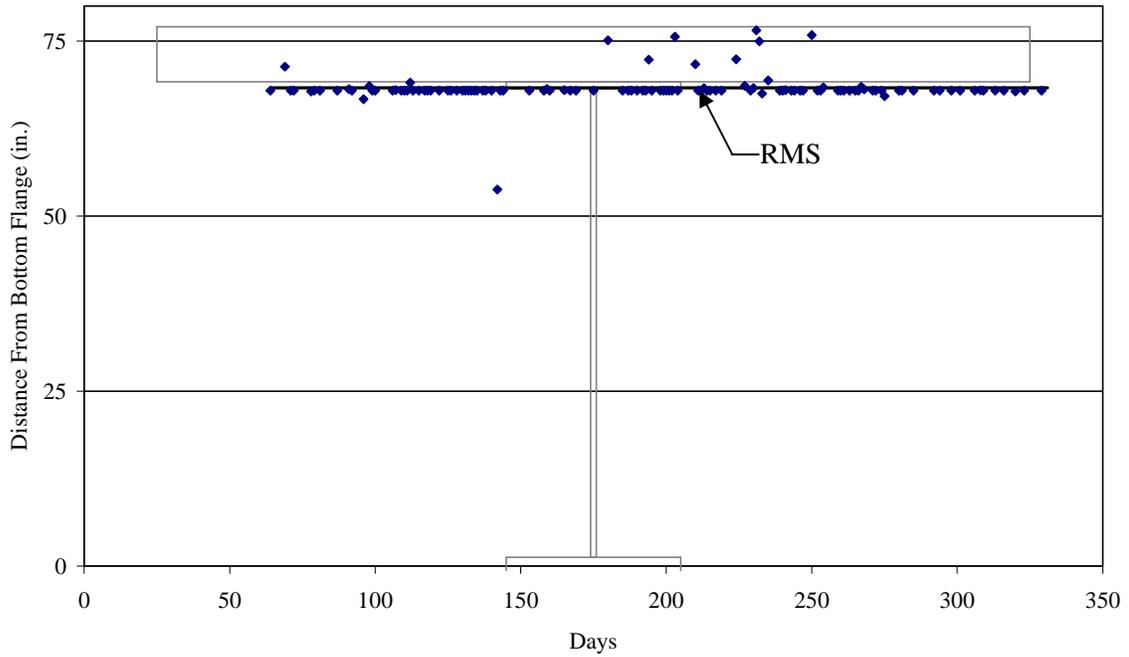
f. G6S

Figure 5.30. Average NA location per day over time

Table 5.5. NA RMS data from long-term ambient traffic and controlled load test

	Girder1 (G1N/G1S)	Girder 2 (G2N)	Girder 3 (G3N)	Girder 4 (G4S)	Girder 5 (G5S)	Girder 6 (G6S)
Long Term RMS	68.83/67.97	68.68	63.51	66.76	67.95	68.32
Load Test RMS	68.19/67.98	68.01	62.33	66.75	67.99	68.37
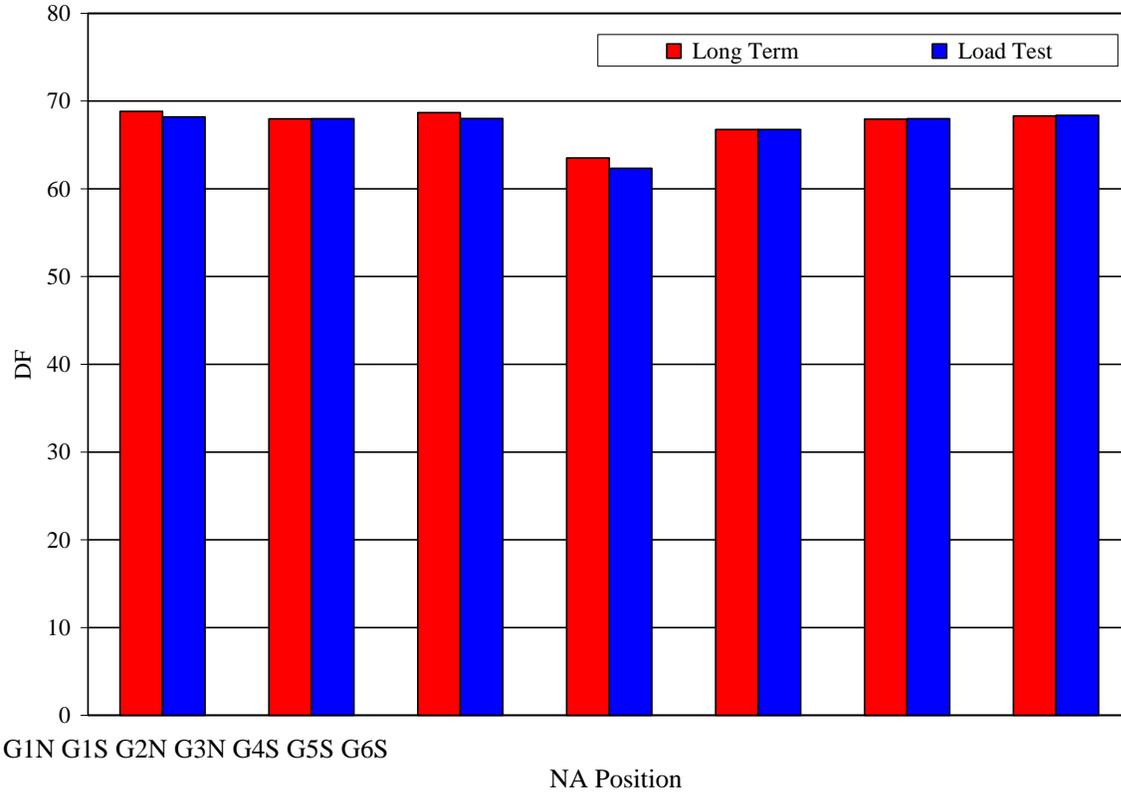
Figure 5.31. NA RMS data from long-term ambient traffic and controlled load test

Table 5.6. Theoretical composite I for girders 3 and 4 and NA location at the north and south midspans

Assumed f'c of deck	North midspan		South midspan	
	Composite I	NA location	Composite I	NA location
5 ksi	134,152 in.^{4}	57.81 in.	117,040 in.^{4}	58.90 in.
7 ksi	138,819 in.^{4}	59.36 in.	120,955 in.^{4}	60.38 in.
9 ksi	144,076 in.^{4}	61.09 in.	125,326 in.^{4}	62.03 in.

110

End Restraint Ratio

The ER data presented below correlate the ratio of the midspan bottom flange strain to the abutment bottom flange strain (on the same girder) as a vehicle crosses the bridge. The ratio is intended to be used as a qualitative measure of changes in the longitudinal stiffness characteristics of the girders over time. It is important to note that the results from girder 1 are dependant on the bottom flange abutment sensor on girder 1, which is the sensor that was found to be unreliable in short-term loading conditions. Therefore, the girder 1 ER is not shown for the controlled load tests.

ER from controlled load tests. Perhaps the most significant source of information from the ER data is from run 2 for girders 2 and 3 (see Figure 5.32). As shown in this figure, the strain magnitude at the midspan increases more rapidly than at the abutment as the vehicle approaches the midspan. To illustrate a typical plot for a girder far from the applied load, Figure 5.33 shows the girder 2 ER for run 6. Note that the ER is approximately 50% less than the ER close to the applied load and has a significantly different shape. The plots shown and the results noted are typical for all data from the controlled load test.

ER time history from ambient traffic. This section presents the average daily ER before the end of September 2004 for the girders instrumented to calculate the ER over time (girders 1, 2, and 3). As mentioned above, the data after October 2004 are not included in this analysis because the related sensors have at times performed unreliably since then. The ER is plotted with both a linear trend line and the long-term RMS. There is a slightly decreasing trend over time for all three girders. This trend may be caused by events similar to those listed for the change of the DF over time. The ER data for girder 1 shifts significantly after about 60 days, unlike the gradual change seen for girders 2 and 3. The girder 1 bottom flange sensor at the abutment began to perform unusually and is thought to be performing unreliably under both live and long-term temperature loads (as discussed above). The time at which the sensor is thought to have begun performing unreliably is shown on the plot in Figure 5.33. The RMS of the long-term ER data was found for each girder; these values are shown in Table 5.7 and in Figure 5.34. By definition, the RMS is a positive number, but the vast majority of the ER data are negative. Therefore, for plotting convenience a negative value is assigned to the RMS.

As stated above, with the limited amount of reliable data available, the trend lines shown for the long-term data may not adequately represent the trends in the data. The RMS data provide a better basis than the trend line for monitoring the changes of the bridge indices over time.

Strain Cycle Counting

Strain cycle counting using the rainflow counting method is used to quantify behavior from ambient traffic in two ways: (1) monitoring the number of strain cycles due to individual ambient traffic events at different locations on the bridge and (2) approximating the number of vehicles that use the bridge on a daily basis.

Ambient Traffic Event Strain Cycles

The results from the rainflow counting process are shown below. The sensors are grouped by their location on the bridge. Data are presented for the first 110 days of monitoring for the north midspan sensors, abutment sensors, and weld splice stress concentration sensors. The south midspan sensors were installed later, but have performed well to the end of this project. Due to the missing data from October and early November 2004, the data used to analyze the south span strain cycle counting add up to about 300 days. The term "bin strain" in Figure 5.35 refers to the average of the bin range (the bin range is 10 me). For example, a 15 me bin strain would contain strain cycles ranging from 10 to 20 me.

Figure 5.35 shows the distribution of cycles for the north midspan bottom flange sensors. For all bin sizes except 25 me, girders 1 and 6 typically record the smallest number of cycles, followed by girders 2 and 5, and girders 3 and 4 report the largest number. This is to be expected due to the proximity of these girders to the live loads. Possible reasons for the difference in the 25 me bin include (1) the fact that girders 1, 2, 5, and 6 have cycles recorded in the 25 me bin that were recorded for girders 3 and 4 in the 35 me bin (i.e., since girders 1, 2, 5, and 6 are loaded less than girders 3 and 4, the cycles from a particular event may not appear in the same bin for each girder) and (2) the size of the vehicles using the bridge may not be a normal distribution (i.e., there are small vehicles that register strain in the 15 me bin and larger vehicles that register strain in the 35 me bin, but no medium-sized vehicles that register in the 25 me bin). For the 15 me bin, girder 3 shows significantly more cycles than girder 4, suggesting more southbound traffic than northbound. With the exception of the first bin, the sensors that are transversely symmetric on the bridge to each other have nearly the same number of cycles.
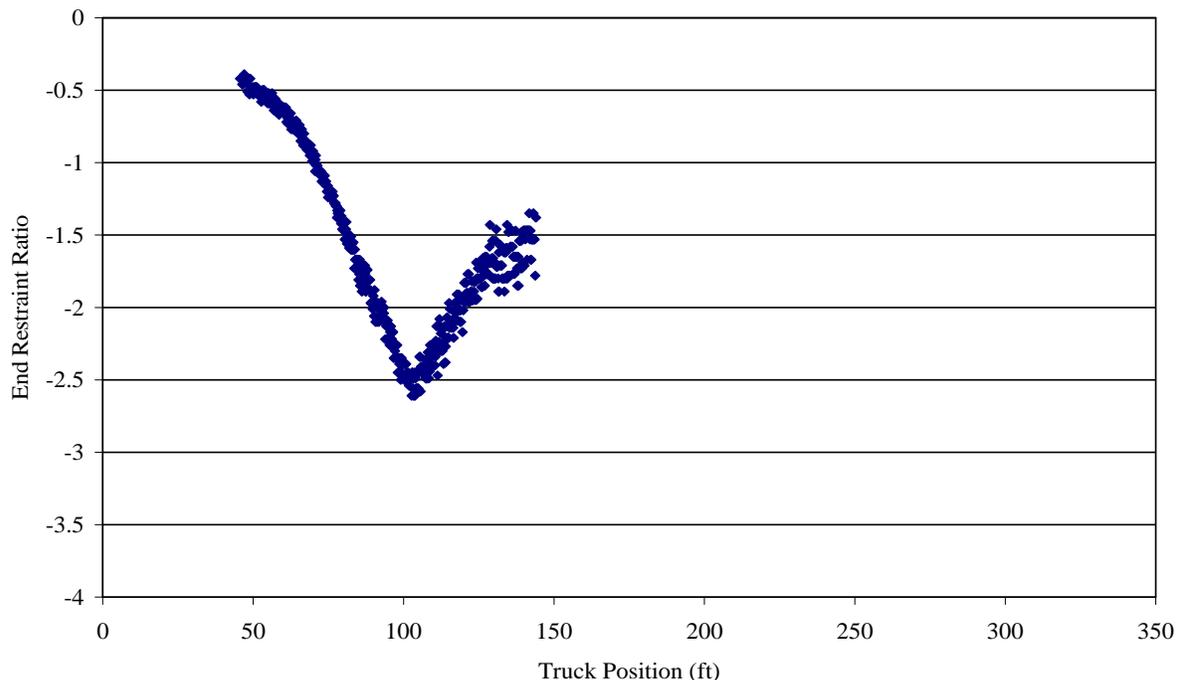
a. Girder 2

112
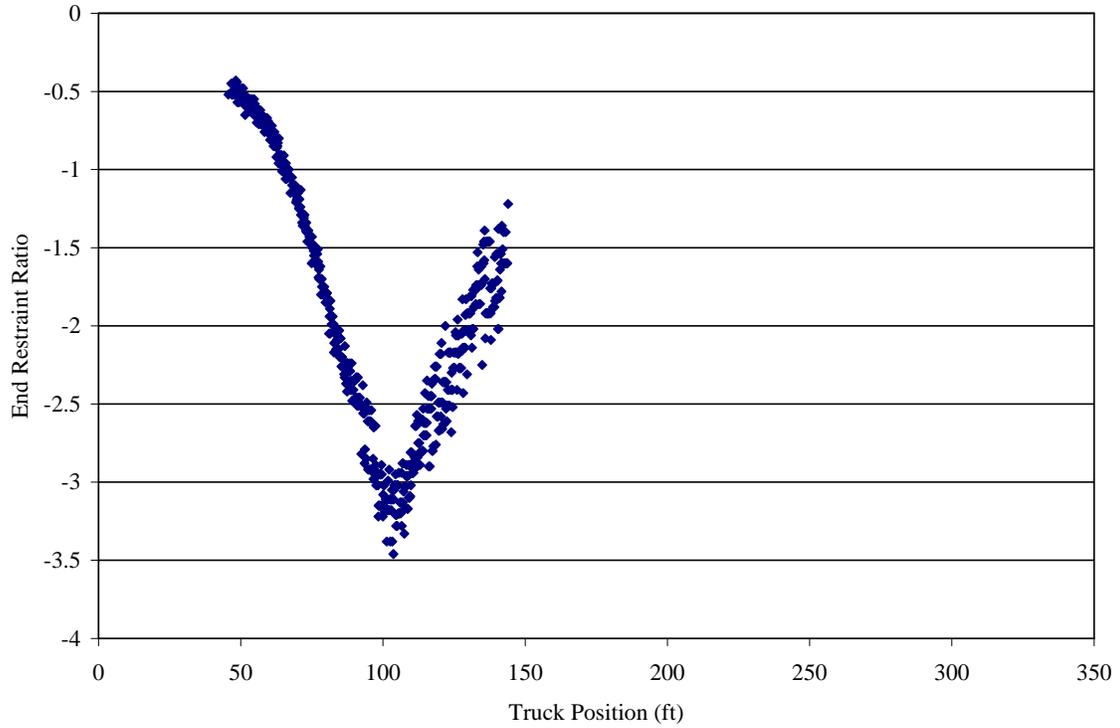
b. Girder 3

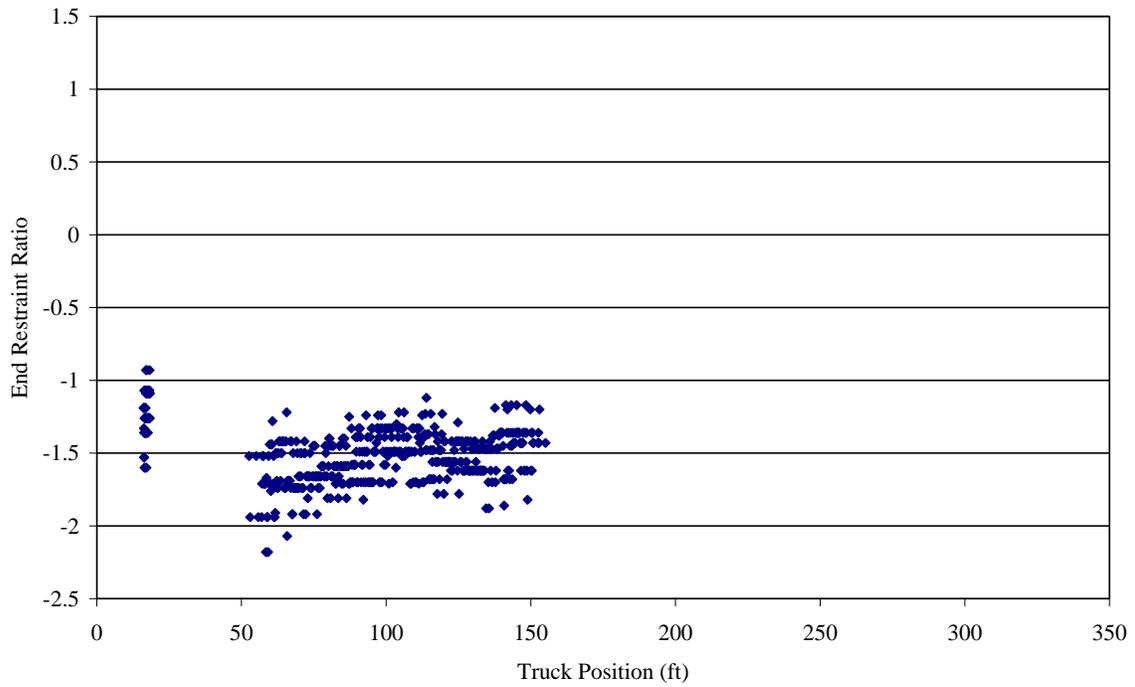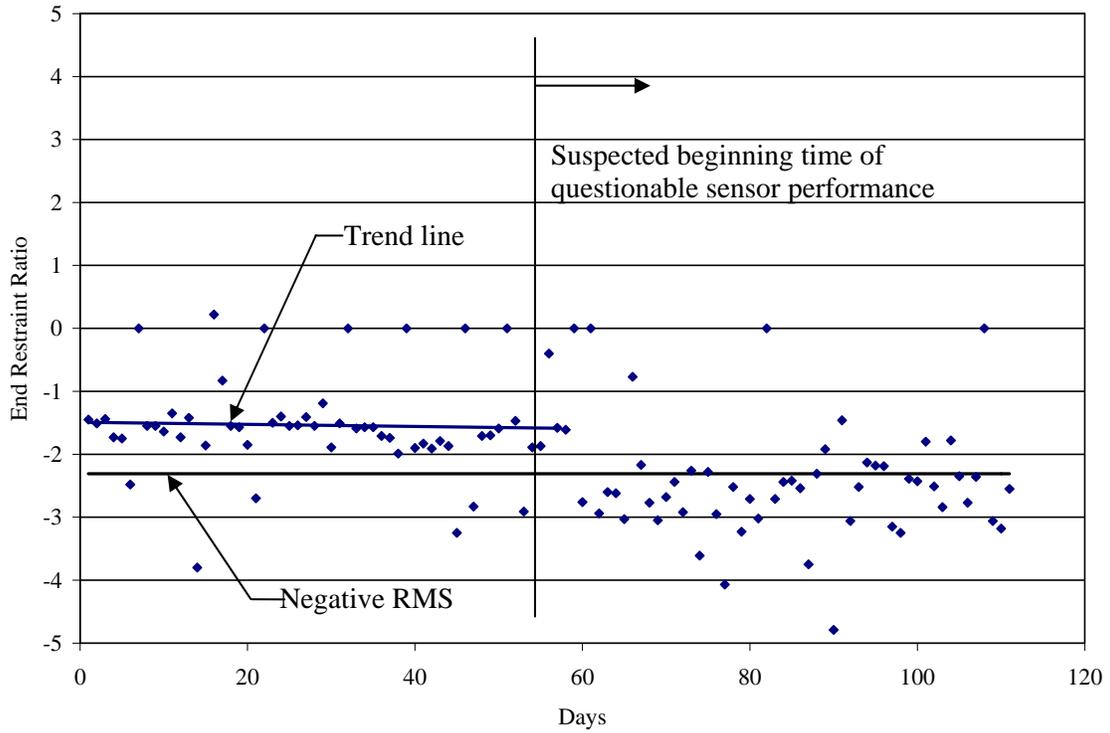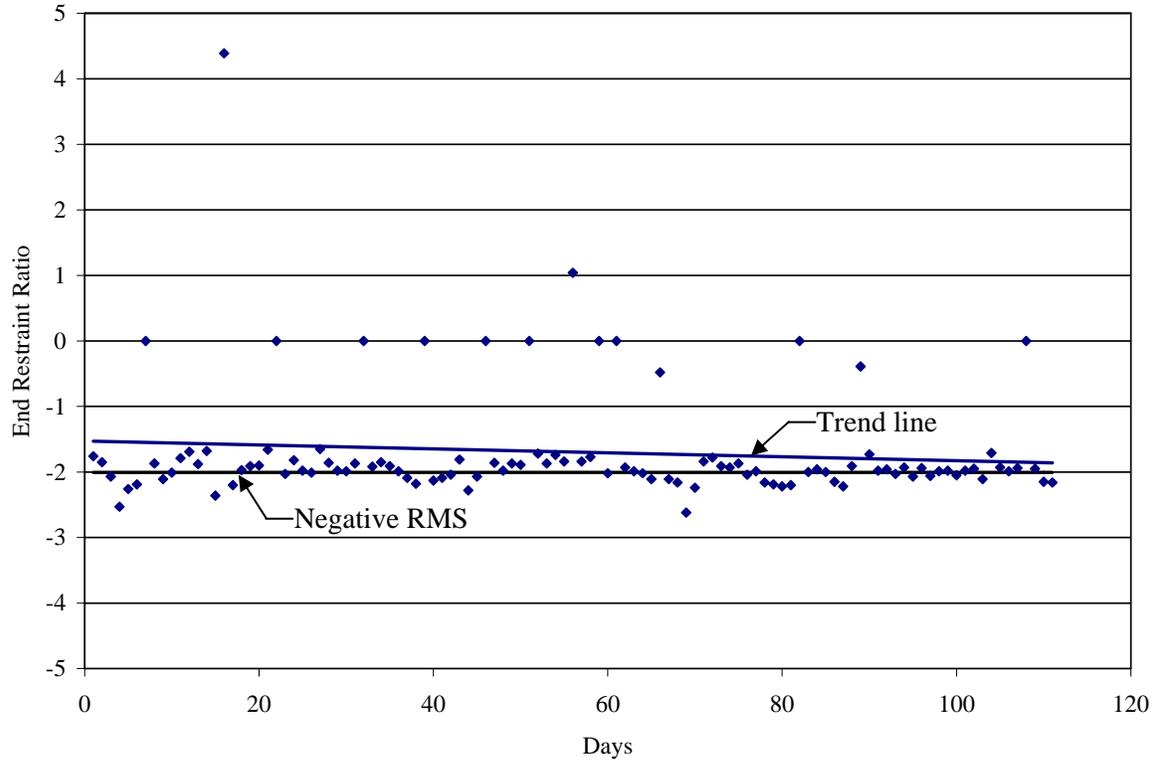**Figure 5.32. ER from run 2 of the controlled load test**

Figure 5.33. ER for girder 2 from run 6 of the controlled load test

113

Table 5.7. Long-term ER—negative RMS values

	Girder 1	Girder 2	Girder 3
RMS	-2.31	-2.01	-2.68

a. Girder 1

b. Girder 2
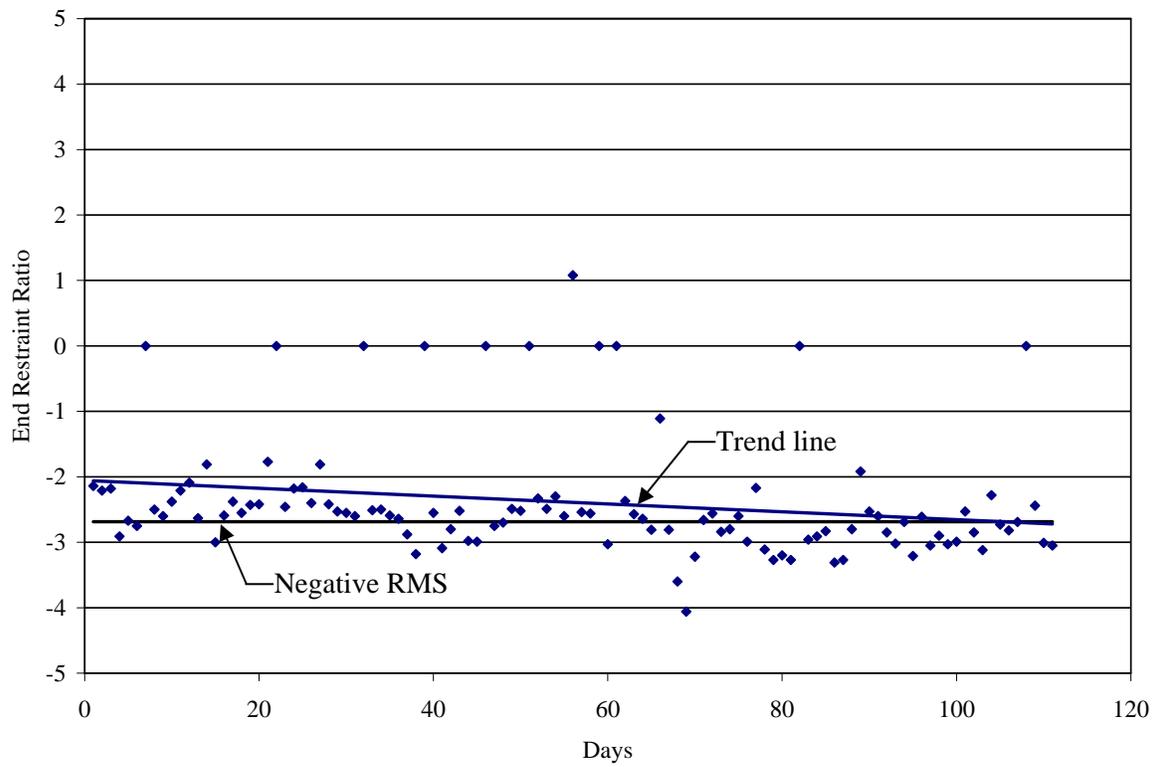
c. Girder 3

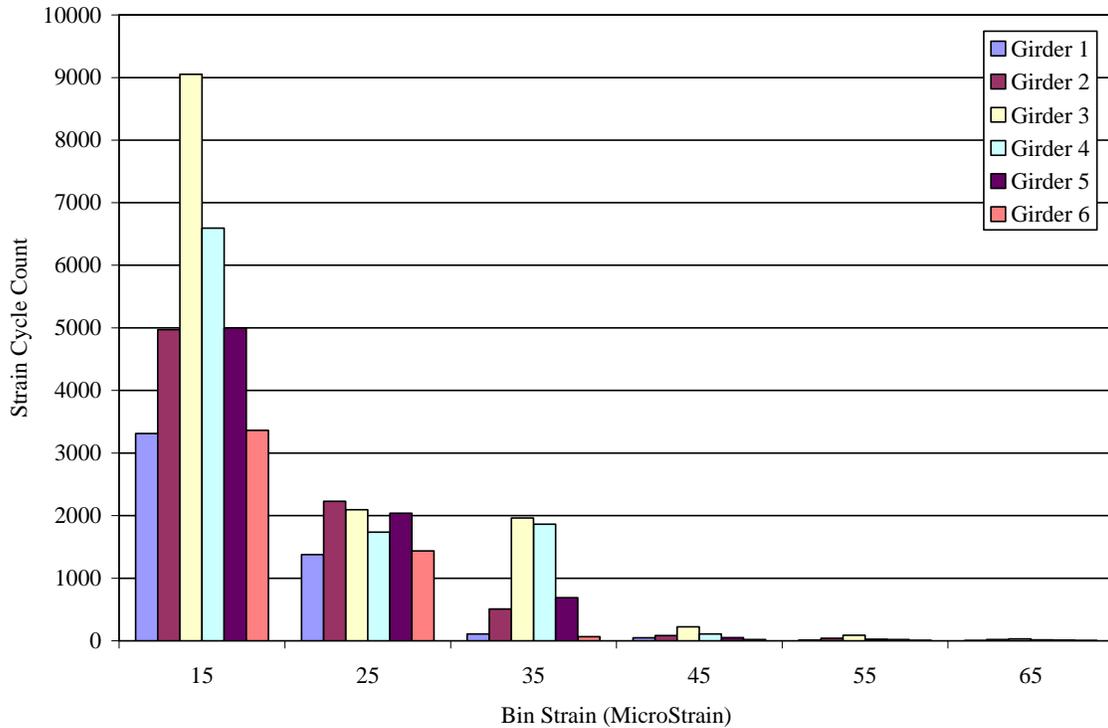**Figure 5.34. Average ER per day over time**

Figure 5.35. Rainflow counting results from bottom flange sensors at the north midspan

Figure 5.36 shows north midspan top flange sensor data for girders 1, 2, and 3. Note that the girder 3 data are significantly larger than the data for the other two girders. Also note that girder 3 also had significantly more 15 με bin cycles at the bottom flange of the north midspan. Girders 1 and 2 have a smaller number of strain cycles due to the larger stiffness (as a result of the sidewalk and barriers rails near girders 1 and 2). Girder 3 also likely has a larger number of strain cycles due to the localized effects of the vehicles passing directly over the top flange sensor locations. (This has been previously shown.)

The south midspan bottom flange sensor data shown in Figure 5.37 have a similar distribution to that of the north midspan bottom flange sensors (in Figure 5.35). Girder 3, once again, has a larger number of cycles, indicating more southbound traffic than northbound. Note that the distribution of the 25 με bin is similar to that of the north midspan bottom flange sensors, indicating that the trend was seen in both spans and is not an anomaly due to sensor or data processing issues. The south midspan top flange sensors (in Figure 5.38) have a distribution similar to that of the north midspan sensors, in which girder 4 has more cycles than girders 1, 5, and 6.
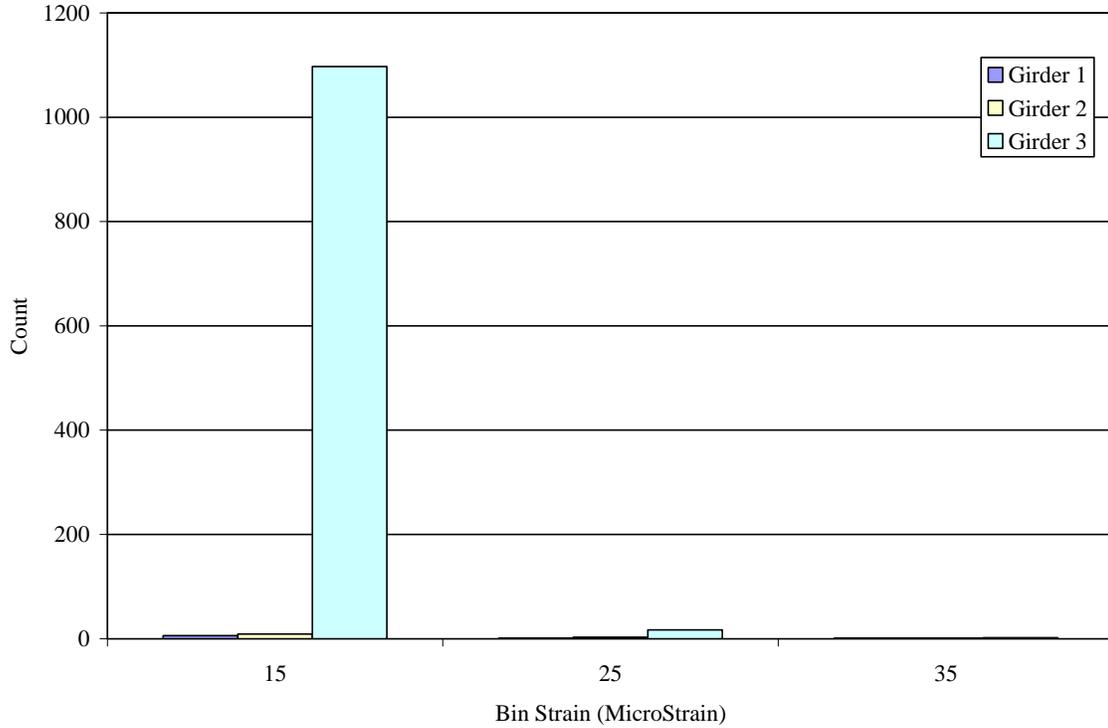
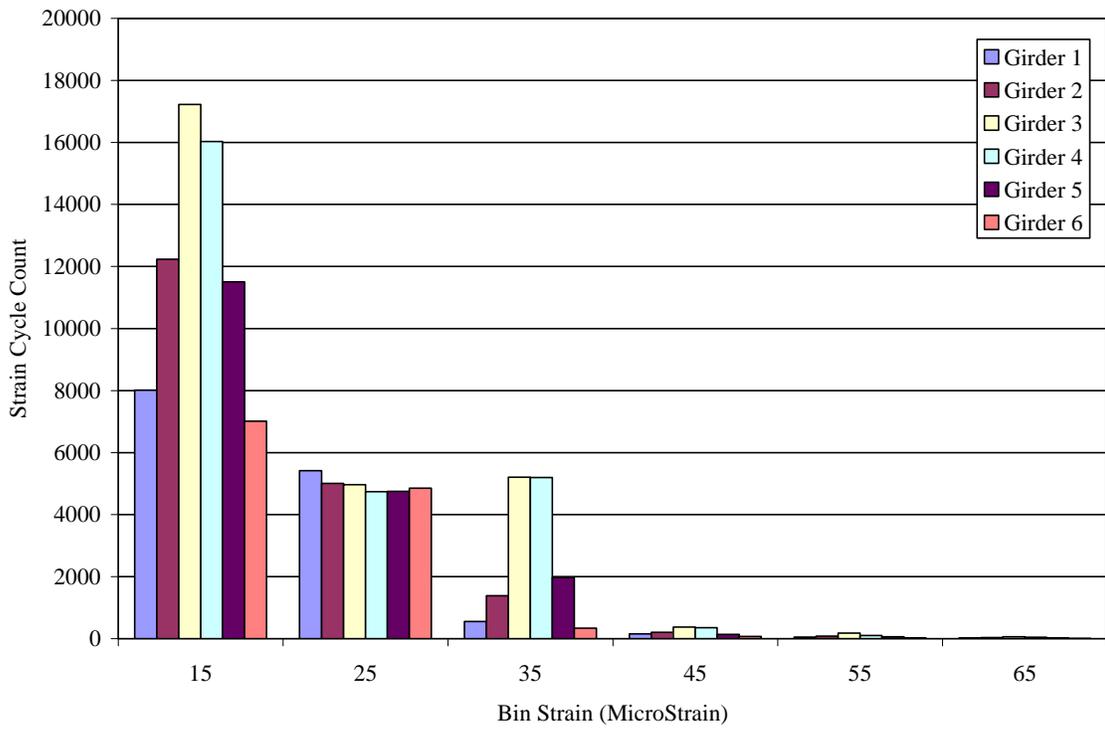**Figure 5.36. Rainflow counting results from top flange sensors at the north midspan**

Figure 5.37. Rainflow counting results from bottom flange sensors at the south midspan
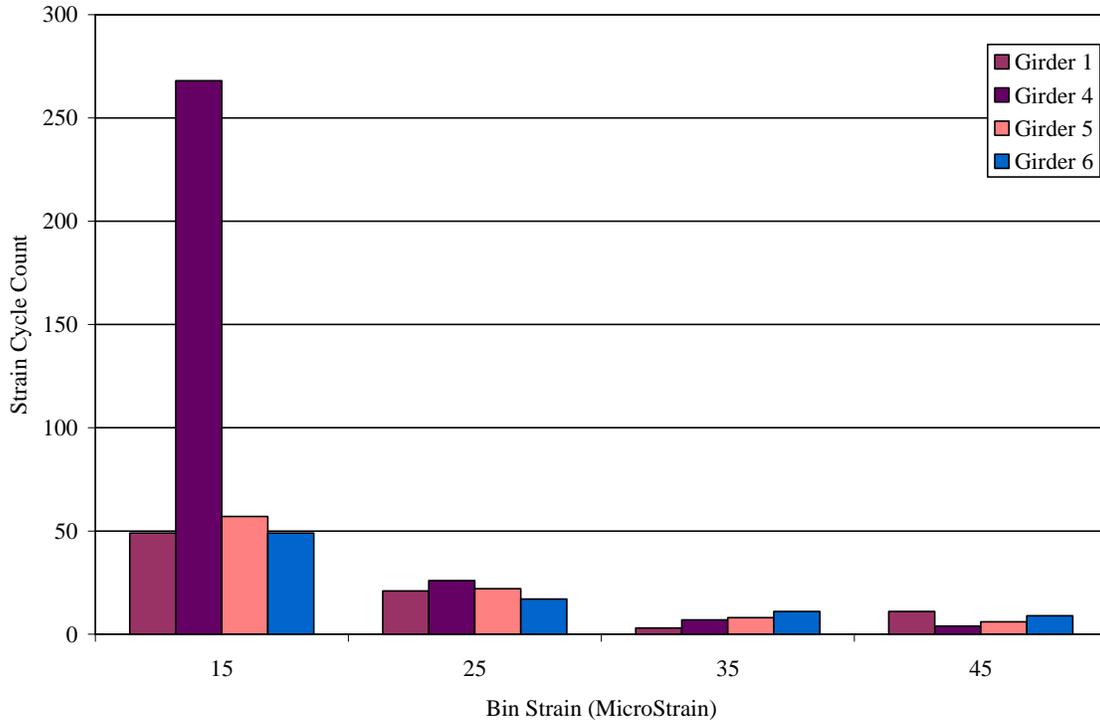
Figure 5.38. Rainflow counting results from top flange sensors at the south midspan

The number of cycles for the abutment sensors, shown in Figure 5.39, is reasonable, since the bottom flange strain at the abutment was shown to have smaller strain ranges than the north midspan bottom flange. The smaller strain ranges would lead to less strain cycles meeting the minimum bin size requirement. Girder 3 (bottom flange) has by far the largest number of cycles. Girder 1 is not shown due to its irregular performance for short-term events.

The rainflow counting of the weld stress concentrations, shown in Figure 5.40, indicates that the flange splice on girder 1 has the most cycles, followed by the web splice on girder 1 and then the flange splice on girder 2, and the fewest cycles are on the web splice on girder 2. The flange splice was shown to have slightly larger strains than the web splice, as shown in Figure 5.17. The splices in girder 1 showed less strain than those in girder 2 in the events presented above. (The strains from girder 1 were so small they were not shown on Figure 5.10a and 5.16a.) Therefore, some of the data presented in Figure 5.40 are supported by the strain plots shown above (e.g., the flange splice had more cycles than the plate splice), but other data are not (girder 1 had more cycles than girder 2).

Figure 5.39. Rainflow counting results from abutment sensors

Figure 5.40. Rainflow counting results from weld splice stress concentration sensors

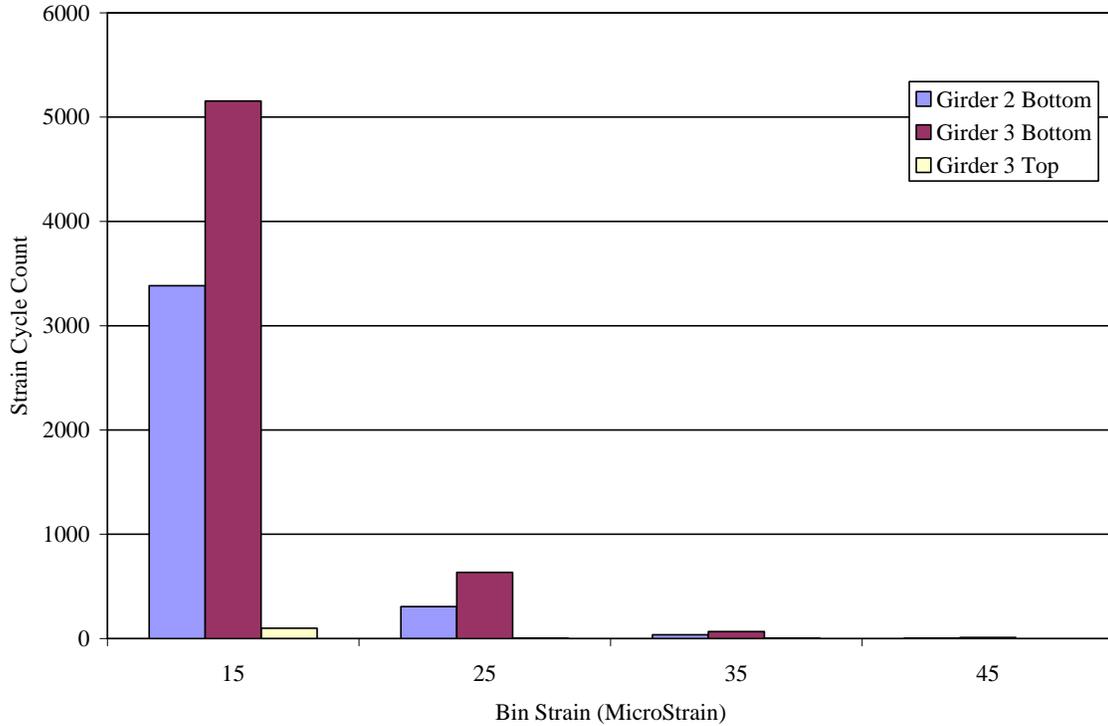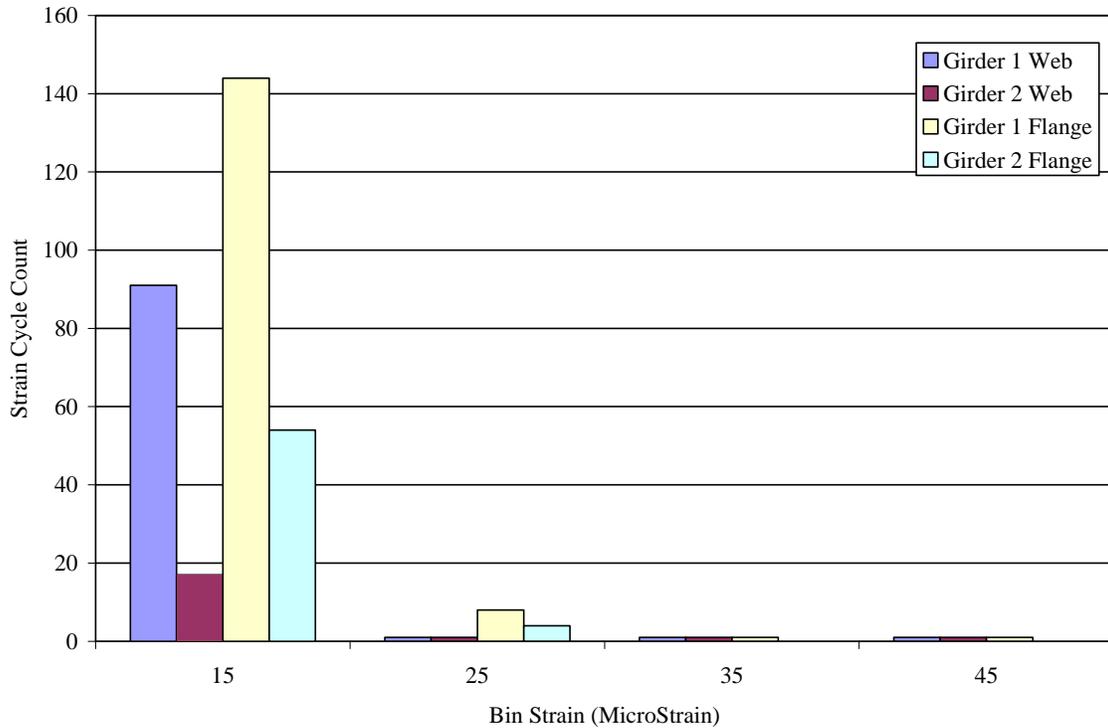Figure 5.41 shows the web gap region sensors. The girder 2 flange tipping has more cycles than the girder 2 web gap or the girder 1 flange tipping and web gap. This information agrees with what was shown in the strain data plots (Figures 5.10, 5.16, and 5.18). The web gap sensors on girder 3 are not shown due to a lack of data as a result of the sensor problems described above.

The fatigue details monitored include the weld between the flange and the web (flange and web weld splice sensors and the web gap sensors). Also included is the weld between the transverse diaphragm stiffener and the flange (flange tipping sensor). The maximum recorded stress in the weld between the flange and web on the bridge is 1.3 ksi (assuming a uniaxial state of stress and using Hooke's Law). This stress value is less than the design stress of 2 ksi and the AASHTO allowable stress of 15 ksi. The AASHTO allowable stress in the weld between the flange and the stiffener is 21 ksi, which is well above the maximum stress recorded on the bridge (0.73 ksi); the calculated design stress was 12 ksi.
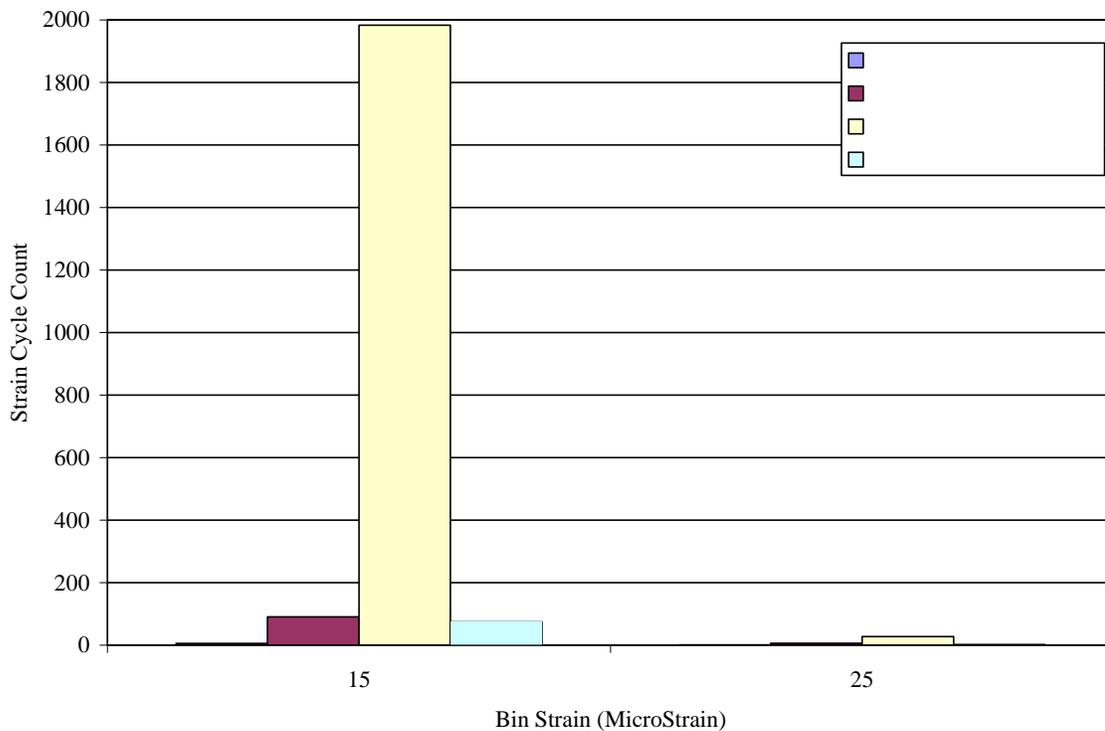
Figure 5.41. Rainflow counting results from web gap region sensors

Traffic Monitoring

A sample of what can be observed relative to traffic engineering is shown in Figures 5.42 and 5.43, which show the bottom flange strain cycles at the south midspan for the weeks of July 26 to August 1, 2004 and September 9 to September 15, 2004, respectively. It is interesting to note the increase in strain cycles in the fall relative to the summer. The traffic volume difference is most likely due to the close proximity of the bridge to a high school, as well as a lower number of people traveling to and from work in the summer months due to vacations. The dramatic drop

120

in the number of traffic events on the weekends compared to weekdays is also noticeable. Although this information as such is not directly applicable to the structural analysis of the bridge, this information may provide insight into changes in bridge performance related to changes in traffic patterns. The ability to extract traffic pattern information from the same data set as structural performance provides opportunities to further the understanding of how traffic patterns affect the behavior of a bridge over time.

Figure 5.42. Strain cycles from July 26 to August 1, 2004 at the south midspan bottom flange for girder 3

Figure 5.43. Strain cycles from September 9 to September 15, 2004 at the south midspan bottom flange for girder 3

6. CONCLUSIONS AND RECOMMENDATIONS

Conclusions

The intent of this project was to investigate the use and performance of high-performance steel (HPS) in bridge applications using a struct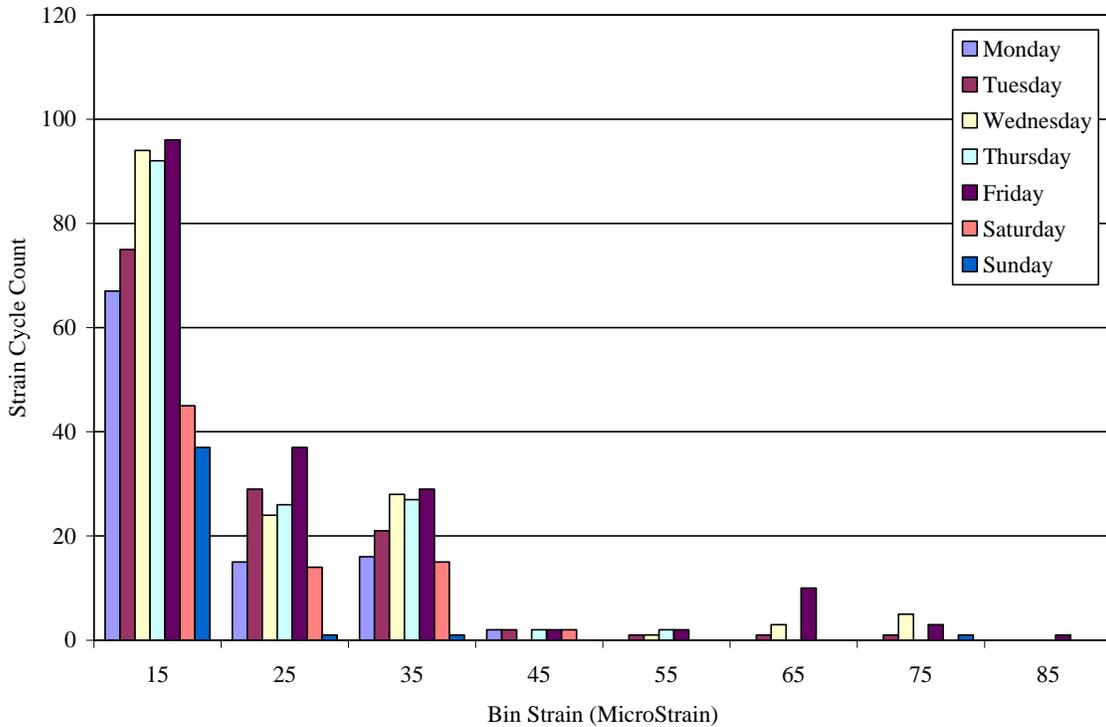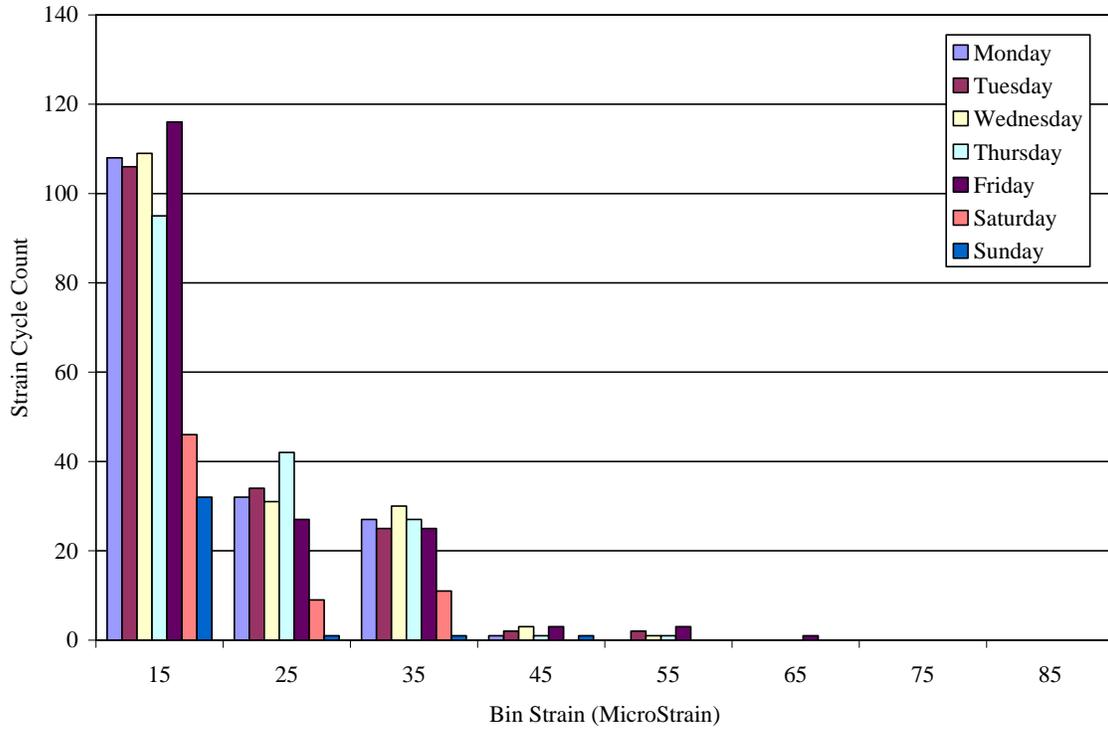ural health monitoring (SHM) system. The objectives of the East 12th Street Bridge SHM project were stated in section 1 and are outlined in the following summary of the project.

Design and Construction Documentation of the East 12th Street Bridge

As Iowa's first HPS bridge, the E. 12th St. bridge allowed the Iowa DOT to examine the relatively new material in terms of design, fabrication, and construction. The design of the bridge utilized the material strength, toughness, and fatigue characteristics of HPS. Construction documentation for the subject bridge was provided in section 3. One challenging aspect of the bridge construction was coordination with traffic on the major roadway (I-235) that the bridge spans. This limited the times when certain construction activities that mandated lane closures of I-235 could be performed.

East 12th Street Bridge Structural Health Monitoring System

The SHM system that was designed for and installed on the E. 12th St. Bridge generally met the objectives established for the project. This project provided an opportunity to evaluate and assess a remote, continuous, fiber-optic based SHM system. The following are major overall accomplishments:

- Given the location of the DASS equipment and the lack of accessibility to the equipment due to traffic, methods were developed to control the equipment from remote locations.
- Readily available technology was used and met the expectations for the objectives of the project.
- The monitoring system successfully acquired data continuously.
- A SHM data processing system was developed to monitor the bridge performance in a format that is consistent with design and evaluation parameters typically used by bridge engineering practitioners.
- While the website developed has been a useful part of the SHM system, there have been continued problems. User interaction with the website has, on occasion, been disrupted during the data collection.

Sensors

During a controlled load test, strain readings from 23 of the 36 FBG sensors used on the bridge were validated with respect to BDI strain transducers. Twenty-two of the 23 sensors proved to be accurate under live loading. Two types of FBG sensors were used: (1) bare FBG and (2) surface-

mountable sensors (bare FBG embedded in FRP). Several problems were encountered with the long-term strain readings of several bare FBGs, including the following:

- Optical loss
- Interference between sensors
- Large strain range of sensors
- Large compressive drop
- Backscatter

The surface-mountable sensors performed well under long-term and short-term loading conditions.

Data Processing

To deal adequately with the vast amount of data collected, to check the integrity of the data, to extract the reliable data (portions of the data were unreliable due to the problems discussed in this report), and to provide useful information, several programs were developed. These programs included the data correction program, data sorter program, and the data processing program. Each of these programs is started by a user who must load the data into the programs. This process, although simple and redundant, does demand time and require that the user be actively involved in data processing. Since the programs are performed in a post-processing mode, rather than in real-time, the results from the processing are not readily available to the research team.

Monitoring Performance Changes Using Bridge Indices

The bridge performance indices mentioned in the report are calculated from the processed live load strain data. Monitoring changes in these indices may provide information regarding the health and performance of the bridge over time. The data can provide insight into the deterioration rates, possible reasons for deterioration, the extent of deterioration, and ways performance is affected. The following observations were based on the bridge indices calculated from ambient traffic and the controlled load test:

- Distribution factor
  - The south midspan load distribution is better than the load distribution in the north midspan.
  - The typical average DF per day for an interior girder is between 0.20 and 0.25; the AASHTO design DF is 0.62.
  - Monitoring the DF from ambient traffic over time may provide a useful tool for bridge engineers, since the data collected have shown slight changes.

- Neutral axis
  - The theoretical NA location for girder 4 at the south midspan differed significantly from the experimental NA location.
  - The theoretical NA location for girder 3 at the north midspan matched the experimental NA location well.
  - There were noticeable differences between the NA location of girder 3 at the north midspan and girder 4 at the south midspan (laterally symmetrical girders).
  - As the trends of the NA are examined over time, conclusions about the performance of the bridge should be apparent, since the NA has been fairly consistent over time at each location the NA is calculated.

- End restraint
  - The data collected have provided a baseline of bridge performance.
  - The value of the ER is still undetermined; as more data are collected, the significance will be evaluated.

In addition to monitoring each of the indices individually, examining them together over time may provide insight into the bridge performance because the indices are based on interrelated properties of the bridge.

Fatigue-Sensitive Detail Performance

The strain plots of the ambient traffic and controlled load tests show very low levels of strain in the localized fatigue details. This observation is verified by the number and magnitudes of stress cycles in the Cycle Counting section. The largest stress value observed in the weld between the flange and the web due to a live load event is 1.3 ksi; this is less than the design stress (2 ksi) and significantly less than the AASHTO allowable stress (15 ksi). The stress recorded between the flange and the stiffener (0.73 ksi) is considerably less than the design stress (12 ksi) and the AASHTO allowable stress (21 ksi).

Recommendations

Sensors

As stated in the Sensor Performance section, several problems were encountered with the fiber-optic sensors. For future work with continuous health monitoring and fiber-optic sensing, the research team recommends the following:

- Use surface-mountable sensors.
- Use at least a 3 mm jacket on the cable.
- Use mechanical splices to splice adjacent fiber strands.
- If bare FBGs are used, test different types of epoxy for the best adhesion.
- Separate the wavelengths of adjacent sensors by at least 5 nm.
- Cover sensors and splices such that they are accessible for visual inspection. (This is only necessary if access to sensors will be available after installation. In this project, future

access is unobtainable.)

After completing this project, the research team recommends that continuous monitoring be continued and a revised plan for instrumentation location has been developed. This plan involves replacing some of the bare FBGs with surface-mountable sensors, removing some sensors completely, and supplementing the existing sensors with more surface-mountable sensors. The plan calls for placing top and bottom flange sensors on every girder at the north midspan, installing bottom flange sensors on girders 2, 3, 4, and 5 at the north abutment, monitoring the flange and web plate splice weld on girder 2, installing sensors in the web gap near the pier on girders 1 and 2, installing bottom flange sensors on girders 3 and 4 near the pier in the negative moment region, and leaving the surface-mountable sensors located at the south midspan. This plan will allow the bridge indices to be further developed and studied while eliminating some of the fatigue detail sensors due to low strain levels. This instrumentation scheme should improve the research team's ability to monitor the use of HPS on the E. 12th St. Bridge using a remote, continuous fiber-optic SHM system.

Data Processing

To simplify user intervention and reduce the repetitive involvement required in data processing, it is recommended that a system be developed that combines the programs used for data processing. Along with this recommendation, it may be beneficial to automate the processing and perform it in real-time. Performing the data processing in real-time would require a change in the algorithms currently used. A data collection and processing system that requires little user intervention but still provides the beneficial information of the current system would enhance the capabilities of the current system. Such a system that requires low levels of involvement in the collection and processing of the data would be advantageous in expanding the use of SHM to more bridges.

REFERENCES

American Association of State Highway and Transportation Officials (AASHTO). 1996. *Standard Specifications for Highway Bridges*. 16th Ed. Washington D.C.: American Association of State Highway and Transportation Officials.

American Society for Testing and Materials (ASTM) International. 2002. Annual Book of ASTM Standards. West Conshohocken, PA: American Society for Testing and Materials.

Ansari, F. 2003. Fiber-optic health monitoring of civil structures. *Proceedings of the First International Conference on Structural Health Monitoring and Intelligent Infrastructure*. Tokyo, Japan: Japan Society of Civil Engineers. 19–30.

Bannantine, J.A., J.J. Commer, and J.L. Handrock. 1990. *Fundamentals of Metal Fatigue Analysis*. Englewood Cliffs, NJ: Prentice Hall.

Bethlehem Lukens Plate. 2002. *Bethlehem Lukens Plate High-Performance Steels for Bridges: HPS-70W*. http://www.bethsteel.com/customers/pdfs/bridges.pdf.

Blue Road Research. 2005. *State-of-the-Art Optical Sensor Solutions*. http://www.blueroadresearch.com/.

Casciati, F., L. Faravelli, F. Borghetti, and A. Fornasari. 2003. Future trends in infrastructure monitoring. *Proceedings of the First International Conference on Structural Health Monitoring and Intelligent Infrastructure*. Tokyo, Japan: Japan Society of Civil Engineers. 997–1002.

Center for the New Engineer. Accessed 2005. *Asynchronous Transfer Mode (ATM) Tutorial*. http://cs.gmu.edu/cne/modules/atm/Texttut.html.

Dummies.com. 2006. *Storing Data with PHP – Flat File or Database*? http://www.dummies.com/WileyCDA/DummiesArticle/id-2402.html.

Glisic, B., D. Inaudi, S. Vurpillot, E. Bu, and C.-J. Chen. 2003. Piles monitoring using topologies of long-gage fiber-optic sensors. *Proceedings of the First International Conference on Structural Health Monitoring and Intelligent Infrastructure*. Tokyo, Japan: Japan Society of Civil Engineers. 291–298.

Inaudi, D. 2003. State of the art in fiber-optic sensing technology and EU structural health monitoring projects. *Proceedings of the First International Conference on Structural Health Monitoring and Intelligent Infrastructure*. Tokyo, Japan: Japan Society of Civil Engineers. 191–198.

Inaudi, D., and B. Glisic. 2004. Combining static and dynamic deformation monitoring with long-gage fiber-optic sensors. *Proceedings of the Second International Conference on Bridge Maintenance, Safety, Management and Cost*. Kyoto, Japan: International Association for Bridge Maintenance and Safety. 543–544.

Indiana University Knowledge Base. 2005. *What are some common networking terms*? http://kb.indiana.edu/data/ahpn.html?cust=450662.53156.30.

Kulcu, E., X. Qin, R.A. Barrish, Jr., and A.E. Aktan. 2000. Information Technology and Data Management Issues for Health Monitoring of The Commodore Barry Bridge. *International Society for Optical Engineering* 3995. 98–111.

Liu, D.H., W.L. Jin, E.Y. Zhang, and J.W. Shao. 2003. Applying Brillouin health monitoring network for civil engineering. *Proceedings of the First International Conference on Structural Health Monitoring and Intelligent Infrastructure*. Tokyo, Japan: Japan Society of Civil Engineers. 237–240.

Lwin, M.M. 2002. *High Performance Steel Designers' Guide*. Washington, D.C.: Federal Highway Administration (FHWA). http://www.fhwa.dot.gov/download/hpsguide.pdf.

Luna Innovations. 2006. *Products at Luna…*.
    http://www.lunainnovations.com/products/systems.htm.

Micron Optics. 2003. *Si425*. http://www.micronoptics.com/si425.htm.

PCB Piezotronics, Inc. 2006. *Products*. http://www.pcb.com/products/.

Roctest. 2004. *Vibrating-Wire Strain Gage*.
    http://www.roctest.com/modules/AxialRealisation/img_repository/files/documents/C-
    110.pdf.

Roctest. 2006. *Products: Readout and dataloggers*.
    http://www.roctest.com/index.php?module=CMS&id=73.

Seim, J., E. Udd, and W. Schulz. 1999. Health monitoring of an Oregon historical bridge with
    fiber grating strain sensors. *International Society for Optical Engineering* 3671. 128–134.

Tennyson, R.C., A.A. Mufti, S. Rizkalla, G. Tadros, and B. Benmokrane. 2001. Structural health
    monitoring of innovative bridges in Canada with fiber-optic sensors. *Smart Materials and
    Structures* 10.3. 560–573.

Texas Measurements, Inc. Accessed 2005. *Strain Gage Series List*.
    http://straingage.com/strain_gage/list/index.php.

Todd, M.D., G.A. Johnson, and B.L. Althouse. 2001. A novel Bragg grating sensor interrogation
    system utilizing a scanning filter, a Mach-Zehner interferometer, and a 3x3 coupler.
    Measurement Science and Technology 12.7. 771–777.

Trans-Tek, Inc. Accessed 2005. *Linear Variable Differential Transformers*.
    http://www.transtekinc.com/lvdt.htm.

Webopedia. 2006. *Database*. Jupitermedia Corporation.
    http://webopedia.internet.com/TERM/d/database.html.

Webopedia. 2006. *Flat-file database*. Jupitermedia Corporation.
    http://webopedia.internet.com/TERM/f/flat_file_database.html.

Wilson, A.D. 2000. Production of High Performance Steels for U.S.A. Bridges. Presented at the
    Conference of High-Performance Steel Bridges, Baltimore, MD.
    http://www.nabro.unl.edu/articles/20002012/download/wilson.pdf.

University of Tennessee, Technology Consulting and Support. 2006. Overview of Wireless
    Technologies. http://oit.utk.edu/helpdesk/section/Wireless/38.